6-18-2018

Accelerated Broadband Spectra and Attosecond Charge Migration Simulations using Real-Time Time-Dependent Density Functional Theory

Adam S. Bruner
Louisiana State University and Agricultural and Mechanical College

ACCELERATED BROADBAND SPECTRA AND ATTOSECOND CHARGE MIGRATION SIMULATIONS USING REAL-TIME TIME-DEPENDENT DENSITY FUNCTIONAL THEORY

A Dissertation

Submitted to the Graduate Faculty of the
Louisiana State University and
Agricultural and Mechanical College
in partial fulfillment of the
requirements for the degree of
Doctor of Philosophy

in

The Department of Chemistry

by
Adam S. Bruner
B.S., Rose-Hulman Institute of Technology - Terre Haute, 2013
August 2018

Acknowledgments

I am excited to say "I did it!" While this journey has been fun, I have learned a lot along the way, becoming a better scientist and engineer. When I left a solid career in industry to pursue this doctoral degree in chemistry, I never imagined all the other adventures that accompanied that decision.

My success, however, has been supported and guided by many people, and this work would not have been possible without the direction of my advisor, Dr. Kenneth Lopata. I am grateful for our many discussions on physical chemistry and for your ability to inspire and challenge me in my research. Many thanks for your instrumental role in my personal and professional development.

This gratitude extends to Dr. Mette Gaarde and Dr. Kenneth Schafer for their support and collaboration for much of this work. They have been a continued source of experienced research and always offer a physical and insightful perspective. My research on charge migration, which serves as a major component of this dissertation, would not have been possible without their support and direction.

I would like to offer special thanks to Dr. Samuel Hernandez for his many contributions to the charge migration efforts as well as my other group members: Dr. Holden Smith, Alex Meyer, Adonay Sissay, and Daniel LaMaster.

Finally, I am thankful for the ongoing support of friends and family. To my best friend Matthew Welmers, I am grateful for the many laughs and adventures that have bolstered my mettle and endurance here. Of course, many thanks to Caite Bresnahan, who reminds me that learning extends beyond the classroom or the lab; you are a true inspiration. To my Parents, I thank you for the many prayers, constant support, wisdom, and many phone calls. Lastly, to my brother, I thank you for your genuine support and admiration; you remind me that life is more than quantum mechanics.

Table of Contents

Abstract

In this dissertation, the calculations of light-matter interactions offer insight into the structure and dynamical response of electrons in molecular systems. Such information is useful for characterizing molecules, electronic structure, photochemistry, photomaterials, and a host of other applications. In the first part of this work, simulations of broadband absorption spectra are accelerated by the use of Padé approximanants of Fourier Transforms and dipole decomposition. Electronic absorption spectra from valence and core levels are obtained using time-dependent methods and compared to results from established perturbative techniques. In addition, core level absorption spectra are calculated for a nickel porphyrin and shown to be consistent with experimental XANES spectra. Not only is the speed up of these real-time simulations significant (at least 5x faster), but such methods offer the ability to directly calculate the dipole response from molecular orbital pairs involved in a given transition.

In the second part of this dissertation, time-dependent density functional theory (TDDFT) calculations were performed to capture core-hole-initiated charge migration. By using well-defined initial states, well-known problems of resonant excitation (with TDDFT) caused by the adiabatic approximation are avoided. Using such initial states, core-hole-initiated valence charge migration is obtained in nitrosobenzene by TDDFT. These results are shown to be in good agreement with those of more accurate methods, provided the use of a hybrid functional to incorporate both electron correlation and exchange. In addition, the time-dependent electron localization function (TD-ELF) can convert the density into a Lewis-dot picture of bonds and lone pairs of electrons.

Building upon these charge migration studies, initial states in the valence orbitals were also constructed. In valence ionization, the electron is partially removed from multiple channels or orbitals; thus, multiple orbitals are involved in constructing the valence hole initial states. Due to the sudden ionization approximation made by construction of the

initial states, a broadband-like response causes many dynamical modes to be excited. Here, the amplitude and phase of Fourier transforms are used to extract and classify the modes as charge migration or density-like excitation. These modes are then used to calculate metrics like migration distance and speed. Using this information in conjuction with the TD-ELF, it becomes possible to not only interpret charge migration, but to predict it by established chemical principles.

Chapter 1. Introduction

1.1 Overview of Quantum Mechanics

Modeling electronic spectroscopy and dynamics in molecules and materials is important for elucidating excited state mechanisms, for predicting dynamical properties, and for interpreting experimental results. Before readily diving into the sea of symbols, however, it is first important to understand why studies of the base functioning units of the universe have only recently begun. While, yes, there are obvious reasons – such as as the tiny size of subatomic particles or perhaps the ability to calculate such complex systems without modern computers. Moreso, the slow progress in the early days of this field was because of the quantum nature of such particles. The conventional world operates in a classical sense, which means that objects can have separable properies of position and momentum (among other things). In other words, it is possible to know both where something is and how quickly it is moving for classical systems. A little over 100 years ago, scientists found that blackbody radiation curves were not consistent with classical theory, and Max Plank postulated that a fitting parameter could be added to correct for the discrepancy. Eventually, this came to be used to obtain:

$$E_{\text{ph}} = h\nu \tag{1.1}$$

where E_{ph} is the energy of a photon, h is Planck's fitting parameter or constant, and ν is the frequency of light. Atomic systems have discrete frequencies of allowed energies, which implies that rather than a continuum of classical values, small particles are "quantized" and can only have discrete energy values. A great amount of contention and effort has arisen out of these implications; however, treating such systems in a quantized manner yields strikingly accurate results.

Due to the inseparable particle nature and wave nature of electrons, a special state function is useful in describing their behavior in chemical systems. Such functions are often referred to as wavefunctions because of their oscillatory behavior, and therefore depend upon

time and position. Although several formalisms for solving such functions exist, perhaps, the most famous is the Schrödinger equation:

$$i\frac{\partial\Psi(r,t)}{\partial t} = -\frac{1}{2}\nabla^2\Psi(r,t) + V(r,t)\Psi(r,t) \tag{1.2}$$

in atomic units. Here, this differential equation relates the wavefunction ($\Psi(r,t)$) to physical observables, where $V(r,t)$ represents a potential that influences the motion of the particles. One important observable can be obtained by multiplying the complex-valued wavefunction by its complex conjugate to yield the probability density. This probability density represents the likelihood of finding the particle at various positions over time; hence this does not yield the exact location of an electron, rather where it is probabalistically expected to be.

At this point, it is important to mention that for a single electron, the Schrödinger equation can be solved exactly. Solutions to the multi-electron problem, however, are not tractable; although, many approximate methods have been developed to tackle some of the challenges of this "many-body" problem. Such methods offer a way to study the electronic processes in molecules and materials, gaining insight into electronic spectroscopy experiments, which probe light-matter interactions and dynamics.

1.2 Electronic Spectroscopy and its Application

Often, understanding spectroscopy and associated experiments is difficult, especially as since the motion of the electrons occurs on incredibly short timescales – even so small as a few attoseconds (a billion billionths of a second, 10^{-18} s). Not only are such experiments challenging to perform, but they can also be difficult to interpret. Using quantum mechanics, it becomes possible to simulate such experiments from first principles in physics and chemistry. By studying how electrons move in their native quantum environment, it becomes possible to directly study how the molecular and electronic structure are related to the experimentally observed response. If we consider a bridge or a building, each has a different frame

structure designed to perform different functions and withstand specific types of stressors. The same is true for molecules and materials. Not only is electronic spectroscopy useful for understanding electronic motion, but it is also a powerful tool to characterize and design new materials. For instance, the valence electrons are farthest from the positive nucleus in an atom; these electrons participate in bonding and interatomic-molecular interactions. In addition, valence electrons are the "freest" to move around and participate in dynamics such as charge migration, charge transfer, ionization, excitation, and many other processes. Core electrons, however, are much closer to the nuclei and are less shielded by the other electrons. As such, core electrons experience a greater amount of the positive charge and remain more localized around the nuclei. Excitation of core electrons requires much more energy, but can provide detailed information about long range structure, electron arrangement, and energy levels.

Typically, excited state simulations are performed in the frequency domain, assuming weak perturbation from the ground state. For such calculations, the gentle perturbations do not significantly shift the energy levels of the electronic structure. In contrast, real-time methods propagate the system in time. Although real-time methods are less common, they are often require longer simulations, yet are also valid in both the linear and non-linear regime, formally permitting the use of strong fields. Such real-time methods include: semi-empirical methods[1,2], Hartree-Fock[3–5], time-dependent density functional theory[6–15], configuration interaction[16–18], multi-configurational self-consistent field[19–21], coupled cluster[22,23], two-electron reduced density matrix methods[24], among others.

For the work of this dissertation, time-dependent density functional theory[25,26] (TDDFT) is used for most of the calculations. TDDFT is one of the most popular excited state methods because it offers a good balance between speed and accuracy. Although results can be sensitive to the choice of DFT functional, much progress has been made towards using TDDFT for a range of challenging processes. Both perturbative (linear-response) as

well as time-dependent TDDFT have been been shown to accurately capture challenging processes. Some such cases include charge transfer[27,28], double excitations[29], strong-field ionization[30,31], above-threshold resonances[32], core-level spectra[33,34], hyperpolarizabilities[35], and excited state absorption[36], just to name a few.

For weak excitations like absorption spectroscopies (UV/Vis, XANES, etc.), perturbative methods like linear-response time-dependent density functional theory (LR-TDDFT) can be used. Unfortunately, the perturbative LR-TDDFT techniques fail to capture strong-field processes. Furthermore, standard implementations are root-based solutions[37,38], which become computationally intensive for systems with a higher number of absorption energies. In contrast, weak-field spectra can also be obtained in the time domain with real-time (RT) TDDFT. Although such methods often require longer simulations for weak-field calculations due to the Fourier uncertainty principle (Discussed in Chapter 2), this dissertation outlines a technique that dramatically reduces propagation time, making it competitive to LR-TDDFT for large numbers of roots (Chapter 3).

Beyond the initial light-matter interations involved in spectroscopy, is it important to study the resulting dynamics. The motion of electrons in excited states and ionized systems may also contain information that underpins applications in light harvesting, photochemistry, and pump-probe spectroscopies. Such dynamics on the attosecond time scale often result from strong field processes like ionization. One such process, high harmonic generation (HHG), involves ionizing an electron, accelerating it in an oscillating (AC) electric field, and recombining it with the parent molecule to probe the charge evolution in the absence of the electron. It requires a large amount of energy to remove the electron, significantly altering the electronic system. While the electron is away from the parent, the other electrons continue to evolve, later to be probed by the ionized electron. Depending on the acceleration time/recollision time, the evolution changes the probed states. To study such charge

migration dynamics, we introduce a methodology based upon construction of well-defined intial states using RT-TDDFT in chapters 4 and 5.

1.3 Funding Sources

The efforts of this dissertation on dipole contributions were supported by the Louisiana Board of Regents Research Competitiveness Subprogram under contract number LEQSF(2014-17)-RD-A-03 (PI: Lopata). The dipole contribution material is based in part upon work supported by the National Science Foundation under the grant number CHE-1362641 (PI: Lopata). Charge migration and high harmonic generation research was funded by the U.S. Department of Energy, Office of Science, Office of Basic Energy Sciences, under award number DE-SC0012462. Computational hardware used for portions of this research was supported by the 2015 Ralph E. Powe Junior Faculty Enhancement Award from Oak Ridge Associated Universities (PI:Lopata). Portions of research was performed using high-performance computational resources provided by Louisiana State University (http://www.hpc.lsu.edu) and Louisiana Optical Network Infrastructure (http://www.loni.org).

1.4 Scope of Dissertation

In this dissertation, methods for accelerating, modeling, and interpreting DFT spectroscopy simulations will be presented. In addition, real-time TDDFT methods will be used to capture the motion of electrons, and the implementation of such techniques will be discussed. These are in contrast to linear-response (LR) methods, which propagate in the freqency domain and are inherently perturbative in nature.

The general principles of quantum mechanical simulations, differences in TDDFT calculations, some of the major problems faced by DFT, and a brief introduction to how these are addressed are outlined in Chapter 2. As a second consideration, signal processing is an integral part of analyzing electron dynamics from a real-time simulation, and a description of methodologies has also been included here. Such techniques not only provide the benefit

of interpreting complex signals, but can also be used to accelerate the convergence of their results.

In Chapter 3, an analysis and acceleration technique is validated for electronic absorption spectra of water and a nickel porphyrin. Here, the acceleration technique is shown to be 7x faster than conventional transformation for water and competitive with linear response for the large nickel porphyrin. Furthermore, the individual electronic contributions for each absorption peak are validated for valence and core excitations.

Chapter 4 discusses the importance of a well-defined initial state, and a detailed implementation of how it can be used to obtain accurate charge migration (CM) and hole dynamics is included. As mentioned earlier, such dynamics are valuable for interpreting experiments like HHG as well as determining the underlying dynamics involved in photochemistry and solar cells. The use of TDDFT for these studies comes with its own set of challenges due to the approximate nature of the DFT functional. In particular, due to a formal dependence upon the entire history of the charge density, TDDFT struggles to capture electron dynamics following large changes in population within the charge density. As shown in this chapter (4), such problems can be avoided by using well-defined initial states. Here, RT-TDDFT with a well-defined core-hole initial state demonstrates accurate results in nitrosobenzene.

Expanding upon the charge migration studies, Chapter 5 discusses how to obtain valence and core initiated CM dynamics in carbonyl sulfide, iodoacetylene, hexatriene, 1,2-diethenyl diborane, and nitrosobenzene. Here, the special construction of the initial states results in a multimodal (broadband-like) excitation, and both "charge-like" migration and "density-like" non-migration modes are excited. Several techniques are introduced to extract and identify modes specifically related to coherent charge migration rather than a density-like excitation. Once the modes are identified, metrics like migration speed and distance are then computed to characterize the dynamics in a way expected to be relevant to experiment.

1.5 References

[1] L. A. Bartell, M. R. Wall, and D. Neuhauser, "A time-dependent semiempirical approach to determining excited states," *J. Chem. Phys.*, vol. 132, no. 23, p. 234106, 2010.

[2] K. Lopata, R. Reslan, M. Kowalska, D. Neuhauser, N. Govind, and K. Kowalski, "Excited-state studies of polyacenes: a comparative picture using eomccsd, cr-eomccsd (t), range-separated (lr/rt)-tddft, td-pm3, and td-zindo," *J. Chem. Theory Comput.*, vol. 7, no. 11, pp. 3686–3693, 2011.

[3] K. C. Kulander, "Time-dependent hartree-fock theory of multiphoton ionization: Helium," *Phys. Rev. A*, vol. 36, pp. 2726–2738, Sep 1987.

[4] X. Li, S. M. Smith, A. N. Markevitch, D. A. Romanov, R. J. Levis, and H. B. Schlegel, "A time-dependent hartree–fock approach for studying the electronic optical response of molecules in intense fields," *Phys. Chem. Chem. Phys.*, vol. 7, no. 2, pp. 233–239, 2005.

[5] C. M. Isborn and X. Li, "Singlet-triplet transitions in real-time time-dependent hartree-fock/density functional theory," *J. Chem. Theory Comput.*, vol. 5, no. 9, pp. 2415–2419, 2009.

[6] J. Theilhaber, "Ab initio simulations of sodium using time-dependent density-functional theory," *Phys. Rev. B*, vol. 46, pp. 12990–13003, Nov 1992.

[7] K. Yabana and G. F. Bertsch, "Time-dependent local-density approximation in real time," *Phys. Rev. B*, vol. 54, pp. 4484–4487, Aug 1996.

[8] X. Andrade, D. Strubbe, U. De Giovannini, A. H. Larsen, M. J. T. Oliveira, J. Alberdi-Rodriguez, A. Varas, I. Theophilou, N. Helbig, M. J. Verstraete, L. Stella, F. Nogueira, A. Aspuru-Guzik, A. Castro, M. A. L. Marques, and A. Rubio, "Real-space grids and the octopus code as tools for the development of new simulation approaches for electronic systems," *Phys. Chem. Chem. Phys.*, vol. 17, pp. 31371–31396, 2015.

[9] R. Baer and D. Neuhauser, "Real-time linear response for time-dependent density-functional theory," *J. Chem. Phys.*, vol. 121, no. 20, pp. 9803–9807, 2004.

[10] C.-L. Cheng, J. S. Evans, and T. Van Voorhis, "Simulating molecular conductance using real-time density functional theory," *Phys. Rev. B*, vol. 74, no. 15, p. 155112, 2006.

[11] J. Sun, J. Song, Y. Zhao, and W.-Z. Liang, "Real-time propagation of the reduced one-electron density matrix in atom-centered gaussian orbitals: Application to absorption spectra of silicon clusters," *J. Chem. Phys.*, vol. 127, no. 23, p. 234107, 2007.

[12] S. Meng and E. Kaxiras, "Real-time, local basis-set implementation of time-dependent density functional theory for excited state dynamics simulations," *J. Chem. Phys.*, vol. 129, no. 5, p. 054110, 2008.

[13] H. O. Wijewardane and C. A. Ullrich, "Real-time electron dynamics with exact-exchange time-dependent density-functional theory," *Phys. Rev. Lett.*, vol. 100, no. 5, p. 056404, 2008.

[14] K. Lopata and N. Govind, "Modeling fast electron dynamics with real-time time-dependent density functional theory: Application to small molecules and chromophores," *J. Chem. Theory Comput.*, vol. 7, no. 5, pp. 1344–1355, 2011.

[15] M. R. Provorse and C. M. Isborn, "Electron dynamics with real-time time-dependent density functional theory," *Int. J. of Quant. Chem.*, vol. 116, no. 10, pp. 739–749, 2016.

[16] P. Krause, T. Klamroth, and P. Saalfrank, "Time-dependent configuration-interaction calculations of laser-pulse-driven many-electron dynamics: Controlled dipole switching in lithium cyanide," *J. Chem. Phys.*, vol. 123, no. 7, p. 074105, 2005.

[17] A. E. DePrince, M. Pelton, J. R. Guest, and S. K. Gray, "Emergence of excited-state plasmon modes in linear hydrogen chains from time-dependent quantum mechanical methods," *Phys. Rev. Lett.*, vol. 107, p. 196806, Nov 2011.

[18] P. Krause, J. A. Sonk, and H. B. Schlegel, "Strong field ionization rates simulated with time-dependent configuration interaction and an absorbing potential," *J. Chem. Phys.*, vol. 140, no. 17, p. 174113, 2014.

[19] H.-D. Meyer, U. Manthe, and L. S. Cederbaum, "The multi-configurational time-dependent hartree approach," *Chem. Phys. Lett.*, vol. 165, no. 1, pp. 73–78, 1990.

[20] M. Nest, T. Klamroth, and P. Saalfrank, "The multiconfiguration time-dependent hartree–fock method for quantum chemical calculations," *J. Chem. Phys.*, vol. 122, no. 12, p. 124102, 2005.

[21] T. Sato and K. L. Ishikawa, "Time-dependent complete-active-space self-consistent-field method for multielectron dynamics in intense laser fields," *Phys. Rev. A*, vol. 88, no. 2, p. 023402, 2013.

[22] C. Huber and T. Klamroth, "Explicitly time-dependent coupled cluster singles doubles calculations of laser-driven many-electron dynamics," *J. Chem. Phys.*, vol. 134, no. 5, p. 054113, 2011.

[23] S. Kvaal, "Ab initio quantum dynamics using coupled-cluster," *J. Chem. Phys.*, vol. 136, no. 19, p. 194109, 2012.

[24] D. B. Jeffcoat and A. E. DePrince III, "N-representability-driven reconstruction of the two-electron reduced-density matrix for a real-time time-dependent electronic structure method," *J. Chem. Phys.*, vol. 141, no. 21, p. 214104, 2014.

[25] E. Runge and E. K. U. Gross, "Density-functional theory for time-dependent systems," *Phys. Rev. Lett.*, vol. 52, pp. 997–1000, Mar 1984.

[26] M. Petersilka, U. Gossmann, and E. Gross, "Excitation energies from time-dependent density-functional theory," *Phys. Rev. Lett.*, vol. 76, no. 8, p. 1212, 1996.

[27] A. Dreuw, J. L. Weisman, and M. Head-Gordon, "Long-range charge-transfer excited states in time-dependent density functional theory require non-local exchange," *J. Chem. Phys.*, vol. 119, no. 6, pp. 2943–2946, 2003.

[28] T. Stein, L. Kronik, and R. Baer, "Reliable prediction of charge transfer excitations in molecular complexes using time-dependent density functional theory," *J. Am. Chem. Soc.*, vol. 131, no. 8, pp. 2818–2820, 2009.

[29] C. M. Isborn and X. Li, "Modeling the doubly excited state with time-dependent hartree–fock and density functional theories," *J. Chem. Phys.*, vol. 129, no. 20, p. 204107, 2008.

[30] X.-M. Tong and S.-I. Chu, "Time-dependent density-functional theory for strong-field multiphoton processes: Application to the study of the role of dynamical electron correlation in multiple high-order harmonic generation," *Phys. Rev. A*, vol. 57, no. 1, p. 452, 1998.

[31] M. Lein and S. Kümmel, "Exact time-dependent exchange-correlation potentials for strong-field electron dynamics," *Phys. Rev. Lett.*, vol. 94, no. 14, p. 143003, 2005.

[32] K. Lopata and N. Govind, "Near and above ionization electronic excitations with non-hermitian real-time time-dependent density functional theory," *J. Chem. Theory Comput.*, vol. 9, no. 11, pp. 4939–4946, 2013.

[33] K. Lopata, B. E. Van Kuiken, M. Khalil, and N. Govind, "Linear-response and real-time time-dependent density functional theory studies of core-level near-edge x-ray absorption," *J. Chem. Theory Comput.*, vol. 8, no. 9, pp. 3284–3292, 2012.

[34] P. J. Lestrange, P. D. Nguyen, and X. Li, "Calibration of energy-specific tddft for modeling k-edge xas spectra of light elements," *J. Chem. Theory Comput.*, vol. 11, no. 7, pp. 2994–2999, 2015.

[35] F. Ding, B. E. Van Kuiken, B. E. Eichinger, and X. Li, "An efficient method for calculating dynamical hyperpolarizabilities using real-time time-dependent density functional theory," *J. Chem. Phys.*, vol. 138, no. 6, p. 064104, 2013.

[36] S. A. Fischer, C. J. Cramer, and N. Govind, "Excited state absorption from real-time time-dependent density functional theory," *J. Chem. Theory Comput.*, vol. 11, no. 9, pp. 4294–4303, 2015.

[37] M. E. Casida, *Time-Dependent Density Functional Response Theory for Molecules*, ch. 5, pp. 155–192. Wiley Online Library, 1995.

[38] E. R. Davidson, "The iterative calculation of a few of the lowest eigenvalues and corresponding eigenvectors of large real-symmetric matrices," *J. Comp. Phys.*, vol. 17, no. 1, pp. 87–94, 1975.

Chapter 2. General Theory and Methodologies

As discussed in Chapter 1, many of the efforts of this dissertation are focused upon improving and interpreting calculated spectra obtained by real-time time-dependent density functional theory. Since Hartree-Fock (HF) or Self-Consistent Field methods are exact for the one-electron case, HF will be used as an introduction to electronic structure theory. All of the real-time response properties discussed in subsequent chapters are calculated in the time domain. Thus, it is important to provide a general introduction to the relevant time and frequency signal processing techniques used in this work. The subsequent chapters for each project contain additional information specific to their relevant techniques; however, this chapter serves merely to introduce these ideas to the general reader. Converting between time and frequency is a central theme of time-dependent properties; thus, this chapter also includes a brief review of Fourier transforms. Due to the Fourier uncertainty principle, transforming time signals can require long simulation times. To address this problem, a description of Padé approximants has been included. The extended discussion and some of the results employing the Padé acceleration technique have been included in Chapter 3.

2.1 The Hartree-Fock Method

2.1.1 The Fock Operator

Before delving into the details of density functional theory, it is first important to give a brief discussion of the foundations of relevant electronic structure calculations. Perhaps, one of the simplest solutions to the wavefunction is the Hartree-Fock method, which is exact for 1-electron systems like the hydrogen atom. Here, a description of HF has been included following the procedure outlined by Ostlund and Szabo.[1] To obtain the HF one-electron wavefunctions ϕ_i and their respective energies ϵ_i, Hartree-Fock solves an analogous Schrödinger equation using the one-electron Fock operator $\hat{f}(i)$:

$$\hat{f}(i)\phi_i = \epsilon_i\phi_i \tag{2.1}$$

where

$$\hat{f}(i) = \hat{h}_{\text{core}}(i) + \nu_{HF}(i) \tag{2.2}$$

Here, $\hat{H}_{\text{core}}(i)$ is the one-electron core Hamiltonian that represents kinetic energy and how electrons interact with the nucleus.

$$\hat{h}_{\text{core}}(i) = -\frac{1}{2}\nabla_i^2 - \sum_{\alpha} \frac{Z_\alpha}{r_{i\alpha}} \tag{2.3}$$

The second term of eq. 2.2, $\nu_{HF}(i)$ is the Hartree-Fock potential, which is the average potential experienced by the ith electron due to the field of the other electrons. This mean-field depends on the eigenvalues of each electron, and must therefore be solved iteratively. Thus, this solution to the Hartree-Fock eigenvalue problem is also commonly referred to as the Self-Consistent Field (SCF) method.

$$\nu_{HF}(i) = \sum_{j=1}^{N/2} [\hat{J}_j(i) - \hat{K}_j(i)] \tag{2.4}$$

Here, the HF potential is constructed of two operators. The first is the Coulomb ($\hat{J}_j(i)$), which as the name implies, yields the Coulombic repulsive interation of an electron in a given spin orbital with the mean field. This term is, of course, approximate because the mean-field approximation of electrons permits electrons to overlap or be non-physically close in space. As a result, the electrons are over-localized giving rise to higher calculated energies. The second operator, $\hat{K}_j(i)$ accounts for electron exchange. The exchange operator has no classical analogue; however, it accounts for the antisymmetry requirement of the wavefunction. Broadly speaking, that means that this operator accounts for the spin-flip operation for a given electron, ensuring that all electrons in the molecule are treated the same. Since there is no mean-field error for this term, the exchange operator is exact for the Hartree-Fock method.

2.1.2 Basis Sets and Matrix Representation

For all of the calculations performed for this work, atom-centered Gaussian basis sets[2,3] were used to describe the electron wavefunctions. These are ideal for energy calculations, however, perform poorly away from atoms and can become expensive for large systems such as solids. In such cases, grid-based calculations employing plane wave basis sets are more efficient.

For the use of Gaussian basis sets, the wavefunction can be constructed by following the prescription outlined in ref. 1:

$$\psi_i = \sum_{\mu=1}^{K} C_{\mu,i}\phi_\mu \qquad i = 1, 2, ..., K \tag{2.5}$$

where $C_{\mu,i}$ are the expansion coefficients that scale the basis functions ϕ_μ. Provided that the set of basis functions were complete, they would span the full space of the wavefunctions, and the expansion would be exact. Often, however, smaller basis sets are used to increase the speed of the calculations. Evaluating the expansion into eq. 2.1 in Bra-Ket notation,

$$\hat{f}(i) \sum_{\mu=1}^{K} C_{\mu,i} \left|\phi_\mu\right\rangle = \epsilon_j \sum_{\mu=1}^{K} C_{\mu,i} \left|\phi_\mu\right\rangle \tag{2.6}$$

and projecting onto the complex conjugate state $\langle\phi_i|$ yields

$$\sum_{\nu=1}^{K} C_{\mu,i} \left\langle\phi_\mu\right| \hat{f}(i) \left|\phi_\nu\right\rangle = \epsilon_j \sum_{\nu=1}^{K} C_{\mu,i} \left\langle\phi_\mu|\phi_\nu\right\rangle \tag{2.7}$$

In this two-index form, it is now possible to convert to matrix representation.

$$\mathbf{FC} = \mathbf{SC}\epsilon \tag{2.8}$$

Here, the overlap matrix is defined as $\mathbf{S}$ with elements

$$\mathbf{S}_{\mu\nu} = \langle \phi_\mu | \phi_\nu \rangle \tag{2.9}$$

and the Fock matrix as $\mathbf{F}$ with elements

$$\mathbf{F}_{\mu\nu} = \langle \phi_\mu | \, \hat{f}_i \, | \phi_\nu \rangle \tag{2.10}$$

In addition, $\mathbf{C}$ is the matrix expansion coefficients, and ϵ is the vector of corresponding energies.

One important property that can be determined from the wavefunctions is the charge density. Essentially, it is the probability of finding an electron in a specific region of space. By squaring the wavefunction for each electron, the charge density can be obtained by

$$\rho(\mathbf{r}) = 2 \sum_{a}^{N/2} |\psi_a(\mathbf{r})|^2 = 2 \sum_{a}^{N/2} \sum_{\nu\mu} C^\star_{\nu a} C_{\mu a} \langle \phi_{\nu a} | \phi_{\mu a} \rangle = \sum_{\mu\nu} \mathbf{P}_{\mu\nu} \langle \phi_{\nu a} | \phi_{\mu a} \rangle \tag{2.11}$$

where the density matrix $\mathbf{P}$ is defined as

$$\mathbf{P}_{\mu\nu} = 2 \sum_{a}^{N/2} C^\star_{\nu a} C_{\mu a} \tag{2.12}$$

Finally, the Fock matrix can be constructed by the one-electron core ($\mathbf{H}^{\text{core}}$) and the two-electron integrals from the Coulomb and exchange terms mentioned earlier. Each element of the Fock matrix can be obtained by

$$\mathbf{F}_{\mu\nu} = \mathbf{H}^{\text{core}}_{\mu\nu} + \sum_{\lambda\sigma} \mathbf{P}_{\lambda\sigma} [(\mu\nu|\lambda\sigma) - \frac{1}{2}(\mu\lambda|\sigma\nu)] \tag{2.13}$$

and the two-electron integral notation has been simplified by

$$(\mu\nu|\lambda\sigma) = \int \phi_\mu^\star(1)\phi_\nu(1)\frac{1}{r_{12}}\phi_\lambda^\star(2)\phi_\sigma(2)d\mathbf{r}_1 d\mathbf{r}_2 \tag{2.14}$$

Because the basis functions are not necessarily orthogonal to each other, there is overlap between the functions, which results in the overlap matrix, $\mathbf{S}$. To orthogonalize the functions with respect to each other, a transformation matrix $\mathbf{X}$ must be obtained

$$|\phi'_\mu\rangle = \sum_\nu \mathbf{X}_{\nu\mu}\,|\phi_\nu\rangle \qquad \mu = 1, 2, ..., K \tag{2.15}$$

such that

$$\langle\phi'^\star_\mu|\phi'_\nu\rangle = \delta_{\mu\nu} \tag{2.16}$$

Provided that the transformation matrix converts the orbitals into an orthonormal set, then transforming the overlap matrix into this basis will be unity:

$$\mathbf{X}^\dagger\mathbf{S}\mathbf{X} = \mathbf{1} \tag{2.17}$$

One way to obtain the transformation matrix is by canonical orthogonalization, which requires a unitary matrix $\mathbf{U}$. Since $\mathbf{S}$ is Hermitian, diagonalizing yields the unitary matrix and a diagonal matrix of overlap eigenvalues $\mathbf{s}$.

$$\mathbf{U}^\dagger\mathbf{S}\mathbf{U} = \mathbf{s} \tag{2.18}$$

In canonical orthogonalization, the transformation matrix is constructed by

$$\mathbf{X} = \mathbf{U}\mathbf{s}^{-1/2} \tag{2.19}$$

With this transformation matrix, it is now possible to convert the Hartree-Fock matrix expression into orthogonal space. To do so, the coefficient matrix is converted by

$$\mathbf{C}' = \mathbf{X}^{-1}\mathbf{C} \tag{2.20}$$

and the Fock matrix by

$$\mathbf{F}' = \mathbf{X}^{\dagger}\mathbf{F}\mathbf{X} \tag{2.21}$$

These are then evaluated into eq. 2.8 to yield

$$\mathbf{F}'\mathbf{C}' = \mathbf{C}'\epsilon \tag{2.22}$$

in an orthogonal basis. It is important to note that the overlap matrix in this basis is a unity matrix, which reduces the expression to a solvable eigenvalue problem.

2.1.3 SCF Algorithm

For a given molecular geometry and basis set, it is now possible in this formalism to perform a Hartree-Fock energy calculation. First, it will be important to determine the overlap, core hamiltonian, and two-electron integral matrices from eqs. 2.9, 2.3, and 2.14, respectively. Second, the overlap matrix must be diagonalized to construct a transformation matrix. Then, a guess for the coefficients of the $\mathbf{C}$ matrix is used to build an initial density matrix from eq. 2.12. The two-electron integrals, density matrix, and the core Hamiltonian matrix are then evaluated into eq. 2.13 to build the Fock matrix, which is then converted to the orthogonal basis by eq. 2.21. The $\mathbf{F}'$ matrix is diagonalized to obtain the eigenvalue energies, and the $\mathbf{C}'$ coefficients. Using eq. 2.20, these coefficients can be converted back to the original atomic orbital (AO) basis and evaluated back as the new guess for building the density matrix. This new density matrix is again used to construct a new Fock matrix, and the process is repeated until the density matrix is self consistent.

2.2 Time-Dependent Density Functional Theory

Although Hartree-Fock is exact for the one-electron case, the mean-field approximation results in errors in the Coulombic term, while the electron exchange remains exact. One approach called density functional theory attempts to correct for these overlocalization errors.

$$i\frac{\partial\psi_j(r,t)}{\partial t} = \Big[-\frac{1}{2}\nabla_j^2 + \nu_{\mathrm{HF}}(r,t) + \nu_{\mathrm{ext}}(r,t) + \nu_{\mathrm{xc}}[\rho](r,t)\Big]\psi_j(r,t) \tag{2.23}$$

Here, the Schrödinger equation is described as a system of noninteracting electrons satisfying the single-particle Kohn-Sham equations. This is accomplished by including the exchange-correlation potential term $\nu_{\mathrm{xc}}[\rho](r,t)$, which depends upon on the electron density (eq. 2.11). This term is a functional – or a function of a function – that depends upon the density, and it is important to note that the exchange-correlation potential is non-local spatially and temporally. Furthermore, it possesses a formal dependence not only on the initial total wavefunction, but also the entire history of the charge density, which will be a recurring topic in this dissertation.

2.2.1 Linear Response TDDFT

Presently, the majority of TDDFT calculations are perturbative in nature, and are calculated in a linear-response (LR) framework, often following a Casida description as outlined here.[4] Provided that the perturbation is small, the Hohenberg-Kohn theorem says that,

$$E_0 \leq F[\rho] + \int \nu_{\mathrm{ext}}(r,t)\rho(r,t)dr \tag{2.24}$$

Here, the perturbation functional $F[\rho]$ is reasonable for small changes in the density, and can be written formally as

$$F[\rho] = \min_{\Psi\to\rho} \frac{\langle\Psi|\hat{T}+\hat{V}_{ee}|\Psi\rangle}{\langle\Psi|\Psi\rangle} \tag{2.25}$$

Now consider a ficticious system of non-interacting electrons in which the density can be constructed of the orbital occupations (n_i) and corresponding orbitals ψ_i:

$$\rho(r) = \sum_i n_i \langle \phi_i | \phi_i \rangle \tag{2.26}$$

In this Kohn-Sham (KS) framework, an orthonormal set of orbitals are used to produce a charge density that is the same as it would be in a system of *interacting* electrons. Since the KS orbitals contain non-interacting electrons, the energies of each electron can be obtained similarly to those in Hartree-Fock.

$$E_{\mathrm{KS}} = T[\rho] + J[\rho] + E_{\mathrm{ext}}[\rho] + E_{\mathrm{xc}}[\rho] \tag{2.27}$$

As in Hartree-Fock, T is the kinetic term, J is the Coulombic term, and E_{ext} is the external forces term.

$$\begin{aligned} T[\rho] &= -\frac{1}{2} \sum_i \langle \psi_i | \nabla^2 | \psi_i \rangle \\ J[\rho] &= \frac{1}{2} \int \int \frac{\rho(r_1)\rho(r_2)}{r_{12}} dr_1 dr_2 \\ E_{\mathrm{ext}}[\rho] &= \int \nu_{\mathrm{ext}}(r,t)\rho(r,t) d\mathbf{r} \end{aligned} \tag{2.28}$$

The primary difference lies in the fourth term E_{xc}, called the exchange-correlation term.

$$E_{\mathrm{xc}}[\rho] = \min_{\Psi \to \rho} F[\rho] - \min_{\Phi_s \to \rho} \frac{\langle \Phi_s | \hat{T} | \Phi_s \rangle}{\langle \Phi_s | \Phi_s \rangle} - J_{xc}[\rho] \tag{2.29}$$

This term contains information from the electron exchange and correlation in addition to the disparity between the kinetic energies of interacting and noninteracting (KS) systems.

Taking the derivative with respect to the density yields the exchange correlation potential:

$$\nu_{\mathrm{xc}}(r,t) = \frac{\delta E_{\mathrm{xc}}\left[\rho(r,t)\right]}{\delta\rho(r,t)} \tag{2.30}$$

2.2.2 Perturbation Operator and LR-TDDFT

Often, it is of interest to calculate response properties in terms of the ground state orbitals. In order to extract such information, first consider the unperturbed system:

$$\hat{H}\Psi(r,t) = i\frac{\partial\Psi(r,t)}{\partial t} \tag{2.31}$$

Introducing a time-dependent perturbation operator $\hat{b}$ to the Hamiltonian and expanding the wavefunction (as $\Psi(r,t) = (\Psi((r)) + \delta\Psi(r,t) + ...)$) gives

$$(\hat{H} + \hat{b}(t))(\Psi((r)) + \delta\Psi(r,t)) = i\frac{\partial}{\partial t}(\Psi((r)) + \delta\Psi(r,t)) \tag{2.32}$$

where it has been assumed that the perturbation is in the linear regime to remove higher-order terms. Since the Hamiltonian operator requires a time-derivative (2.31) and the perturbation operator ($\hat{b}$) acts on the grounds state, the equation simplifies to

$$\hat{H}\delta\Psi(r,t) + \hat{b}(t)\Psi(r) = i\frac{\partial}{\partial t}\delta\Psi_0(r,t) + E_0\delta\Psi_0(r,t) \tag{2.33}$$

Now, grouping similar terms,

$$\hat{b}(t)\Psi_0(r) = (i\frac{\partial}{\partial t} + E_0 - \hat{H})\delta\Psi_0(r,t) \tag{2.34}$$

For first-order perturbation theory, Rayleigh-Schrödinger (RS) equations can be applied to quantum harmonic oscillators.[5] Since these oscillators are well-defined and can be normalized

in frequency space, a Fourier transform (FT) of eq. 2.33 is necessary. The FT yields

$$\hat{b}(w)\Psi_0(r) = (\omega + E_0 - \hat{H})\delta\Psi_0(r,\omega) \tag{2.35}$$

From RS, it is known that

$$\delta\Psi_0(r,\omega) = \sum_{i\neq 0} \Psi_i(r) \frac{\langle\Psi_i|\hat{b}(\omega)|\Psi_0\rangle}{\omega - \omega_i} \tag{2.36}$$

In other words, when the frequency of the oscillator (ω) is close to the frequency corresponding to the ith excitation energy, the more it contributes to the perturbation at that frequency. By assuming that the perturbation occurs for a single, given frequency (ω_0), the perturbation operator can be written as

$$\hat{b}(t) = b\cos(\omega_0 t) \tag{2.37}$$

or in the more relevant form

$$\hat{b}(\omega) = b\left[\delta(\omega - \omega_0) + \delta(\omega + \omega_0)\right] \tag{2.38}$$

within frequency space. Evaluating eq. 2.38 into eq. 2.39 and transforming back to the time domain produces

$$\delta\Psi_0(r,\omega) = \cos(\omega_0 t)\sum_{i\neq 0} \Psi_i \frac{\langle\Psi_i|\hat{b}(\omega)|\Psi_0\rangle}{\omega_0^2 - \omega_i^2} - i\sin(\omega_0 t)\sum_{i\neq 0} \Psi_i \frac{\langle\Psi_i|\hat{b}(\omega)|\Psi_0\rangle}{\omega_0^2 - \omega_i^2} \tag{2.39}$$

To obtain the linear perturbation of a given observable, $\delta\langle\hat{O}\rangle(t) = \langle\Psi_0|\hat{O}|\delta\Psi_0(t)\rangle + \langle\delta\Psi_0(t)|\hat{O}|\Psi_0\rangle$, which yields

$$\delta\langle\hat{O}\rangle(t) = \cos(\omega_0 t)\sum_{i\neq 0}\frac{\mathrm{Re}(\langle\Psi_0|\hat{O}|\Psi_i\rangle\langle\Psi_i|\hat{b}(\omega)|\Psi_0\rangle)}{\omega_0^2-\omega_i^2} + \sin(\omega_0 t)\sum_{i\neq 0}\frac{\mathrm{Im}(\langle\Psi_0|\hat{O}|\Psi_i\rangle\langle\Psi_i|\hat{b}(\omega)|\Psi_0\rangle)}{\omega_0^2-\omega_i^2} \tag{2.40}$$

2.2.3 Absorption Calculations from LR-TDDFT

In order to illustrate how to obtain information from LR perturbations, it is of interest to calculate absorption spectra. Although LR-TDDFT is not the emphasis of this dissertation, a brief discussion of such calculations will serve as a relevant primer to the content of Chapter 3, in which LR-TDDFT is used to validate RT-TDDFT spectral contributions. For this formalism, a perturbation will be applied to the density matrix in the frequency domain to capture the response associated with resonant transitions. Since transitions involve two orbitals, the perturbation will be constructed from the Coulomb and exchange-correlation contributions in a coupling term between states. This expression will be rewritten as an eigenvalue problem, where the solutions are perturbations to the density matrix. These perturbations are then used to construct the oscillator strength of absorption spectra.

Since the exchange correlation functional depends on the density, first consider that the response to any small change induced by an external, time-dependent field will result in a small perturbation in the electron density.

$$\delta\rho(\mathbf{r},\omega) = \sum_{\mu\nu}\delta\mathbf{P}_{\mu\nu}(\omega)\langle\phi_{\nu a}|\phi_{\mu a}\rangle \tag{2.41}$$

where the perturbation in the density matrix for a given orbital (a) can be expressed as

$$\delta\mathbf{P}_{\mu\nu a}(\omega) = \frac{C_{\nu a}-C_{\mu a}}{\omega-(\epsilon_\mu-\epsilon_\nu)}\langle\psi_{\mu a}|\hat{b}_{\mathrm{eff}}(\omega)|\psi_{\nu a}\rangle \tag{2.42}$$

To include changes as a response of the SCF, the effective perturbation operator is defined as $\hat{b}_{\text{eff}} = \hat{b} + \delta\nu_{\hat{\text{SCF}}}$ using $\hat{b}$ from eq. 2.38. In terms of matrices, this can be expressed as

$$\mathbf{b}^{\text{eff}}_{\mu\nu a}(\omega) = \langle\psi_{\mu a}|\hat{b}_{\text{eff}}(\omega)|\psi_{\nu a}\rangle = \mathbf{b}_{\mu\nu a}(\omega) + \sum \mathbf{K}_{\mu\nu a,\lambda\sigma\tau}\delta\mathbf{P}_{\lambda\sigma\tau}(\omega) \tag{2.43}$$

where the perturbation in the SCF potential for orbital (a) due to changes in a second orbital (τ) is represented across two sets of basis functions through the coupling matrix $\mathbf{K}$. Since the potential relates two electrons, this coupling can be described by two-electron integrals for the "Hartree-like" Coulomb term (f_{H}) and the DFT exchange correlation term $(f^{a,\tau}_{\text{xc}})$.

$$\mathbf{K}_{\mu\nu a,\lambda\sigma\tau} = \frac{\partial\nu^{\text{SCF}}_{\mu\nu a}}{\partial\mathbf{P}_{\lambda\sigma\tau}} = (\mu\nu|f_{\text{H}}|\lambda\sigma) + \delta_{a,\tau}(\mu\nu|f^{a,\tau}_{\text{xc}}|\lambda\sigma) \tag{2.44}$$

At this point, it is important to mention that this form of the coupling matrix accounts for the full time history of the density. If the full history were known, it would be possible to calculate perturbations of the DFT exchange correlation relative to those from past densities. Unfortunately, a full history of electron density is not available. To resolve this issue the adiabatic approximation is applied here, which assumes that the density does not change significantly. Since a LR-TDDFT simulation only slighly perturbs the system, this is a reasonable assumption here. Now, the exchange correlation contribution to the coupling matrix becomes $(\mu\nu|f^{a,\tau}_{\text{xc}}|\lambda\sigma)$.

With the perturbation matrix $(\mathbf{b}^{\text{eff}}_{\mu\nu a})$ defined, it can now be evaluated into eq. 2.42.

$$\delta\mathbf{P}_{\mu\nu a}(\omega) = \frac{C_{\nu a} - C_{\mu a}}{\omega - (\epsilon_\mu - \epsilon_\nu)}\left[\mathbf{b}_{\mu\nu a}(\omega) + \sum \mathbf{K}_{\mu\nu a,\lambda\sigma\tau}\delta\mathbf{P}_{\lambda\sigma\tau}(\omega)\right] \tag{2.45}$$

Multiplying by the reciprocal of the resonance prefactor yields

$$\frac{\omega - (\epsilon_\mu - \epsilon_\nu)}{C_{\nu a} - C_{\mu a}}\delta\mathbf{P}_{\mu\nu a}(\omega) = \mathbf{b}_{\mu\nu a}(\omega) + \sum \mathbf{K}_{\mu\nu a,\lambda\sigma\tau}\delta\mathbf{P}_{\lambda\sigma\tau}(\omega) \tag{2.46}$$

which can be rewritten as

$$-\sum\left[\mathbf{K}_{\mu\nu a,\lambda\sigma\tau}\delta\mathbf{P}_{\lambda\sigma\tau}(\omega)\right]+\frac{\omega-(\epsilon_\mu-\epsilon_\nu)}{C_{\nu a}-C_{\mu a}}\delta\mathbf{P}_{\mu\nu a}(\omega)=\mathbf{b}_{\mu\nu a}(\omega) \tag{2.47}$$

To simplify this expression, it is necessary to change the perturbation basis for orbital τ to be the same as orbital a. This can be accomplished by expanding the perturbation in the space described by the set of functions $\{\mu,\nu\}$.

$$\sum_{\lambda\sigma a}^{C_{\mu a}\neq C_{\nu a}}\left[\delta_{a,\tau}\delta_{\mu,\lambda}\delta_{\nu,\sigma}\delta\mathbf{P}_{\lambda\sigma\tau}(\omega)\right]=\delta\mathbf{P}_{\mu\nu a}(\omega) \tag{2.48}$$

Here, the summation does not include the space for $\mu=\nu$ because no transitions occur between a given orbital and itself in this representation (e.g., no HOMO→HOMO transitions). This summation can then be evaluated into eq. 2.47, and like-terms are grouped to produce

$$\sum_{\lambda\sigma a}^{C_{\mu a}\neq C_{\nu a}}\left[\frac{\omega-(\epsilon_\mu-\epsilon_\nu)}{C_{\nu a}-C_{\mu a}}\delta_{a,\tau}\delta_{\mu,\lambda}\delta_{\nu,\sigma}-\mathbf{K}_{\mu\nu a,\lambda\sigma\tau}\right]\delta\mathbf{P}_{\lambda\sigma\tau}(\omega)=\mathbf{b}_{\mu\nu a}(\omega) \tag{2.49}$$

To obtain the density response from this expression, it is again convenient to use matrices. Elements of two simplifying matrices can be defined as

$$\begin{aligned}A_{\mu\nu a,\lambda\sigma\tau}&=\delta_{a,\tau}\delta_{\mu,\lambda}\delta_{\nu,\sigma}(\epsilon_\mu-\epsilon_\nu)+K_{\mu\nu a,\lambda\sigma\tau}\\B_{\mu\nu a,\lambda\sigma\tau}&=K_{\mu\nu a,\sigma\lambda\tau}\end{aligned} \tag{2.50}$$

Since each of the remaining transitions for occupied to virtual states ($i\rightarrow a$, $\mu\rightarrow\lambda$) do not cause a large change in the occupations, then the occupied states will take values of 1 and the virtual states will take values of 0. With this assumption, it is then possible to write eq. 2.49 in the form

$$(-1)\omega-\mathbf{A}\delta\mathbf{P}(\omega)-\mathbf{B}\delta\mathbf{P}^*(\omega)=\mathbf{b}(\omega) \tag{2.51}$$

and the corresponding

$$(+1)\omega - \mathbf{B}^*\delta\mathbf{P}(\omega) - \mathbf{A}^*\delta\mathbf{P}^*(\omega) = \mathbf{b}^*(\omega) \tag{2.52}$$

where the prefactor (± 1) and conjugate forms result from the direction of excitation or de-exciation (e.g. HOMO→LUMO vs. LUMO→HOMO). This can be written more compactly as

$$\left\{ \omega \begin{bmatrix} -1 & 0 \\ 0 & +1 \end{bmatrix} - \begin{bmatrix} \mathbf{A} & \mathbf{B} \\ \mathbf{B}^* & \mathbf{A}^* \end{bmatrix} \right\} \begin{pmatrix} \delta\mathbf{P}(\omega) \\ \delta\mathbf{P}^*(\omega) \end{pmatrix} = \begin{pmatrix} \mathbf{b}(\omega) \\ \mathbf{b}^*(\omega) \end{pmatrix} \tag{2.53}$$

When the driving frequency is resonant with an excitation, the response of the density matrix becomes infinite. This condition is true even in the case of infinite perturbation. Thus, for a resonant transition, the perturbation ($\mathbf{b}(\omega)$) is negligible by comparison.

$$\omega \begin{bmatrix} -1 & 0 \\ 0 & +1 \end{bmatrix} \begin{pmatrix} \delta\mathbf{P}(\omega) \\ \delta\mathbf{P}^*(\omega) \end{pmatrix} = \begin{bmatrix} \mathbf{A} & \mathbf{B} \\ \mathbf{B}^* & \mathbf{A}^* \end{bmatrix} \begin{pmatrix} \delta\mathbf{P}(\omega) \\ \delta\mathbf{P}^*(\omega) \end{pmatrix} \tag{2.54}$$

To simplify, rewrite this expression as an eigenvalue problem. Here, for an operator

$$\hat{O} = (\mathbf{A} - \mathbf{B})^{1/2}(\mathbf{A} + \mathbf{B})(\mathbf{A} - \mathbf{B})^{1/2} \tag{2.55}$$

and the eigenfunction

$$\mathbf{F} = (\mathbf{A} - \mathbf{B})^{-1/2}(\delta\mathbf{P} + \delta\mathbf{P}^*) \tag{2.56}$$

the resonant matrix expression (eq. 2.54) becomes

$$\hat{O}\mathbf{F} = \omega^2\mathbf{F} \tag{2.57}$$

Solutions to this eigenvalue problem are then obtained by iterative Davidson-Krylov[6] methods, since the combinatorial space is often to large for conventional techniques. The eigen values correspond to the transition frequencies, and the eigenvectors contain the density perturbations and orbital couplings. As such, for a given resonant frequency, the corresponding oscillator strength can be obtained by

$$S(\omega) = \frac{2}{3} \sum_{r=x,y,z} |r(\delta\mathbf{P} + \delta\mathbf{P}^*)|^2 = \frac{2}{3} \sum_{r=x,y,z} |r(\mathbf{A} - \mathbf{B})^{1/2}\mathbf{F}|^2 \tag{2.58}$$

2.2.4 Real-Time TDDFT

Although Linear-Response TDDFT is widely used for electronic structure calculations, it assumes only weak perturbations to the electron density. Furthermore, as discussed in the derivation, the density response is obtained in the frequency domain and lacks truly time-dependent dynamical information. For much of the work in this dissertation, it is of interest to track the time-dependent density and electron dynamics. This information can be determined by real-time TDDFT, which explicitly propagates the electron density in the time domain.[7] Again, in a Kohn-Sham (KS) framework, an orthonormal set of basis functions yields a charge density that is the same as for a system of interacting electrons, and thus, the energies are calculated similarly to those of Hartree-Fock.

$$E_{\mathrm{KS}}(r,t) = T[\rho(r,t)] + J[\rho(r,t)] + E_{\mathrm{ext}}[\rho(r,t)] + E_{\mathrm{xc}}[\rho(r,t)] \tag{2.59}$$

Here, however, the KS electron energies are time-dependent, as the density evolves in time. As before, E_{ext} is the energy due to an external potential (e.g., from a time-dependent electic field), and the Hartree potential describes the Coulombic interactions,

$$J[\rho(r,t)] = \frac{1}{2} \int\int \frac{\rho(r_1,t)\rho(r_2,t)}{r_{12}} dr_1 dr_2 \tag{2.60}$$

The exchange-correlation term is also be time-dependent. In other words, the time-dependent density be evaluated into the functional at each time step to obtain the exchange-correlation potential.

$$\nu_{\mathrm{xc}}^{\mathrm{adiab.}} = \nu_{\mathrm{xc},0}[\rho](r)|_{\rho=\rho(t)} \tag{2.61}$$

It is important to note that the adiabatic approximation has been employed here for simplicity, as it permits the use of the $t = 0$ exchange-correlation functional at all times. This approximation and associated pathologies are discussed in more detail in section 2.3.

To calculate how the density changes in time, start a von Neumann representation of the equation of motion, as discussed in ref. 8.

$$-i\frac{\partial \mathbf{P}'(t)}{\partial t} = [\mathbf{F}'(t), \mathbf{P}'(t)] \tag{2.62}$$

where $\mathbf{F}'(t)$ and $\mathbf{P}'(t)$ are the Fock matrix and density matrix, respectively. Recall that the prime denotes the canonical basis, since an orthogonal representation is necessary for propagation. Although there are several ways to integrate eq. 2.62, the second-order Magnus (exponential midpoint) propagator has been used for this work because it is accurate and efficient for large time steps.

$$\mathbf{P}'(t + \Delta t) = e^{\Omega}\mathbf{P}'(t)e^{-\Omega} \tag{2.63}$$

where

$$\Omega \equiv -i\mathbf{F}'\left(t + \frac{\Delta t}{2}\right)\Delta t \tag{2.64}$$

Essentially, eq. 2.64 calculates the density at a future time step. Since the future Fock matrix $\mathbf{F}'\left(t + \frac{\Delta t}{2}\right)$ is not expressly known, it is obtained by extrapolating the previous two times, propagating one time step into the future, and interpolating until the future Fock matrix is

self-consistent. From the calculated density matrices, the density can be calculated as before by eq. 2.11.

2.2.5 Absorption Calculations for RT-TDDFT

In particular, it is of interest to obtain absorption information from a real-time TDDFT calculation. Here, a general introduction to time-dependent absorption theory has been included. Expanded descriptions of other useful properties will be discussed in subsequent chapters, as they are introduced.

Recall from linear response absorption calculations, that all of the transitions are obtainable by interatively solving the perturbation eigenvalue problem (eq. 2.54). In order to get all of the excitations in a real-time calculation, it is necessary to excite all of the modes at once. Since each transition in a molecule is quantized, it has a specific frequency associated with it. Thus, to excite all modes, an applied electric field pulse needs to be narrow in time or broad in frequency. Such fields are often artificially represented as a Dirac delta function, which probes all transitions:

$$\mathbf{E}(t) = \kappa\delta(t)\hat{\mathbf{d}} \tag{2.65}$$

Here, κ denotes the field amplitude and $\hat{\mathbf{d}} = \{\hat{x}, \hat{y}, \hat{z}\}$. Provided that the frequency of the incident light is low, the applied field can be assumed relatively constant over the molecule. When that assumption is true, the electric field ($\mathbf{E}(t)$) can be coupled to the Fock matrix (eq. 2.10) by

$$\mathbf{V}(t) = -\mathbf{D} \cdot \mathbf{E}(t) \tag{2.66}$$

where $\mathbf{D}$ is the dipole tensor. The elements of the dipole tensor represent the direction-specific projections of one state onto another, such that

$$\mathbf{D}_{a,b,d} = \langle\psi_b|\hat{\mathbf{d}}|\psi_a\rangle \tag{2.67}$$

If the applied field is not strong enough to Stark-shift the orbitals, the time-dependent dipole can be obtained by projecting the density matrix (eq. 2.12) onto the dipole tensor.

$$\mu_d(t) = \mathrm{Tr}[\mathbf{M}(t)] = \mathrm{Tr}[\mathbf{D}_d\mathbf{P}(t)] \tag{2.68}$$

By taking the Fourier transform of the time-dependent dipole signal and electric field, it is possible to calculate the dipole polarizability ($\alpha_{dd}(\omega)$).

$$\alpha_{dd} = \frac{\mu_d(\omega)E_d^*(\omega)}{E_d(\omega)E_d^*(\omega)} = \frac{\mu_d(\omega)E_d^*(\omega)}{|E_d(\omega)|^2} \tag{2.69}$$

It is important to note that the multiplication and division by the complex conjugate (asterisk) of the electric field accounts for any phase ripples in the frequency spectrum due to a time-shifted excitation. Using these polarizabilities, the oscillator strengths of the dipole response can now be obtained.

$$S(\omega) = \frac{4\pi\omega}{3c}\mathrm{Im}[\alpha_{xx}(\omega) + \alpha_{yy}(\omega) + \alpha_{zz}(\omega)] \tag{2.70}$$

2.3 The Adiabatic Approximation

One major challenge in density functional theory calculations involves the history dependence or "memory" of the DFT functional. Provided that the electron density does not change significantly, the converged self-consistent field (SCF) ground state density can be evaluated into the DFT functional. The assumption that this density does not dramatically change is referred to as the adiabatic approximation. While this is not generally a concern for perturbative or ground state calculations, excited states can often involve large changes in the density, yielding sizable errors in a TDDFT simulation. (See fig. 2.1) In Chapter 4, the development and implementation of well-defined initial states are used to avoid many of

the problems introduced by the adiabatic approximation and large changes to the electron density, specifically during excitation. Although these well-defined initial states remain subject to the adiabatic approximation, they are representative of the true excited states of a system, and lack the large changes introduced to the density during a resonant excitation.

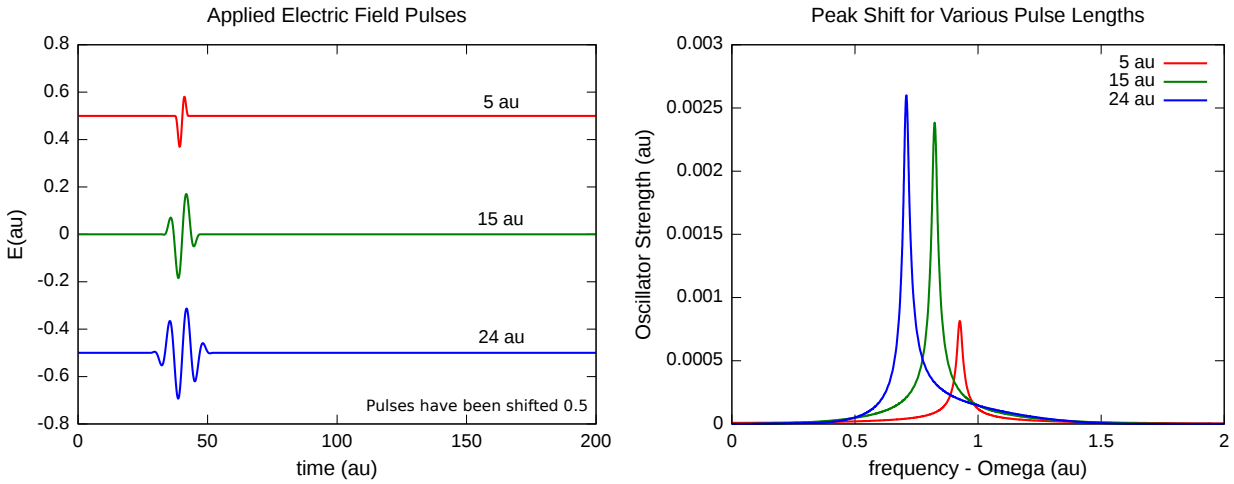

Figure 2.1: Three applied pulses of increasing duration (Left) were used to excite an H_2 molecule. Each pulse of 5, 15, and 24 as has the same frequency at 0.936 au., which should excite more population into the same resonant excited state. The corresponding TDDFT responses (Right) show that longer pulse duration does increase the population; however, the resonant frequency red shifts to lower energies due to the adiabatic approximation.

To illustrate the potential errors resulting from the adiabatic approximation in RT-TDDFT, consider a broadband excitation for a hydrogen molecule. To probe as many frequencies as possible, a Dirac delta function can be used. Such a pulse will be infinitely narrow in time, and consequently, infinitely broad in frequency following a Fourier transform. From such a delta "kick," H_2 shows an absorption peak at $\sim$0.936 au in energy (25.5 eV). Since there is an absorption at this frequency, now consider a new case in which a Gaussian enveloped pulse is applied at this frequency. Extending the pulse duration should result in increased population of the excited state. If three applied pulses at this frequency with different pulse durations (FWHM), then the longest pulse should excite more population from the ground to excited state. Unfortunately, in the process, if the charge density changes

significantly, large errors develop in from the DFT functional. An example of this can be observed by shifting of the absorption peak. Although this can cause major problems for excited state calculations, Chapters 3 and 4 introduce a way to address these challenges.

2.4 Signal Processing and Transforms

2.4.1 Fourier Transformation

The Fourier transform is a powerful tool for obtaining the relevant frequencies and associated dynamics from a time-dependent calculation. To help understand the ideas of the Fourier transform, consider playing music. When a single note is played, it has a specific frequency corresponding to a given designation such as an $A^{\flat}$ or a $D^{\sharp}$. A different harmonic occurs by shifting up or down an octave in pitch, and playing multiple notes together produces a chord. If it were of interest to know which notes were played just by listening, it would be necessary to convert the time-dependent sound wave into its respective frequencies. The mathematical conversion between the time-dependent wave and the corresponding frequencies is often described by a Fourier transform.

$$\mathcal{F}(\omega) = \frac{1}{\sqrt{2\pi}} \int_{-\infty}^{\infty} f(t) e^{-i\omega t} dt \tag{2.71}$$

Here, it is important to note that small step-sizes are often necessary to avoid aliasing effects in the transformed signal. Aliasing occurs when a set of time points fails to adequately sample a high-frequency signal, instead yielding a spurious lower frequency in the Fourier transform. This can be avoided by a step size smaller than half of the desired maximum period ($T/2$), yet for the work of this dissertation a more stringent condition was used.

$$dt = 0.1T \tag{2.72}$$

The time step is denoted as dt and the period of the oscillation is T, where

$$T = \frac{2\pi}{\omega} \tag{2.73}$$

This ensures that frequencies at or below a threshold frequency (ω) are captured.

2.4.2 The Fourier Uncertainty Principle

Prior to the discussion of the research and efforts of subsequent chapters, some of the motivating challenges and relevant problems with TDDFT calculations should be introduced. Firstly, real-time (RT-TDDFT)) calculations often require a large amount of time signal to yield converged frequency spectra, often referred to as the Fourier uncertainty principle. (See fig. 2.2) This issue is worsened by the small time-steps required by the density propagators.

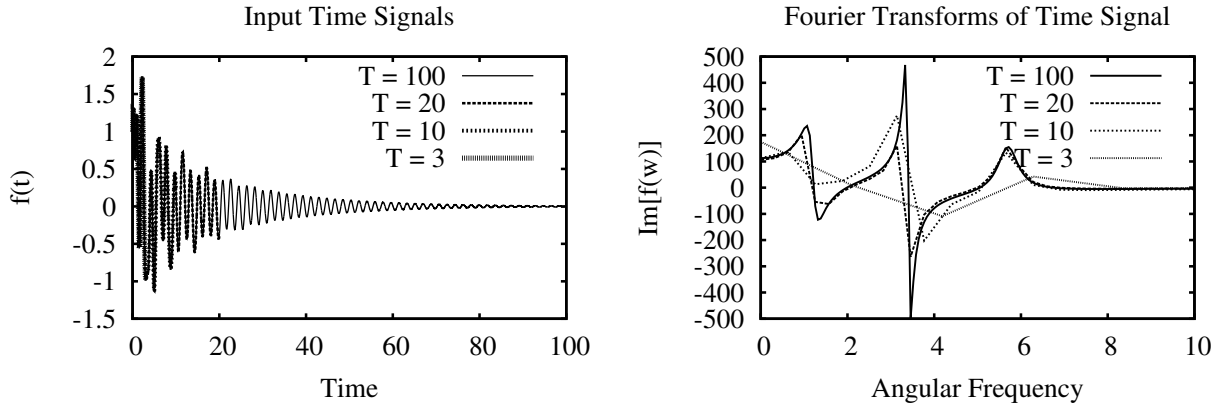

Figure 2.2: Four propagation times of the same damped oscillator signal have been Fourier transformed from the time domain (Left) into the frequency domain (Right). Due to the Fourier uncertainty principle, shorter propagation times do not have enough oscillations to capture lower frequencies effectively. As the number of propagation time points increases, the frequency spectrum converges to the infinite-time result.

Although many numerical propagators exist, they often balance a larger time-step with a slower point convergence. Furthermore, large time-steps can introduce aliasing effects in the transformed spectra. To address the long simulation time requirement, Chapter 2 introduces a numerical signal processing technique, which is used to accelerate the transform conver-

gence. In Chapter 3, this technique is used to dramatically reduce simulation times while also providing accurate real-time spectral contributions, akin to those from LR-TDDFT.

2.4.3 Padé Approximants to Fourier Transforms

In addition to the time step, these transforms also depend heavily upon the number of oscillations due to the Fourier uncertainty principle. As the cycle number increases, the resolution in the frequency data improves. Thus, as mentioned above, a long time simulation is often required for fully resolved frequency spectra. To avoid such costly simulations, Padé approximants[9–11] essentially use a ratio of coefficients to fit a short amount of time data as a means to extrapolate more.[12]

$$\mu(z) = \frac{\Sigma_{k=0}^{N} a_k z^k}{\Sigma_{k=0}^{N} b_k z^k} \tag{2.74}$$

The set of b_k coefficients provide additional flexibility to capture poles in the signal more effectively than traditional fitting functions. Once the sets of a_k and b_k coefficients are known, the discrete Fourier transform can be populated to any spectral density. While several fitting methods exist, Padé approximants have been chosen for convenience and relevance to Chapter 3, which contains additional details on the methodology and implementation. It is

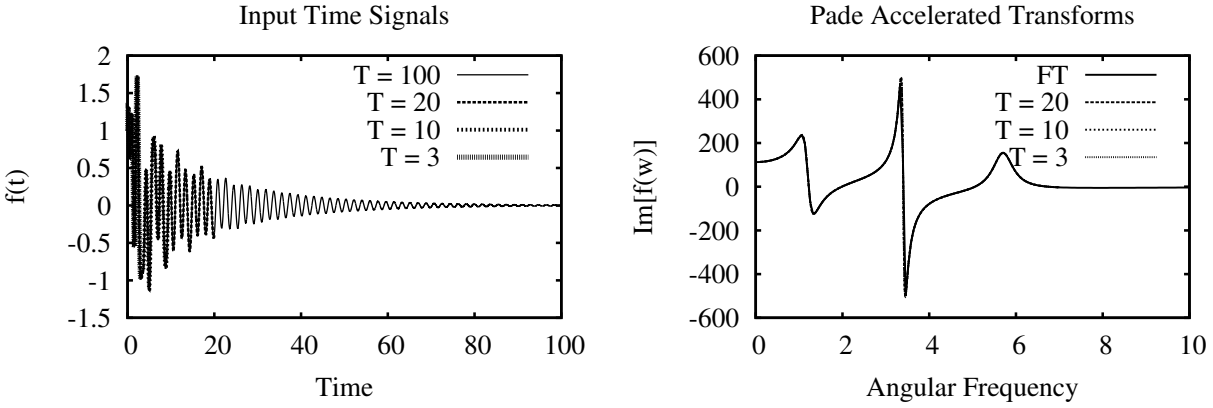

Figure 2.3: Four propagation times of the same signal have been Padé transformed from the time domain (Left) to the frequency domain (Right). Unlike the conventional Fourier transform (Fig. 2.2), the Padé accelerated transform is converged even for very small propagation times.

important to mention that for very small data sets, Padé approximants do not capture the response (Fig. 2.3); however, this can be avoided by checking the time convergence since the frequency response should not change for increasing time data if there is a sufficient number of time points.

2.5 References

[1] A. Szabo and N. S. Ostlund, *Modern quantum chemistry: Introduction to advanced electronic structure theory*. Courier Corporation, 1989.

[2] R. Krishnan, J. S. Binkley, R. Seeger, and J. A. Pople, "Self-consistent molecular orbital methods. xx. a basis set for correlated wave functions," *J. Chem. Phys.*, vol. 72, no. 1, pp. 650–654, 1980.

[3] T. H. Dunning Jr, "Gaussian basis sets for use in correlated molecular calculations. i. the atoms boron through neon and hydrogen," *J. Chem. Phys.*, vol. 90, no. 2, pp. 1007–1023, 1989.

[4] M. E. Casida, *Time-Dependent Density Functional Response Theory for Molecules*, ch. 5, pp. 155–192. Wiley Online Library, 1995.

[5] E. Schrödinger, "Quantisierung als eigenwertproblem," *Annal. Phys.*, vol. 385, no. 13, pp. 437–490, 1926.

[6] E. R. Davidson, "The iterative calculation of a few of the lowest eigenvalues and corresponding eigenvectors of large real-symmetric matrices," *J. Comp. Phys.*, vol. 17, no. 1, pp. 87–94, 1975.

[7] E. Runge and E. K. U. Gross, "Density-functional theory for time-dependent systems," *Phys. Rev. Lett.*, vol. 52, pp. 997–1000, Mar 1984.

[8] K. Lopata and N. Govind, "Modeling fast electron dynamics with real-time time-dependent density functional theory: Application to small molecules and chromophores," *J. Chem. Theory Comput.*, vol. 7, no. 5, pp. 1344–1355, 2011.

[9] A. George Jr, *Essentials of Padé approximants*. Elsevier, 1975.

[10] S. Dey and R. Mittra, "Efficient computation of resonant frequencies and quality factors of cavities via a combination of the finite-difference time-domain technique and the padé approximation," *IEEE Microw. Guided W.*, vol. 8, no. 12, pp. 415–417, 1998.

[11] W.-H. Guo, W.-J. Li, and Y.-Z. Huang, "Computation of resonant frequencies and quality factors of cavities by fdtd technique and padé approximation," *IEEE Microw. Wirel. Co.*, vol. 11, no. 5, pp. 223–225, 2001.

[12] A. Bruner, D. LaMaster, and K. Lopata, "Accelerated broadband spectra using transition dipole decomposition and padé approximants," *J. Chem. Theory Comput.*, vol. 12, no. 8, pp. 3741–3750, 2016.

Chapter 3. Accelerating Broadband Spectra Using Transition Dipole Decomposition and Padé Approximants

3.1 Introduction

Within this chapter, we present a method for accelerating the computation of UV-Visible and X-ray absorption spectra in large molecular systems using real-time time dependent density functional theory (TDDFT).[1] The approach is based on deconvolution of the dipole into molecular orbital dipole pairs developed by Repisky, et al,[2,3] followed by Padé approximants to their Fourier transforms. By combining these two techniques, the required simulation time is reduced by a factor of five or more, and moreover, the transition dipoles yield the molecular orbital contributions to each transition, akin to the coefficients in linear-response TDDFT. We validate this method on valence and core-level spectra of gas-phase water and nickel porphyrin, where the results are essentially equivalent to conventional linear response. This approach makes real-time TDDFT competitive against linear response for large molecular and material systems with a high density of states.

Modeling electronic spectroscopy and dynamics in molecules and materials is important for elucidating excited state mechanisms, for predicting dynamical properties, and for interpreting experimental results. Typically, excited state simulations are solved in the frequency domain assuming weak perturbation from the ground state. Real-time methods, where the wavefunction is explicitly integrated in time, are less common but can be simpler to implement and are valid for non-linear response. These span the gamut of electronic structure approaches including: semi-empirical methods[4,5], Hartree-Fock[6–8], time-dependent density functional theory[9–18], configuration interaction[19–21], multi-configurational self-consistent field[22–24], coupled cluster[25,26], and two-electron reduced density matrix methods[27].

Time-dependent density functional theory[28,29] is perhaps the most popular general purpose excited state method due to the generally favorable tradeoff between accuracy and com-

This chapter has been reprinted with minor changes from its original format in Bruner, A., LaMaster, D., Lopata, K., J. Chem. Theory Comput., 2016, 12 (8), pp 3741-3750. with permission by the authors and the journal.

putation cost. Care must be taken, however, as results can be sensitive to the choice of DFT functional, and in extreme cases pathologies in the functional can yield qualitatively wrong results. Regardless, much progress has been made towards extending TDDFT to a range of challenging excitations including charge transfer[30,31], double excitations[32], strong-field ionization[33,34], above-threshold resonances[35], core-level spectra[36,37], hyperpolarizabilities[38], and excited state absorption[39].

In the case of weak excitations, such as absorption spectroscopy, where the applied fields are weaker than the internal molecular fields, the molecular response can be obtained via perturbative quantum calculations. Linear-response (LR) TDDFT essentially consists of finding roots in the frequency-dependent molecular response by assuming a small change in the electron density from the ground state[40,41]. Practical implementations typically use the Casida approach[40] where Davidson iterations are performed[42]to obtain the eigenvalues and eigenvectors of the linear response matrix. Frequency domain LR-TDDFT calculations yield both the spectral information (peak energies and oscillator strengths) from the eigenvalues, as well as the composition of each peak, e.g., which molecular orbitals are involved in each transition, from the corresponding eigenvectors.[40] On the other hand, these root-based methods can face convergence issues and may require a prohibitively large number of roots in systems with a high density of states. Approximate linear-response solvers such as Lanczos methods[43] offer promise for extending LR-TDDFT to very large systems.

An alternative approach to computing weak-field spectra is real-time (RT) TDDFT, where the time-dependent wavefunction (or density matrix) is propagated in time, typically following broad-band (narrow pulse) excitation. Although they compute nearly equivalent information, real-time propagation can have many advantages over frequency domain techniques. First, RT simulations yield the full absorption spectrum spanning valence to core with only three simulations (x, y, z polarizations). If there are no magnetic fields and if the light is linearly polarized and all polarizations are in phase, then the three simulations

can be condensed down to one, provided that the molecule is not planar and not oriented along a resultant field vector. Rather than calculating the entire absorption spectrum at once, LR only computes a finite number of roots. This makes RT especially advantageous for systems with a high density of states, where LR would require potentially thousands of roots to generate a spectrum[44,45]. Furthermore, polarization-specific transformations to frequency space converge to resolved spectra more quickly than the total since they do not contain as many frequencies.

Additionally, real-time propagation is inherently non-linear and can thus extend TDDFT to strong-field dynamics and nonlinear spectra where the system is driven far from the ground state. By tracking the electron dynamics as they evolve as a response to the laser fields, real-time simulations can shed light on excited state absorption, high harmonic generation, and attosecond transient absorption. Here, the adiabatic (local-in-time) approximation for the DFT functional can be especially problematic, and in extreme cases even adiabatically-exact functionals are insufficient[46,47]. The validity of TDDFT for these dynamics, and development of memory functionals, remains a topic of ongoing study.

Despite these obvious advantages, there are numerous limitations to real-time TDDFT for spectroscopy applications. Firstly, real-time simulations are generally more time consuming than comparable linear-response ones. Due to the short time scales of electronic dynamics, short integrator time steps are usually required, typically $\Delta t < 10$ as or even shorter for high frequency electronic responses (e.g., X-ray absorption). Compounding this problem, long time signals are required to adequately resolve spectral features of similar energies, which can lead to lengthy simulation times for even modestly sized systems. The cost of RT-TDDFT versus comparable frequency domain techniques becomes increasingly favorable as system sizes increases, but even for large systems, it is typically at least five times slower than LR-TDDFT[45].

There are numerous approaches to accelerating spectral convergence of time signals (harmonic inversion[48]) such as Prony's method, Filter Diagonalization[49–51], Padé approximants[52–54], and linear predictors[55,56]. These tools are employed in applications spanning wavepacket dynamics[57], molecular dynamics[56], classical electrodynamics[53,54], and NMR[51]. Filter Diagonalization, for example, essentially fits the time signal to a series of damped oscillators and excels at spectra with a few dominant modes, but it can have convergence issues for highly dense spectra and is unsuitable for non-Lorentzian lineshapes. Linear predictors make no assumptions about the functional form, but struggle with irregular time signals and typically require small time steps to converge well. Padé approximants fit the short time signal to a ratio of polynomials, which captures poles effectively and requires no assumption about functional form, which makes them suitable for non-Lorentzian lineshapes.

Another drawback of a real-time approach is the difficulty associated with interpreting spectra. Constructing an absorption spectrum from the Fourier transform of the dipole moment gives the frequency-dependent absorption cross section, but this spectrum does not contain information about the molecular orbitals involved in each transition. Linear response TDDFT, on the other hand, directly yields the occupied-virtual contributions through the coefficients.

The simplest way to interpret RT spectra is to visualize the excitations by exciting the system with narrow-band quasi-monochromatic excitations and tracking the deviation of the charge density from the ground state[17,36]. This must be done on a peak-by-peak basis, however, and also requires very long pulses and simulation times to selectively excite only a single mode. A more elegant approach is to compute the Fourier transform of the 3D time-dependent density fluctuations, which give transition density plots at frequencies of interest[58]. This approach offers both graphical and quantitative transition information, but requires a Fourier transform at each point in space, and has difficulty deconvoluting nearby peaks, especially for dense spectra. Another approach consists of projecting the density

matrix onto the ground state to deconvolute the dipole moment into separate time-dependent transition dipole moments corresponding to transitions between MO pairs developed by Repisky, et al[2,3].

In this paper we develop a method for accelerating real-time TDDFT calculations by combining Padé approximants and decomposition of the total diple into MO pair transition dipoles. The Padé acceleration technique, however, can have convergence issues for congested dipole signals. The key here, is to first deconvolute the dipole moment into the MO pair transitions before acceleration. Since the spectrum of each MO pair transition is far less dense than the full spectrum, each of these can be independently converged even for very short signals, which allows for simulation times at least five times shorter than traditional Fourier transforms. Moreover, the relative areas under each peak correspond to the MO contribution to an excitation at that frequency, which gives a clear physical interpretation of each excitation that is consistent with linear response. This combination of interpretation and simulation speedup makes these RT-TDDFT simulations competitive with LR-TDDFT, especially for large systems with many transitions, or for systems where Davidson iterations have difficulty converging.

The rest of this paper takes the following form. In Sec. 3.2 we present the details of the approach, including time propagation, MO deconvolution, and signal processing. In Sec. 3.3 we validate this approach versus LR-TDDFT for valence and core-level spectroscopy for a water molecule and a zinc porphyrin, and benchmark the speedups due to Padé acceleration. Finally, we summarize in Sec. 3.4.

3.2 Methods

In this section we outline the details of the approach including bases used (Sec. 3.2.1), time propagation of the density matrix (Sec. 2.2.4), normalization of signal from a time-shifted electric field (Sec. 3.2.2), spectral decomposition into occupied–virtual MO contributions (Sec. 3.2.3), and acceleration of convergence using Padé approximants (Sec. 3.2.4).

3.2.1 Atomic, Canonical, and Molecular Orbital Bases

Before discussing the formal approach we first distinguish between the three different bases used: The atomic orbital (AO) basis, which we denote with unprimed notation, is non-orthogonal and is used to construct the operators (e.g., transition dipole and Fock matrices) in terms of the Gaussian-type orbitals. For clarity, the notation has been chosen to be consistent with Chapter 1. All AO basis operators are size $n \times n$, where n is the number of basis functions.

The canonical orbital (CO) basis, denoted with a prime, is an orthogonal basis used for time propagation. AO↔CO conversions use canonical orthogonalization of the Fock ($\mathbf{F}$) and density ($\mathbf{P}$) matrices[17,59]:

$$\begin{aligned} \mathbf{F}' &= \mathbf{X}^\dagger \mathbf{F} \mathbf{X} \\ \mathbf{F} &= \mathbf{Y} \mathbf{F}' \mathbf{Y}^\dagger \\ \mathbf{P}' &= \mathbf{Y}^\dagger \mathbf{P} \mathbf{Y} \\ \mathbf{P} &= \mathbf{X} \mathbf{P}' \mathbf{X}^\dagger \end{aligned} \tag{3.1}$$

where the transform matrices are:

$$\begin{aligned} \mathbf{X} &= \mathbf{U}\mathbf{s}^{-1/2} \\ \mathbf{Y} &= \mathbf{X}\mathbf{s} = \mathbf{U}\mathbf{s}^{1/2}. \end{aligned} \tag{3.2}$$

with $\mathbf{U}$ and $\mathbf{s}$ denoting the eigenvector and diagonal eigenvalue matrix of the overlap matrix $\mathbf{S}$, respectively. In the case of linear dependencies in the overlap matrix (typically large basis sets with diffuse functions) the $\mathbf{X}$ and $\mathbf{Y}$ matrices become size $n \times m$, while the density and Fock matrices become size $m \times m$. Here, n and m represent the number of atomic and canonical orbitals, respectively, with $m \leq n$.

Finally, the molecular orbital (MO) basis, denoted with an "MO" subscript, is another orthogonal basis defined by projection onto the ground state eigenvectors, and is used to

deconvolute the time dependent dipole moment into contributions due to MO pairs for analysis purposes. All MO operators are size $m \times m$, where m is the number of canonical orbitals, i.e,. $m < n$ for the case of linear dependencies. The details of the projection onto the MO basis is discussed in Sec. 3.2.3.

3.2.2 Absorption Spectra from Broadband Excitation

To compute a wide spectrum of electronic excited states, typically a delta-function or step-function electric field is used. To illustrate how to properly correct for phase using an arbitrary electric field, we instead use a narrow Gaussian electric field of amplitude κ, width w, center t_0, and polarization $\hat{d} = \{\hat{x}, \hat{y}, \hat{z}\}$:

$$E(t) = \kappa \exp\left[-\frac{(t-t_0)^2}{2w^2}\right] \hat{d} \tag{3.3}$$

As in Chapter 1, this electric field is coupled into the Fock matrix through an external potential ($\mathbf{V}$) by its product with the transition dipole matrix ($\mathbf{D}$),

$$\mathbf{V}(t) = -\mathbf{D}\cdot\mathbf{E}(t) \tag{3.4}$$

which implicitly assumes a uniform electric field across the molecule. This can be extended to high frequency fields via quadrupole and higher terms, although even for deep core X-ray absorption these effects are often negligible[60]. The excitation spectrum is computed from the time-dependent expectation value of the dipole, which in the atomic orbital basis is:

$$\mu_d(t) = \mathrm{Tr}\left[\mathbf{M}(t)\right] = \mathrm{Tr}\left[\mathbf{D}_d\mathbf{P}(t)\right] \tag{3.5}$$

Since the total dipole is built from the trace elements of matrix M, these values will be important later for obtaining the peak compositions.

Performing a Fourier transform of the dipole and electric fields then yields the dipole polarizability:

$$\alpha_{dd} = \frac{\mu_d(\omega)E_d^*(\omega)}{E_d(\omega)E_d^*(\omega)} = \frac{\mu_d(\omega)E_d^*(\omega)}{|E_d(\omega)|^2} \tag{3.6}$$

where the multiplication and division by the complex conjugate of the transformed electric field compensates for any phase ripples in the spectrum due to a time-shifted excitation. Finally, the dipole strength function is computed from the polarizability:

$$S(\omega) = \frac{4\pi\omega}{3c}\mathrm{Im}\left[\alpha_{xx}(\omega) + \alpha_{yy}(\omega) + \alpha_{zz}(\omega)\right] \tag{3.7}$$

3.2.3 Molecular Orbital Dipole Contributions

Although $S(\omega)$ yields the absorption spectrum, including excitation energies and absorption/oscillator strengths, it is often useful to characterize excitations according to their dominant molecular orbital contributions, as is done in linear response (Casida method) TDDFT. For this, we compute the time-dependent transition dipole moments in the basis of the ground state molecular orbitals[2,3]. For small perturbations from the ground state (linear reponse regime) and for the times when there is no applied electric field (e.g., after the excitation pulse has passed), the time-dependent density matrix can be projected onto the ground state molecular orbitals yielding MO pair contribution time-dependent dipole moments $\bar{}_{ia}(t)$. This consists of first diagonalizing the ground state Fock matrix in the canonical basis and converting to the atomic orbital basis

$$\mathbf{F}'\mathbf{C}' = \mathbf{C}'\epsilon \tag{3.8}$$

$$\mathbf{C} = \mathbf{X}\mathbf{C}' \tag{3.9}$$

where $\mathbf{C}$ is the eigenvector matrix and ϵ is the diagonal matrix of eigenvalues.

The density matrix and transition dipole matrix in the AO basis can then be transformed to the basis of the ground state molecular orbitals:

$$\mathbf{P}^{\mathrm{MO}} = (\mathbf{C}^{-1})\mathbf{P}(\mathbf{C}^{-1})^{\dagger} \tag{3.10}$$

$$\mathbf{D}^{\mathrm{MO}} = \mathbf{C}^{\dagger}\mathbf{D}\mathbf{C}. \tag{3.11}$$

For large systems with diffuse basis functions, linear dependencies in the overlap matrix require pruning away orthogonal orbitals using canonical orthogonalization. In such instances, the dimensions of $\mathbf{C}$ are reduced to $n \times m$, where n and m represent the number of atomic and canonical orbitals, respectively, with $m < n$. Using such truncated non-square matrices requires left and right pseudo-inverses

$$\mathbf{C}_L^{-1} = (\mathbf{C}^{\dagger}\mathbf{C})^{-1}\mathbf{C}^{\dagger} \tag{3.12}$$

$$(\mathbf{C}_R^{-1})^{\dagger} = \mathbf{C}(\mathbf{C}^{\dagger}\mathbf{C})^{-1} \tag{3.13}$$

with the resulting density matrix in the MO basis becoming size $m \times m$

$$\mathbf{P}^{\mathrm{MO}} = \mathbf{C}_L^{-1}\mathbf{P}(\mathbf{C}_R^{-1})^{\dagger} \tag{3.14}$$

To study electronic transitions and induced dipole moments we first construct a MO dipole matrix as a linear combination of all possible MO pairs. For clarity we will show this for a particular polarization and drop the d subscript.

$$\mathbf{M}_{ij}(t) = \sum_{k=1}^{m} \mathbf{D}_{ik}\mathbf{P}_{kj}(t) \tag{3.15}$$

$$= \mathbf{D}_{i1}\mathbf{P}_{1j}(t) + \mathbf{D}_{i2}\mathbf{P}_{2j}(t) + \mathbf{D}_{i3}\mathbf{P}_{3j}(t) + \ldots \tag{3.16}$$

The total dipole can be computed from the trace of $\mathbf{M}(t)$ (eq 3.5)

$$\mu(t) = \sum_{i=1}^{m} \mathbf{M}_{ii}(t) \tag{3.17}$$

Now, looking at elements of this trace

$$\mathbf{M}_{11} = \mathbf{D}_{11}\mathbf{P}_{11} + \mathbf{D}_{12}\mathbf{P}_{21} + \mathbf{D}_{13}\mathbf{D}_{31} + \ldots \tag{3.18}$$

$$\mathbf{M}_{22} = \mathbf{D}_{21}\mathbf{P}_{12} + \mathbf{D}_{22}\mathbf{P}_{22} + \mathbf{D}_{23}\mathbf{D}_{32} + \ldots \tag{3.19}$$

we note that the terms in $\mathbf{M}_{ii}$ arising from occupied-occupied MO pairs (e.g., $\mathbf{D}_{11}\mathbf{P}_{11}$) sum up to the static dipole of the system μ_0, whereas the time-dependence is contained in the occupied-virtual terms (e.g., $\mathbf{D}_{12}\mathbf{P}_{21}$). The time-dependent MO pair dipole for occupied state i and virtual state a is then given by:

$$\mu_{ia}(t) = \mathbf{D}_{ia}^{\mathrm{MO}}\mathbf{P}_{ai}^{\mathrm{MO}}(t) + \mathbf{D}_{ai}^{\mathrm{MO}}\mathbf{P}_{ia}^{\mathrm{MO}}(t) \tag{3.20}$$

with the total dipole given by

$$\mu(t) = \mu_0 + \sum_{i=1}^{m_{\mathrm{occ}}} \sum_{a=m_{\mathrm{occ}}+1}^{m} \mu_{ia}(t) \tag{3.21}$$

where m_{occ} is the number of occupied orbitals. Physically, the MO pair dipoles $\mu_{ia}(t)$ can be viewed as the deconvolutions of the total dipole into contribution excitations from occupied to virtual orbitals. Practically, the Fourier transforms of these dipoles yield the MO contributions of every excitation in the system, i.e., for an excitation of interest in the system, the $\mu_{ia}(\omega)$ peaks in that energy range provide the percent MO contributions. In other words, these quantities yield information qualitatively similar to the coefficients from a linear-response TDDFT calculation. Although the LR and RT coefficients are qualitatively

similar and yield equivalent physical interpretations, they are measures of different quantities and cannot be quantitatively compared. The LR percents, on one hand, are obtained from the eigenvectors (coefficients) of the linear response matrix, whereas the RT percentages are related to the relative dipole contributions to a peak of interest.

3.2.4 Padé Accelerated Transforms

One critical limitation of a real-time approach over frequency-domain (root-based) methods is the long simulation times required to converge a spectrum. Moreover, for large system sizes with a high density of states, the congested spectra require even longer simulations to resolve nearby peaks due to the Fourier uncertainty principle. We use Padé approximants to decrease the simulation times by accelerating the convergence of the Fourier transform of the time-dependent transition dipole moments.

This consists of fitting the transform from a short-time simulation to a ratio of power series expansions. The denominator in the ratio provides added flexibility in the coefficients, especially for capturing poles in the signal. Once these expansion coefficients are known, one can interpolate the spectrum to arbitrary spectral density, which is equivalent to extrapolating the signal in time. Padé approximants do not require any assumption about the functional form of the time or frequency signal, unlike stencil or Filter diagonalization approaches. Thus, Padé methods are likely to be useful for acceleration coupled electron/nuclear simulations for first-principles non-Lorentzian linewidths, for example. On the other hand, Padé approximants can produce artifacts or false peaks in spectra, especially for short time signals. In practice, however, these artifacts are highly sensitive to signals length, and simple convergence checks with simulation time ensure spectra contain only physical peaks.

To calculate frequency spectra by use of Padé approximants, the Fourier transform of a MO dipole pair is expressed in its discrete form by:

$$\mu_{ia}(\omega) = \sum_{k=0}^{M} \mu_{ia}(t_k) e^{-i\omega t_k} \tag{3.22}$$

where the $\mu_{ia}(t_k)$ are discrete time signal values. Here, the M denotes the total number of points, and t_k are the time values. For a constant time step $t_k = k\Delta t$, the exponential can be rewritten as

$$\mu_{ia}(\omega) = \sum_{k=0}^{M} \mu_{ia}(t_k) e^{-i\omega k\Delta t} \tag{3.23}$$

$$= \sum_{k=0}^{M} \mu_{ia}(t_k) \left(e^{-i\omega\Delta t}\right)^k \tag{3.24}$$

This is now in the form of a power series expansion where, if $c_k \equiv \mu_{ia}(t_k)$ and $z_k \equiv e^{-i\omega\Delta t}$,

$$\mu_{ia}(z) = \sum_{k=0}^{M} c_k (z_k)^k \tag{3.25}$$

As mentioned previously, the method of Padé approximants equates an initial power series to a ratio of power series expansions:

$$\mu_{ia}(z) = \frac{\sum_{k=0}^{N} a_k z^k}{\sum_{k=0}^{N} b_k z^k} \tag{3.26}$$

Note that $z = f(\omega)$, and we have adopted a diagonal Padé scheme such that $N = M/2$. The resulting linear system is then

$$\sum_{k=0}^{M} c_k z^k \cdot \sum_{m=0}^{N} b_m z^m = \sum_{k=0}^{N} a_k z^k \tag{3.27}$$

This describes a system that has $2N+1$ equations for $2N$ unknowns ($a_0, a_1, ..., a_N$ and $b_0, b_1, ...b_N$). Thus, it is customary to prescribe $b_0 = 1$ for the free variable of the over-determined system of equations. The relationship between the coefficients can be determined by expanding eq. 3.27 and equating powers of z. The equations involving z^0 to z^N give:

$$\sum_{m=0}^{k} b_m c_{k-m} = a_k, \quad k = 1, \ldots N \tag{3.28}$$

with $a_0 = c_0$. The z^{N+1} to z^M terms give:

$$\sum_{m=1}^{N} b_m c_{N-m+k} = -c_{N+K}, \quad k = 1, \ldots, N \tag{3.29}$$

Eq. 3.29 relates the b coefficients to the known c's and is most conveniently solved in a matrix form:

$$\mathbf{G}b = d \tag{3.30}$$

where $\mathbf{G}$ is a $N \times N$ matrix with elements $G_{km} = c_{N-m+k}$, $\mathbf{d}$ is a length N column vector with elements $d_k = -c_{N+k}$, and $\mathbf{b}$ is a length N vector (recall $b_0 = 1$ by convention). The unknown b's are found via inversion:

$$b = \mathbf{G}^{-1} d \tag{3.31}$$

Once the b values are known, the a_k coeffients are calculated by

$$a_k = \sum_{m=0}^{k} b_m c_{k-m}, \quad k = 1, \ldots N \tag{3.32}$$

With the a and b coefficients known, the Fourier transform can be constructed using eq 3.26. As these coefficients are not functions of the frequency, the spectrum can be calculated for an

arbitrary density of frequencies. This is akin to extrapolation of the time signal to arbitrarily long times.

3.3 Results

In this section we compute the core and valence spectra for water and a Ni-porphyrin using this RT-TDDFT approach to demonstrate three advantages over a conventional real-time simulation: (i) accelerated convergence of the spectra, (ii) attribution of peak to molecular orbital transitions, and (iii) extraction of selected transitions (e.g., from a particular X-ray absorption edge) from congested spectra.

3.3.1 Valence and Core-Level Spectra of Water

First, we present results for the valence and X-ray absorption of a single gas-phase water molecule. The geometry was optimized using aug-cc-pVTZ/B3LYP, while the excited state calculations (both valence and core) used the Sapporo-QVP[61] with diffuse functions on the oxygen and hydrogen atoms. As we are primarily interested in demonstrating this approach, we use the B3LYP functional[62] throughout, although other functionals are likely more suitable for XANES[36,63].

First, we computed the oxygen K-edge core-level spectra for water. A Gaussian pulse electric field was used with a center at $t_0 = 20\text{au} = 0.48\text{fs}$, a field strength of $\kappa = 0.001\text{au}$, and pulse width $w = 0.024\text{fs}$. The time step was $\Delta t = 0.05\text{au} = 1.2\text{as}$ and the signal was damped with $\tau = 150\,\text{au} = 3.6\,\text{fs}$ prior to transformation to give well-defined Lorentzian lineshapes, which result from exponential damping of the time signal, i.e., the Fourier transform of a decaying exponential is a Lorentzian with full-width half maximum inversely proportional to the exponential lifetime. See Table S1 in Appendix A for a complete list of all simulation parameters. The resulting XANES spectra were computed using the Padé approximant method and checked for convergence with simulation time (see below for valence example). Additionally, these spectra were shifted by $\Delta = +15.4\,\text{eV}$ to be consistent with previous

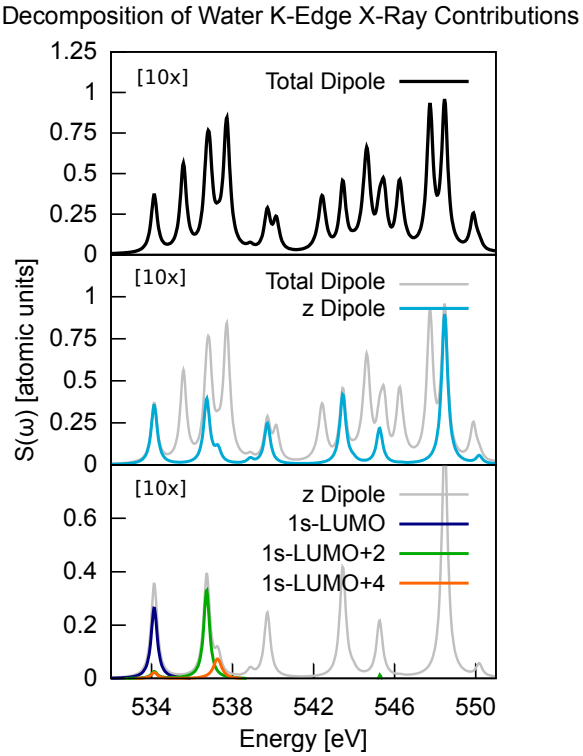

Figure 3.1: Top-down decomposition of the total oxygen K-edge absorption spectrum of water (top) by light polarization (middle) followed by occupied→ virtual molecular orbital transition dipole pairs (bottom). The total dipole can be reconstructed from the sum of all transition dipole spectra for each polarization.

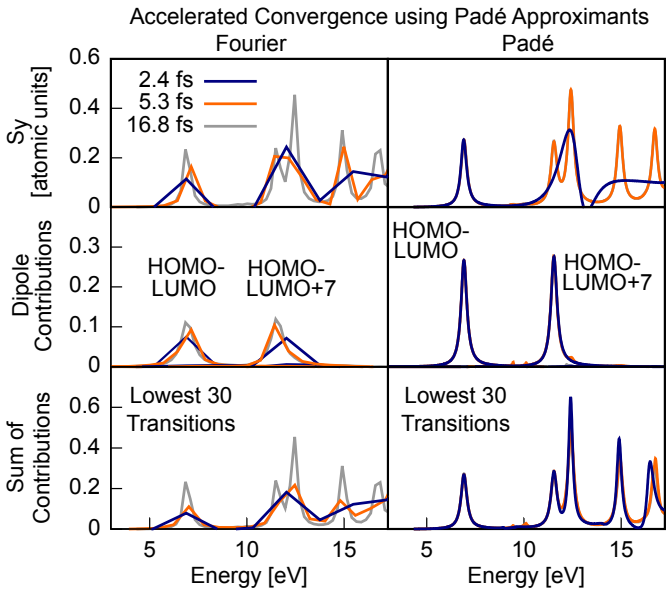

Figure 3.2: Time convergence of the total y-polarized valence spectrum for water using conventional Fourier transforms (left column) and Padé acceleration (right column). Using Padé, the transform of the total z dipole (top row) converges with a simulation time approximately three times shorter than FT. Two representative individual MO contributions $\mu_{1\to6}(\omega)$ and $\mu_{1\to13}(\omega)$ are shown in the middle row. The resulting spectrum computed from the sum of all dipole pairs (bottom) converges with a simulation time approximately seven shorter than FT.

calculations and experimental work[36,64]. This shift issue could be remedied by DFT methods with improved description of core-hole relaxation, such as orthogonality constrained DFT[65].

The first step is to compute and transform the time-dependent MO dipole contributions $\mu_{ia}(t)$. The time signals for the total dipole $\mu(t)$ and two representative dipole contributions $\mu_{ia}(t)$ are shown in Fig. S1 in the appendix Using a top-down approach, the total dipole $^{-}(t)$ can separated into its three polarization components $\mu_d(t)$, $d = \{x, y, z\}$, each of which can then be deconstructed into the various MO contributions $\mu_{ia,d}(t)$ (Eq. 3.20). The sum of all the $\mu_{ia,d}(t)$ yields the total dipole, although only occupied-virtual combinations contribute to the time-dependence. Fig. 3.1 shows the resulting breakdown for the water oxygen K-edge XANES. The congested spectrum from the total dipole (top) becomes simpler when separated into polarizations (middle: z) and further deconstructed into MO pair dipole

components (bottom). This spectral isolation becomes advantageous when accelerating via Padé.

To explore this acceleration, we computed the valence absorption spectrum using three methods: conventional Fourier transform of the total dipole in each polarization, Padé accelerated spectra from the polarization-dependent dipoles, and finally spectra built from sum of Padé accelerated transforms of occupied-virtual $\mu_{ia,d}(t)$ contributions (Eq. 3.21). All propagation and signal processing parameters were the same as the XANES calculations except for a larger time step of $\Delta t = 0.2$ au $= 4.8$ as. In Fig. 3.2, the left column shows the spectra processed by Fourier methods, and the right column shows those processed with Padé Approximants. The top row of the figure is the total dipole calculated using three different lengths of simulation time, and it can be noted that the Padé of the total dipole converges three times faster than that of the Fourier transform, i.e. a Fourier approach requires $t_{\max} \gtrsim 15$ fs, whereas the Padé of the total requires only $t_{\max} \gtrsim 5$ fs. In the second row, the Padé transforms of two dipole contributions μ_{ia} are converged even at 2.4 fs because they contain fewer frequencies than the total, thereby resolving more quickly. By adding all of the transformed μ_{ia} contributions together, the total dipole can be reconstructed (bottom row). This rebuilt spectrum from the sum of the Padé transforms of the $\mu_{ia,d}(t)$ is effectively converged at $t_{\max} \gtrsim 2.5$ fs, which is approximately seven times faster than a Fourier transform. In other words, calculating the dipole contributions finding their Padé transforms individually provides an additional acceleration advantage over Padé transformation of the total.

Next we compute the MO contributions to the peaks, yielding physical interpretation of the excitations. Transition "coefficients" are determined from the percent dipole strength of each MO pair, i.e., the area under a single MO contribution $S^{\text{int}}_{ia,d}(\omega)$ divided by the area of the total dipole signal. As the MO contribution spectra are sparse, it is unlikely to have two transitions at similar energies for a particular MO pair; thus, in practice, the

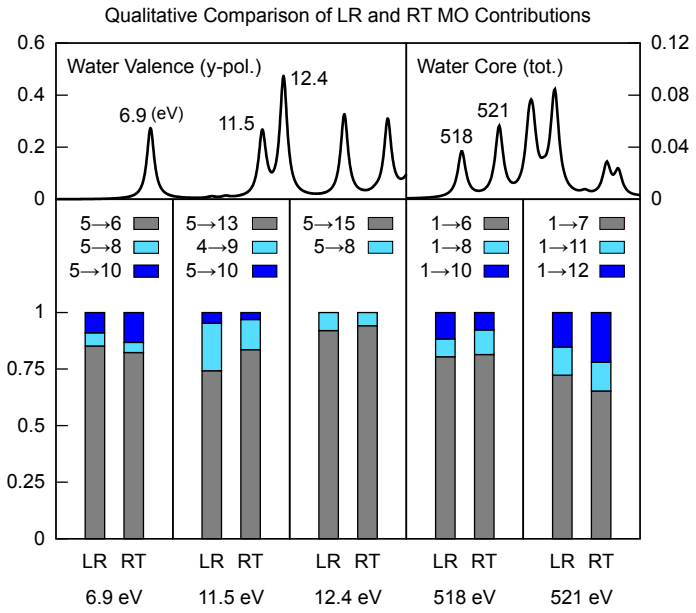

Figure 3.3: Coefficient values from linear-response (LR) and real-time (RT) calculations are compared for select valence and core excitations in water. The height of each bar corresponds to the percent contribution of each specific molecular orbital involved in that transition. Overall, the LR and RT coefficients demonstrate good qualitative agreement.

integration is taken across a frequency range containing only the excitation of interest. In the unlikely situation that two peaks are nearby, fitting the $S_{ia,d}(\omega)$ spectra to Lortentzians would be useful for obtaining the $p^{\mathrm{RT}}_{ia,d}$ values, at least for the case of exponentially damped time signals. Note, that at a given frequency the $S_{ia,d}(\omega)$ peaks may be either positive or negative, which arises from a relative phase between the oscillations of the $\mu_{ia}(t)$, each of which can be viewed as a coherence between two states. The total dipole constructed from the sum of these contributions, however, is guaranteed to be positive, at least for the case of absorption from the ground state. Excited state absorption or stimulated emission, on the other hand, may have negative dipole spectral features.[39]

For comparison with LR, the RT coefficients are defined as the square root of these areas:

$$p^{\mathrm{RT}}_{ia,d} = \frac{\left|S^{\mathrm{int}}_{ia,d}\right|^{\frac{1}{2}}}{\sum_{i,a}\left|S_{ia,d}\right|^{\frac{1}{2}}}, \tag{3.33}$$

$$S_{ia,d}^{\text{int}} \equiv \int_{\omega_-}^{\omega_+} d\omega \; S_{ia,d}(\omega) \tag{3.34}$$

which corresponds to a percent. In linear-response TDDFT the MO coefficients are square normalized, which tends to over-emphasize large contributions. Here, we instead consider the absolute values of the occupied-virtual coefficients normalized by the sum of their absolute values:

$$p_{ia,d}^{\text{LR}} = \frac{|c_{ia,d}|}{\sum_{i,a} |c_{ia,d}|} \tag{3.35}$$

Figure 3.3 shows the resulting comparison between the LR and RT contributions for the valence and oxygen K-edge XANES spectra for water. For example, in both the LR and RT analysis, the first valence peak (6.9 eV) largely consists of HOMO→LUMO with a small contribution from HOMO→LUMO+2 and LUMO+4. The second XANES peak (521 eV) is largely oxygen 1s → LUMO+1, and smaller contributions from transitions to the LUMO+5 and LUMO+6. Overall, the MO deconvolution method demonstrates good qualitative agreement with linear response.

3.3.2 Near-Edge X-ray Absorption in a Ni-Porphyrin

Although water provides an illustrative picture of near-edge XAS features, it is a simple molecule, and its transitions remain similar to atomic core exitations and its XAS spectrum is very sparse. As a means to further validate the real-time contribution and acceleration techniques for larger molecules, here we compute the nitrogen K-edge spectra in Ni porphyrin ($C_{20}H_{12}N_4Ni$). The geometry was optimized in the gas phase using B3LYP and the 6-31++G** basis for C, N, and H, and the Stuttgart-RSC-1997 ECP for the Ni atom. The excited state calculations were performed using B3LYP, and a mixed basis of 6-31+G* for C and H, Stuttgart-RSC-1997 ECP for the Ni, and the Sapporo-TZP basis[61] with added

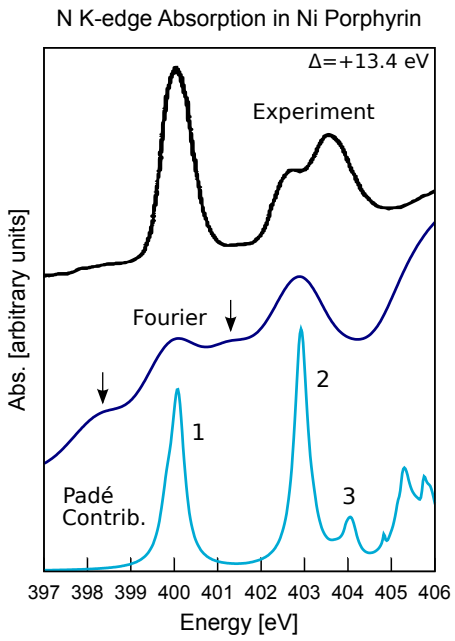

Figure 3.4: Experimental nitrogen K-edge XANES (top) and RT-TDDFT computed spectra using Fourier transform (FT) of the dipole (middle) and Padé accelerated MO pair contributions (bottom). The FT is too broad to resolve all features and contains non-physical intruder peaks (arrows). The Padé contribution method, on the other hand, is sufficiently resolved and includes only physical excitations. The experimental spectrum was digitized with permission from Ref. 66 (Copyright 1993 American Chemical Society).

diffuse functions for the four N atoms. Additionally, the N 1s functions were uncontracted to provide more variational flexibility, resulting in a total of 561 basis functions.

To demonstrate the acceleration advantages of the deconvolution/Padé approach versus Fourier transforms (FT), all spectra were computed using a total propagation time of 5 fs. The simulation parameters were the same as for the water XANES case. Before taking the FT, the time signals were damped with $\tau = 30$ au $= 0.73$ fs and padded with 10^6 zeros to increase spectral density. If a signal is not damped to zero before padding, however, the resulting discontinuity in the signal gives rise to ripples in the spectrum (Gibbs artifacts). Practically, damping the signal to a few percent is typically sufficient. To facilitate visualization and integration without losing resolution, the Padé the signals were damped with $\tau = 150$ au $= 3.6$ fs. The RT-TDDFT spectra have been shifted to match the first peak of

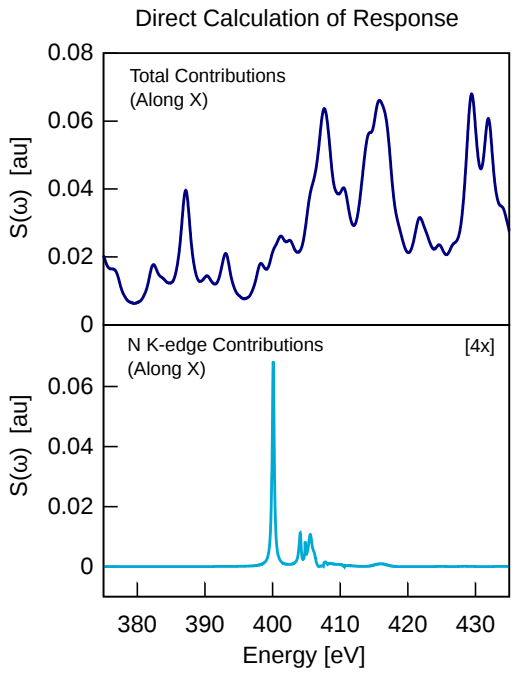

Figure 3.5: The nitrogen x-polarized K-edge XANES spectrum of nickel porphyrin computed from the Fourier transform (top) exhibits numerous non-physical intruder peaks due to transitions from other core edges or the valence to high virtual states. In contrast, the spectrum constructed from the nitrogen 1s MO dipole pairs (bottom) shows only physical excitations for the N K-edge.

the experimental results (Δ =+13.4 eV). Each RT-TDDFT simulation used 56 processors for 14 hours.

Figure 3.4 shows a comparison between the computed and experimental[66] XANES. Here, the experimental molecule is nickel octaethylporphyrin, which is the ethyl functionalized analog of nickel porphyrin, whereas the simulations were performed on unfunctionalied nickel porphyrin. The effect of these functional groups on the lowest energy peaks in the spectrum is likely limited due to character of the virtual states, which are π^* dominated. The traditional Fourier transform (middle) of the total dipole signal captures the gross features of the experimental XANES absorption spectrum (top), but the poor resolution makes resolving nearby spectral features impossible. The Padé results (bottom), on the other hand, are well-resolved and agree reasonably well with the experimental spectrum.

Table 3.1: The MO pair contributions for the nitrogen K-edge XANES in nickel porphyrin. For clarity, only the dominant polarization is labeled, and only the contributions greater than 10% are shown. Here "percent" refers to p_{ia} in eq 3.34.

Peak	**Energy (eV)**	**Pol.**	**Transition**	**Percent**	**Target MO**	**Character**
1a	400	z	1→90	19.5	π^* C_i (E_g)	Macrocycle C p_z y-axis
			1→95	29.1	π^* C_{4v} (A_{2u})	(C_α-N-C_α)-Ni p_z
			1→99	19.6	σ^* D_{4h} (A_{1g})	N $p_{x,y}$ & Ni dz^2
			1→115	12.8	σ^* D_{2h} (B_{1g})	C_β $p_{x,y}$ & H s
			1→116	12.4	π^* C'_{2h} (E_g)	[N-C_α-C_β]$_2$-C_{meso} p_z
1b	400	xy	1→91	75.8	π^* C_i (E_g)	Macrocycle C p_z x-axis
2	403	z	1→95	36.7	π^* C_{4v} (A_{2u})	(C_α-N-C_α)-Ni p_z
			1→99	19.5	σ^* D_{4h} (A_{1g})	N $p_{x,y}$ & Ni dz^2
			1→115	11.1	σ^* D_{2h} (B_{1g})	C_β $p_{x,y}$ & H s
			1→116	10.2	π^* C_{2h} (B_g)	[N-C_α-C_β]$_2$-C_{meso} p_z
3	404	z	1→95	14.8	π^* C_4 (A_{2u})	(C_α-N-C_α)-Ni p_z
			1→99	33.3	σ^* D_{4h} (A_{1g})	N $p_{x,y}$ & Ni dz^2
			1→115	12.2	σ^* D_{2h} (B_{1g})	C_β $p_{x,y}$ & H s
			1→116	10.9	π^* C'_{2h} (E_g)	[N-C_α-C_β]$_2$-C_{meso} p_z

Note also that the FT spectrum contains additional non-physical peaks labeled with arrows. These "intruder" peaks arise from transitions from valence or high edge core orbitals to very high virtual states, which are poorly described by both the atom centered basis and the DFT functional. These transitions are non-physical because they occur at energies well above the ionization edge of a given valence MO. The continuum spectrum should thus smoothly falloff and be relatively featureless, save for shape resonances, for example. Gaussian type basis sets cannot adequately capture this, instead giving a series of discrete non-physical peaks. One solution is to introduce phenomenological lifetimes to the high energy virtual molecular orbitals to "filter out" these non-physical transitions. Coupled with range-separated TDDFT, this has shown to adequately capture both resonance and near-edge X-ray spectra.[35,63] LR-TDDFT avoids this problem by orbital windowing, i.e., selecting transitions only from the core state of interest. In principle, however, if all of the transitions were calculated, analogous intruders would be present. If the transition frequen-

cies are similar to the XANES edge of interest, these non-physical peaks can contaminate the spectrum. One solution is to introduce phenomenological lifetimes to the high energy virtual states[63]. Using our approach here, this issue of intruder peaks can instead be remedied by reconstructing the spectrum from individual dipole contributions $S_{ia,d}(\omega)$. Figure. 3.5 shows a comparison between the x-polarized FT and the corresponding spectrum computed using transitions from the four nitrogen "1s" molecular orbitals to the 30 lowest virtual orbitals. The FT spectrum is essentially incomprehensible whereas the dipole pair spectrum contains only nitrogen K-edge features. LR-TDDFT methods, on the other hand, which are typically based on energy windowing, do not suffer this problem, although Davidson convergence can be problematic for XANES in large molecules.

Next, we analyze the MO contributions for the XANES peaks. Previous experimental studies assert that nitrogens in phorphyrins and imidizoles possess transitions to π^* resonances at energies near 400, 403, and 404 eV for the K-edge[66,67]. In our case, the nickel porphyrin contains four equivalent nitrogen atoms which exhibit K-edge features consistent with these energies. Table 3.1 shows the dominant ($p_{ia,d} > 0.1$) MO pair contributions for the three lowest XANES peaks. The lowest broad peak consists of two nearby transitions, denoted 1a and 1b. Qualitatively, peak 1a is largely z-polarized and involves a mixture of N 1s$\rightarrow$ π^* and σ^* orbitals with significant contributions from the (C_α-N-C_α)-Ni π^*, the N 2p + Ni dz^2 σ^*, and a π^* macrocyclic resonance contributor along the y-axis. A degenerate π^* resonance contributor along the x-axis is the largest contribution of peak 1b.

The next peak near 403 eV has its largest contribution from the (C_α-N-C_α)-Ni π^* and a smaller contribution from the N 2p + Ni dz^2 σ^*. Other notable contributions are π^* interactions farther from the metal center between nitrogen, α-carbons, and the flanking β- and meso-carbons (the bridging methylene carbons). Additionally, another σ^* is involved from β carbons and hydrogens. The third peak near 404 eV has its largest contributions from a N 2p + Ni dz^2 σ^* with other significant contributions from (C_α-N-C_α)-Ni π^*. This

peak also contains the same notable transitions observed in the second peak, yet there are higher contributions from σ^* and π^* interactions farther from the metal center and nitrogens. Overall, the observed trend towards increasing σ^* character for higher photon energies is consistent with the traditional interpretation of XANES in porphyrin systems.

3.4 Conclusions

In this article, we have presented a method for accelerating the computation of absorption spectra using real-time TDDFT. The total time-dependent dipoles were deconstructed into MO pair contributions, which provides insight into the dominant molecular orbitals involved in each excitation. Additionally, Padé approximants were used to accelerate the transforms of these individual contributions, where the sum of transformed component spectra yields the converged total dipole signal with dramatically reduced simulation time. This effect is even more apparent for systems with many transitions and higher spectral density. Finally, by considering only select MO pairs, the resulting spectra are not contaminated with spurious intruder peaks due to transitions to very high virtual states. This enables simple real-time simulations for X-ray absorption, for example, without resorting to phenomenological damping or filtering.

We demonstrated the validity of this technique by computing the valence and core (oxygen K edge) spectra of gas-phase water and nitrogen K edge XANES for a Ni-porphyrin. The resulting spectra and their analyzed MO transitions were found to be consistent with linear response (frequency-domain) TDDFT. Moreover, Padé accelerated transforms of the individual contributions resulted in rapid convergence of the spectra, essentially allowing for simulation times at least five times shorter than using traditional Fourier transforms. The combined MO decomposition/Padé scheme is especially promising for computing excited states in large molecules and materials, where the high density of states and large basis sets would otherwise require long simulations to adequately resolve the spectra.

3.5 References

[1] A. Bruner, D. LaMaster, and K. Lopata, "Accelerated broadband spectra using transition dipole decomposition and padé approximants," *J. Chem. Theory Comput.*, vol. 12, no. 8, pp. 3741–3750, 2016.

[2] M. Repisky, L. Konecny, M. Kadek, S. Komorovsky, O. L. Malkin, V. G. Malkin, and K. Ruud, "Excitation energies from real-time propagation of the four-component dirac–kohn–sham equation," *J. Chem. Theory Comput.*, vol. 11, no. 3, pp. 980–991, 2015.

[3] M. Kadek, L. Konecny, B. Gao, M. Repisky, and K. Ruud, "X-ray absorption resonances near $l_{2,3}$-edges from real-time propagation of the dirac–kohn–sham density matrix," *Phys. Chem. Chem. Phys*, vol. 17, no. 35, pp. 22566–22570, 2015.

[4] L. A. Bartell, M. R. Wall, and D. Neuhauser, "A time-dependent semiempirical approach to determining excited states," *J. Chem. Phys.*, vol. 132, no. 23, p. 234106, 2010.

[5] K. Lopata, R. Reslan, M. Kowalska, D. Neuhauser, N. Govind, and K. Kowalski, "Excited-state studies of polyacenes: a comparative picture using eomccsd, cr-eomccsd (t), range-separated (lr/rt)-tddft, td-pm3, and td-zindo," *J. Chem. Theory Comput.*, vol. 7, no. 11, pp. 3686–3693, 2011.

[6] K. C. Kulander, "Time-dependent hartree-fock theory of multiphoton ionization: Helium," *Phys. Rev. A*, vol. 36, pp. 2726–2738, Sep 1987.

[7] X. Li, S. M. Smith, A. N. Markevitch, D. A. Romanov, R. J. Levis, and H. B. Schlegel, "A time-dependent hartree–fock approach for studying the electronic optical response of molecules in intense fields," *Phys. Chem. Chem. Phys.*, vol. 7, no. 2, pp. 233–239, 2005.

[8] C. M. Isborn and X. Li, "Singlet-triplet transitions in real-time time-dependent hartree-fock/density functional theory," *J. Chem. Theory Comput.*, vol. 5, no. 9, pp. 2415–2419, 2009.

[9] J. Theilhaber, "Ab initio simulations of sodium using time-dependent density-functional theory," *Phys. Rev. B*, vol. 46, pp. 12990–13003, Nov 1992.

[10] K. Yabana and G. F. Bertsch, "Time-dependent local-density approximation in real time," *Phys. Rev. B*, vol. 54, pp. 4484–4487, Aug 1996.

[11] X. Andrade, D. Strubbe, U. De Giovannini, A. H. Larsen, M. J. T. Oliveira, J. Alberdi-Rodriguez, A. Varas, I. Theophilou, N. Helbig, M. J. Verstraete, L. Stella, F. Nogueira, A. Aspuru-Guzik, A. Castro, M. A. L. Marques, and A. Rubio, "Real-space grids and the octopus code as tools for the development of new simulation approaches for electronic systems," *Phys. Chem. Chem. Phys.*, vol. 17, pp. 31371–31396, 2015.

[12] R. Baer and D. Neuhauser, "Real-time linear response for time-dependent density-functional theory," *J. Chem. Phys.*, vol. 121, no. 20, pp. 9803–9807, 2004.

[13] C.-L. Cheng, J. S. Evans, and T. Van Voorhis, "Simulating molecular conductance using real-time density functional theory," *Phys. Rev. B*, vol. 74, no. 15, p. 155112, 2006.

[14] J. Sun, J. Song, Y. Zhao, and W.-Z. Liang, "Real-time propagation of the reduced one-electron density matrix in atom-centered gaussian orbitals: Application to absorption spectra of silicon clusters," *J. Chem. Phys.*, vol. 127, no. 23, p. 234107, 2007.

[15] S. Meng and E. Kaxiras, "Real-time, local basis-set implementation of time-dependent density functional theory for excited state dynamics simulations," *J. Chem. Phys.*, vol. 129, no. 5, p. 054110, 2008.

[16] H. O. Wijewardane and C. A. Ullrich, "Real-time electron dynamics with exact-exchange time-dependent density-functional theory," *Phys. Rev. Lett.*, vol. 100, no. 5, p. 056404, 2008.

[17] K. Lopata and N. Govind, "Modeling fast electron dynamics with real-time time-dependent density functional theory: Application to small molecules and chromophores," *J. Chem. Theory Comput.*, vol. 7, no. 5, pp. 1344–1355, 2011.

[18] M. R. Provorse and C. M. Isborn, "Electron dynamics with real-time time-dependent density functional theory," *Int. J. of Quant. Chem.*, vol. 116, no. 10, pp. 739–749, 2016.

[19] P. Krause, T. Klamroth, and P. Saalfrank, "Time-dependent configuration-interaction calculations of laser-pulse-driven many-electron dynamics: Controlled dipole switching in lithium cyanide," *J. Chem. Phys.*, vol. 123, no. 7, p. 074105, 2005.

[20] A. E. DePrince, M. Pelton, J. R. Guest, and S. K. Gray, "Emergence of excited-state plasmon modes in linear hydrogen chains from time-dependent quantum mechanical methods," *Phys. Rev. Lett.*, vol. 107, p. 196806, Nov 2011.

[21] P. Krause, J. A. Sonk, and H. B. Schlegel, "Strong field ionization rates simulated with time-dependent configuration interaction and an absorbing potential," *J. Chem. Phys.*, vol. 140, no. 17, p. 174113, 2014.

[22] H.-D. Meyer, U. Manthe, and L. S. Cederbaum, "The multi-configurational time-dependent hartree approach," *Chem. Phys. Lett.*, vol. 165, no. 1, pp. 73–78, 1990.

[23] M. Nest, T. Klamroth, and P. Saalfrank, "The multiconfiguration time-dependent hartree–fock method for quantum chemical calculations," *J. Chem. Phys.*, vol. 122, no. 12, p. 124102, 2005.

[24] T. Sato and K. L. Ishikawa, "Time-dependent complete-active-space self-consistent-field method for multielectron dynamics in intense laser fields," *Phys. Rev. A*, vol. 88, no. 2, p. 023402, 2013.

[25] C. Huber and T. Klamroth, "Explicitly time-dependent coupled cluster singles doubles calculations of laser-driven many-electron dynamics," *J. Chem. Phys.*, vol. 134, no. 5, p. 054113, 2011.

[26] S. Kvaal, "Ab initio quantum dynamics using coupled-cluster," *J. Chem. Phys.*, vol. 136, no. 19, p. 194109, 2012.

[27] D. B. Jeffcoat and A. E. DePrince III, "N-representability-driven reconstruction of the two-electron reduced-density matrix for a real-time time-dependent electronic structure method," *J. Chem. Phys.*, vol. 141, no. 21, p. 214104, 2014.

[28] E. Runge and E. K. U. Gross, "Density-functional theory for time-dependent systems," *Phys. Rev. Lett.*, vol. 52, pp. 997–1000, Mar 1984.

[29] M. Petersilka, U. Gossmann, and E. Gross, "Excitation energies from time-dependent density-functional theory," *Phys. Rev. Lett.*, vol. 76, no. 8, p. 1212, 1996.

[30] A. Dreuw, J. L. Weisman, and M. Head-Gordon, "Long-range charge-transfer excited states in time-dependent density functional theory require non-local exchange," *J. Chem. Phys.*, vol. 119, no. 6, pp. 2943–2946, 2003.

[31] T. Stein, L. Kronik, and R. Baer, "Reliable prediction of charge transfer excitations in molecular complexes using time-dependent density functional theory," *J. Am. Chem. Soc.*, vol. 131, no. 8, pp. 2818–2820, 2009.

[32] C. M. Isborn and X. Li, "Modeling the doubly excited state with time-dependent hartree–fock and density functional theories," *J. Chem. Phys.*, vol. 129, no. 20, p. 204107, 2008.

[33] X.-M. Tong and S.-I. Chu, "Time-dependent density-functional theory for strong-field multiphoton processes: Application to the study of the role of dynamical electron correlation in multiple high-order harmonic generation," *Phys. Rev. A*, vol. 57, no. 1, p. 452, 1998.

[34] M. Lein and S. Kümmel, "Exact time-dependent exchange-correlation potentials for strong-field electron dynamics," *Phys. Rev. Lett.*, vol. 94, no. 14, p. 143003, 2005.

[35] K. Lopata and N. Govind, "Near and above ionization electronic excitations with non-hermitian real-time time-dependent density functional theory," *J. Chem. Theory Comput.*, vol. 9, no. 11, pp. 4939–4946, 2013.

[36] K. Lopata, B. E. Van Kuiken, M. Khalil, and N. Govind, "Linear-response and real-time time-dependent density functional theory studies of core-level near-edge x-ray absorption," *J. Chem. Theory Comput.*, vol. 8, no. 9, pp. 3284–3292, 2012.

[37] P. J. Lestrange, P. D. Nguyen, and X. Li, "Calibration of energy-specific tddft for modeling k-edge xas spectra of light elements," *J. Chem. Theory Comput.*, vol. 11, no. 7, pp. 2994–2999, 2015.

[38] F. Ding, B. E. Van Kuiken, B. E. Eichinger, and X. Li, "An efficient method for calculating dynamical hyperpolarizabilities using real-time time-dependent density functional theory," *J. Chem. Phys.*, vol. 138, no. 6, p. 064104, 2013.

[39] S. A. Fischer, C. J. Cramer, and N. Govind, "Excited state absorption from real-time time-dependent density functional theory," *J. Chem. Theory Comput.*, vol. 11, no. 9, pp. 4294–4303, 2015.

[40] M. E. Casida, *Time-Dependent Density Functional Response Theory for Molecules*, ch. 5, pp. 155–192. Wiley Online Library, 1995.

[41] R. E. Stratmann, G. E. Scuseria, and M. J. Frisch, "An efficient implementation of time-dependent density-functional theory for the calculation of excitation energies of large molecules," *J. Chem. Phys.*, vol. 109, no. 19, pp. 8218–8224, 1998.

[42] E. R. Davidson, "The iterative calculation of a few of the lowest eigenvalues and corresponding eigenvectors of large real-symmetric matrices," *J. Comp. Phys.*, vol. 17, no. 1, pp. 87–94, 1975.

[43] J. Brabec, L. Lin, M. Shao, N. Govind, C. Yang, Y. Saad, and E. G. Ng, "Efficient algorithms for estimating the absorption spectrum within linear response TDDFT," *J. Chem. Theory Comput.*, vol. 11, no. 11, pp. 5197–5208, 2015.

[44] Y. Wang, K. Lopata, S. A. Chambers, N. Govind, and P. V. Sushko, "Optical absorption and band gap reduction in $(\mathrm{fe}_{1-x}\mathrm{cr}_x)_2\mathrm{o}_3$ solid solutions: A first-principles study," *J. Phys. Chem. C*, vol. 117, no. 48, pp. 25504–25512, 2013.

[45] S. Tussupbayev, N. Govind, K. Lopata, and C. J. Cramer, "Comparison of real-time and linear-response time-dependent density functional theories for molecular chromophores ranging from sparse to high densities of states," *J. Chem. Theory Comput.*, vol. 11, no. 3, pp. 1102–1109, 2015.

[46] J. I. Fuks, P. Elliott, A. Rubio, and N. T. Maitra, "Dynamics of charge-transfer processes with time-dependent density functional theory," *J. Phys. Chem. Lett.*, vol. 4, no. 5, pp. 735–739, 2013.

[47] J. I. Fuks, K. Luo, E. D. Sandoval, and N. T. Maitra, "Time-resolved spectroscopy in time-dependent density functional theory: An exact condition," *Phys. Rev. Lett.*, vol. 114, p. 183002, May 2015.

[48] V. A. Mandelshtam and H. S. Taylor, "Harmonic inversion of time signals and its applications," *J. Chem. Phys.*, vol. 107, no. 17, pp. 6756–6769, 1997.

[49] M. R. Wall and D. Neuhauser, "Extraction, through filter-diagonalization, of general quantum eigenvalues or classical normal mode frequencies from a small number of residues or a short-time segment of a signal. i. theory and application to a quantum-dynamics model," *J. Chem. Phys.*, vol. 102, no. 20, pp. 8011–8022, 1995.

[50] V. A. Mandelshtam and H. S. Taylor, "A low-storage filter diagonalization method for quantum eigenenergy calculation or for spectral analysis of time signals," *J. Chem. Phys.*, vol. 106, no. 12, pp. 5085–5090, 1997.

[51] V. A. Mandelshtam, H. S. Taylor, and A. Shaka, "Application of the filter diagonalization method to one-and two-dimensional nmr spectra," *J. Mag. Res.*, vol. 133, no. 2, pp. 304–312, 1998.

[52] A. George Jr, *Essentials of Padé approximants*. Elsevier, 1975.

[53] S. Dey and R. Mittra, "Efficient computation of resonant frequencies and quality factors of cavities via a combination of the finite-difference time-domain technique and the padé approximation," *IEEE Microw. Guided W.*, vol. 8, no. 12, pp. 415–417, 1998.

[54] W.-H. Guo, W.-J. Li, and Y.-Z. Huang, "Computation of resonant frequencies and quality factors of cavities by fdtd technique and padé approximation," *IEEE Microw. Wirel. Co.*, vol. 11, no. 5, pp. 223–225, 2001.

[55] J. Makhoul, "Linear prediction: A tutorial review," *Proc. IEEE*, vol. 63, no. 4, pp. 561–580, 1975.

[56] R. Roy, B. Sumpter, D. Noid, and B. Wunderlich, "Estimation of dispersion relations from short-duration molecular dynamics simulations," *J. Phys. Chem.*, vol. 94, no. 15, pp. 5720–5729, 1990.

[57] G.-J. Kroes, M. R. Wall, J. W. Pang, and D. Neuhauser, "Avoiding long propagation times in wave packet calculations on scattering with resonances: A new algorithm involving filter diagonalization," *J. Chem. Phys.*, vol. 106, no. 5, pp. 1800–1807, 1997.

[58] D. Hofmann and S. Kümmel, "Self-interaction correction in a real-time kohn-sham scheme: Access to difficult excitations in time-dependent density functional theory," *J. Chem. Phys.*, vol. 137, no. 6, p. 064117, 2012.

[59] A. Szabo and N. S. Ostlund, *Modern quantum chemistry: Introduction to advanced electronic structure theory*. Courier Corporation, 1989.

[60] S. D. George, T. Petrenko, and F. Neese, "Time-dependent density functional calculations of ligand k-edge x-ray absorption spectra," *Inorg. Chim. Acta*, vol. 361, no. 4, pp. 965–972, 2008.

[61] T. Noro, M. Sekiya, and T. Koga, "Segmented contracted basis sets for atoms h through xe: Sapporo-(dk)-nzp sets (n= d, t, q)," *Theor. Chem. Acc.*, vol. 131, no. 2, pp. 1–8, 2012.

[62] P. Stephens, F. Devlin, C. Chabalowski, and M. J. Frisch, "Ab initio calculation of vibrational absorption and circular dichroism spectra using density functional force fields," *J. Phys. Chem.*, vol. 98, no. 45, pp. 11623–11627, 1994.

[63] R. G. Fernando, M. C. Balhoff, and K. Lopata, "X-ray absorption in insulators with non-hermitian real-time time-dependent density functional theory," *J. Chem. Theory Comput.*, vol. 11, no. 2, pp. 646–654, 2015.

[64] K. R. Wilson, B. S. Rude, T. Catalano, R. D. Schaller, J. G. Tobin, D. T. Co, and R. Saykally, "X-ray spectroscopy of liquid water microjets," *J. Phys. Chem. B*, vol. 105, no. 17, pp. 3346–3349, 2001.

[65] W. D. Derricotte and F. A. Evangelista, "Simulation of x-ray absorption spectra with orthogonality constrained density functional theory," *Phys. Chem. Chem. Phys.*, vol. 17, no. 22, pp. 14360–14374, 2015.

[66] S. Mitra-Kirtley, O. C. Mullins, J. Van Elp, S. J. George, J. Chen, and S. P. Cramer, "Determination of the nitrogen chemical structures in petroleum asphaltenes using xanes spectroscopy," *J. Am. Chem. Soc.*, vol. 115, no. 1, pp. 252–258, 1993.

[67] A. Vairavamurthy and S. Wang, "Organic nitrogen in geomacromolecules: insights on speciation and transformation with k-edge xanes spectroscopy," *Env. Sci. Tech.*, vol. 36, no. 14, pp. 3050–3056, 2002.

Chapter 4. Attosecond Charge Migration with TDDFT: Accurate Dynamics from a Well-Defined Initial State

4.1 Introduction

Recall from chapter 1 that the adiabatic approximation has been shown to qualitatively fail for TDDFT calculations of excited state dynamics if there is a significant change in the electron density. In order to obtain charge migration dynamics for high harmonic generation studies, we investigate the ability of time-dependent density functional theory (TDDFT) to capture attosecond valence electron dynamics resulting from sudden X-ray ionization of a core electron.[1] Here, for the ionized core electron, the initial state can be constructed unambiguously, allowing for a simple test of the accuracy of the dynamics. The response following nitrogen K-edge ionization in nitrosobenzene shows excellent agreement with fourth order algebraic diagrammatic construction (ADC(4)) results, suggesting that a properly chosen initial state allows TDDFT to adequately capture attosecond charge migration. Visualizing hole motion using an electron localization picture (ELF), we provide an intuitive chemical interpretation of the charge migration as a time-dependent superposition of Lewis-dot resonance structures. Coupled with the initial state solution to obtain such dynamics with TDDFT, this chemical picture facilitates interpretation of electron response.

Modeling attosecond electronic dynamics in molecules is important for a range of excited state processes such as light harvesting, photochemistry, and pump-probe photoelectron spectroscopy. Here, time-dependent simulations are necessary to capture the coherent response of the electron density, typically under intense laser fields or following ionization. Popular electronic structure approaches to calculate the relevant electron dynamics include: time-dependent Hartree-Fock[2–4], coupled cluster[5–7], configuration interaction[8–10], multiconfiguration[11–14], among others. For the case of large molecules, where the system size precludes correlated techniques, time-dependent density functional theory (TDDFT) is often

This chapter has been reprinted with minor changes from its original format in Bruner, A., et al, J. Phys. Chem. Lett., 2017, 8 (17), pp 3991-3996. with permission by the authors and the journal.

the method of choice. TDDFT has a good track record for correctly capturing challenging processes such as strong-field ionization[15–17], charge transfer[18,19], double excitations[20,21], above threshold resonances[22,23], X-ray absorption[24–28],and high harmonic generation[29,30], but applications to coherent electron dynamics are less reliable.

Broadly speaking, dynamics simulations with TDDFT have two sources of error: lack of an exact DFT functional and the choice of initial state for propagation. For the ground state, all practical DFT functionals are approximate, leading to self-interaction errors[31,32] and incorrect Coulomb potentials[33,34]. While there has been significant progress towards addressing these issues for ground state DFT functionals,[31,35–39] TDDFT is faced with the additional challenges related to a formal dependence of the functional on the complete history of the density[40]. Adiabatic TDDFT, which neglects the density's time-dependence, has been shown to qualitatively fail for the case of 1D model systems[41–44] and also leads to non-physical peak shifting in resonant excitations.[45–47] Although adiabatic TDDFT cannot be used to drive a system to an excited state, real-time (RT) TDDFT using a linear response initial state has shown promise for electronic excited state absorption[48,49]. For excited state calculations, however, dynamics can be highly sensitive to the choice of initial state for time propagation[50,51], and for some processes (e.g., electron/hole dynamics), the initial (complex) wavefunction should include all phase information, which can be challenging to compute. Provided the "correct" initial state, the ability of adiabatic TDDFT to capture electron dynamics in molecules remains relatively unstudied; thus, validating the accuracy of TDDFT is a crucial step towards modeling coherent processes.

The goal of this work is to demonstrate that TDDFT gives accurate dynamics for a specific example of ionization triggered hole migration. Additionally, using an electron localization function (ELF), we provide a chemical picture of charge migration as the superposition of Lewis-dot resonance structures. Since many attosecond electron dynamics experiments are still in their infancy, a direct comparison to experiment is not yet possible. Thus, we instead

compare to the results of previous ADC(4) calculations by Cederbaum and co-workers[52], where they demonstrated that rapid core-hole ionization can cause coherent valence hole motion across a nitrosobenzene molecule.[52] These dynamics manifest as a satellite peak in experimental N K-edge X-ray absorption near-edge structure (XANES) spectra.[53] Our dynamics simulations are related to the satellite via the hole migration frequency (shake-up energy). ADC methods are essentially a limited space configuration interaction within a perturbative framework. They capture electron correlation beyond mean-field and can yield highly accurate results, but computational cost grows significantly with increasing order.[54,55] Here, the charge migration of interest takes approximately 1.4 fs, well within the timescales of Auger decay for this system ($\sim$6 fs).[52,56] This is an ideal case-study for TDDFT since it involves a well-defined initial state, and thus only tests the validity of the functional.

One of the difficulties faced by TDDFT is its failure to resonantly drive systems to an excited state and capture subsequent dynamics. This is due to two general sources of error. The first is the lack of an exact DFT functional, and consequently, the approximate functionals introduce self-interaction errors[31,32] and incorrect Coulomb potentials[33,34]. Although there has been significant progress toward addressing these issues for ground state DFT functionals,[31,35–39] excited state TDDFT is also faced with challenges imposed by the adiabatic approximation. This approximation neglects the density's time-dependence upon its complete history[40]. Without this information, TDDFT qualitatively fails to capture dynamics for 1D model systems[41–44] and also leads to non-physical peak shifting in resonant excitations.[45–47] As such, adiabatic TDDFT cannot be used to drive a system to an excited state. To address this, real-time (RT) TDDFT using a linear response initial state has shown promise for electronic excited state absorption[48,49], although dynamics in the excited state can be highly sensitive to the choice of initial state for time propagation[50,51]. Furthermore, for some processes (e.g., electron/hole dynamics) the initial (complex) wavefunction should include all phase information, which can be challenging to compute. Despite much discus-

sion, the ability of adiabatic TDDFT to capture electron dynamics for a "correct" initial condition remains relatively unstudied. Here, we use the results of previous calculations by Cederbaum and co-workers[52] as a benchmark to demonstrate that for a well-described initial condition, adiabatic TDDFT can accurately capture the resulting attosecond charge migration, making this work a key step towards modeling coherent processes.

4.2 Description of State Preparation

All simulations use the equilibrium neutral geometry of nitrosobenzene, which was optimized using the PBE0 functional[57] and aug-cc-pVTZ basis set[58]. Although DFT functionals have been extensively benchmarked against ground state[59] and response properties[60,61], their accuracy for attosecond dynamics is far less understood. To evaluate the performance of TDDFT, we use a selection of functionals within the same family including Hartree-Fock, PBE[62], PBE0[57], and LC-PBE* (optimally tuned range-separated)[63]. For all, we use the Sadlej+ basis[64,65]. Basis set convergence data are included in Appendix B. The initial state was created by converging the neutral molecule to its electronic ground state, followed by removal of an electron from the "1s" molecular orbital on the nitrogen atom without performing a subsequent SCF energy optimization. The density matrix was then propagated field-free from this non-stationary initial state. (See Computational Details section at the end of this chapter.) Since core MOs are essentially atomic-like, this initial condition is a good approximation of "sudden" resonant X-ray ionization at the nitrogen K-edge ($\sim$ 410 eV). Modeling the resulting electronic dynamics thus offers a simple validation of TDDFT's ability to capture charge migration, as there is no initial state problem, and any inaccuracies arise only from issues with the exchange-correlation functional. This is in contrast with valence ionization (e.g., via tunneling or multiphoton ionization), where in general the initial state must be constructed from a linear combination of holes in the multiple MOs, with a complex phase between them.

4.3 Results

Figure 4.1 shows the resulting hole density along the length of the nitrosobenzene molecule following sudden creation of a N 1s core-hole, where the hole density has been integrated along the x and y directions to yield $Q(z,t)$. Here, we show TD-PBE0 (a global hybrid) results, selected based upon good agreement with the reference ADC(4) calculation. Results using other functionals are described later. The core-hole localized on the N is essentially static in time, which results in a large amount of valence electron migration to the nitrogen atom shown as the large negative peak. Looking at hole density around the oxygen atom and the C4 carbon (opposite the nitroso on the ring), a clear signature of valence charge migration is visible. Approximately 0.3 fs following ionization, a hole is created on the O atom (point A on bottom plot) as the electrons flow from the O towards the N atom. Subsequently, at $t \simeq 0.5$ fs the hole enters the ring across the C1 atom (B) before reaching the C4 carbon at $t \simeq 0.7$ fs (C). This represents hole migration across the molecule with a timescale of $\simeq 0.7$ fs. The hole then begins to migrate back across the molecule, returning across the C1 carbon (D) to the oxygen (E) with a round trip migration of $T \simeq 1.4$ fs. Due to the lack of dephasing in these simulations, the hole migration is time-reversible and thus oscillates forever. These observed hole migration dynamics are consistent with the ADC(4) results (Fig. 3 in Ref. 52).

There are some qualitative differences between the ADC(4) and TDDFT results, however. For example, the hole density on the nitroso carbon (C1), shows persistent dynamics over the simulation, where rather than seeing a coherent charge motion, a steady amount of hole density is maintained on the C1 carbon. This can be attributed to excitations corresponding to local charge motion between neighboring atoms. Such excitations result from the "sudden" ionization approximation, which imparts an impulse to the system.

The hole density can provide additional information about the time dependent hole motion. Fig. 4.2 (top) shows snapshots of the hole density (blue) as the hole migrates

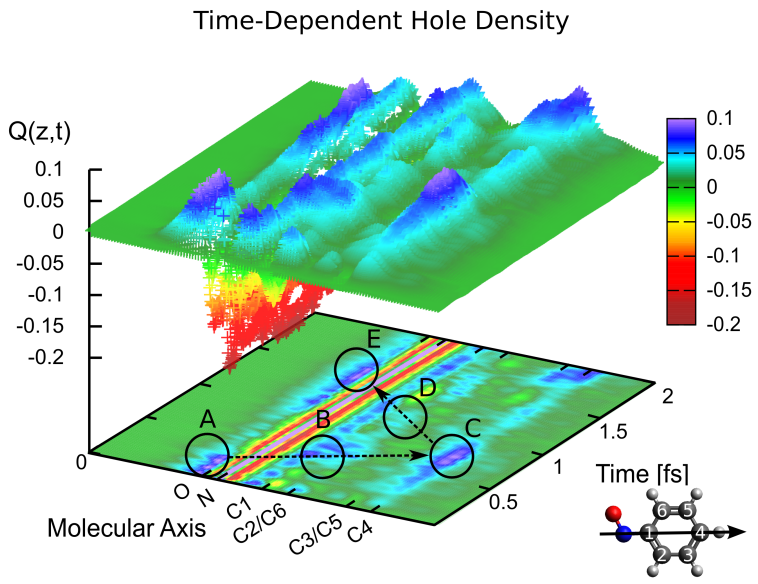

Figure 4.1: Evolution of the hole density $Q(z,t)$ in nitrosobenzene following nitrogen K-edge core-hole ionization. The hole (positive) moves to the oxygen, to the C1 carbon and eventually the C4 carbon, before oscillating back (period $\simeq$ 1.4 fs). This agrees well with the ADC(4) hole dynamics (Fig. 3 in Ref. 52).

through points A-E of Fig. 4.1 during a complete cycle of valence hole motion from the N to the C4 and back. In addition to the hole migration, the N core-hole draws charge from the neighboring oxygen and carbon atoms, resulting in a shell of increased electron density around N (red). Moreover, localized excitations not relevant to the hole migration are visible in the ring as alternating charge (red) and depletion (blue). These dynamics can obfuscate the hole motion, which makes hole densities hard to interpret. To study these systems, physics and chemistry often represent such dynamical information in several different ways.

A more physical interpretation can be obtained from the time-dependent electron localization function (TDELF)[66,67], which provides a picture of the hole migration that is consistent with the density, but emphasizes relevant features (e.g. lone pairs, bonds, holes). (See Computational Details.) Fig. 4.2 (middle) shows snapshots of the TDELF 1.5 $\mathring{A}$ above the plane of the molecule to highlight how the hole (magenta circles) migrates through the π-system. Initially, the π-electrons are delocalized in the ring (A), then move to a superpo-

sition of two paths that the hole can travel around the ring (B), and form the double bonds on the sides of the ring (C) before returning back (D & E). Since the ELF is derived from an expectation value of the density, it shows a weighted average (smearing) of the hole across nearly equivalent pairs of carbons C2/C6 and C3/C5. In contrast, the hole is pronounced on C4 because there is only one carbon in this chemical environment. By emphasizing bonds and lone pairs, the TDELF not only gives a good picture of the hole motion, but also yields dynamics qualitatively suggestive of organic chemistry resonance forms.

In the context of organic chemistry, Lewis dot resonance structures are employed to describe bonds, lone pairs, localized electrons, etc., with the resonance structures corresponding to equivalent electron arrangements in a molecule. From this picture, mechanisms are proposed to illustrate general movement of the charge. Fig. 4.2 (bottom) shows the expected "electron pushing" mechanism in nitrosobenzene following the removal of a N lone pair electron. Initially the electrons are delocalized around the π ring on the aromatic at $t = 0$, with a rapid contraction of electrons around the N (point A). Next, (B) the hole migrates into the ring, which involves the radical moving both on the right (up path) and the left (down path) sides of the ring. Once the hole reaches C4 (point C) the ring has two double bonds. Migration of the hole back to the N proceeds in a reverse fashion (through D & E). In this chemistry picture, it is understood that such molecules exist in a superposition of the resonance structures, as electrons are delocalized on the timescales of chemical reactions. Although this evolution of the resonance structures corresponds to a lone pair electron removed from the valence rather than core-hole driven dynamics (TDELF), it provides a general picture of the "stops along the way".

Also, it is important to assess the performance of various DFT functionals for capturing the dynamics. Here, we have compared Hartree-Fock (HF) and the PBE0 functionals. A full evaluation of four functionals from the same family: Hartree-Fock, PBE, PBE0, and optimally tuned LC-PBE* has been included in Appendix B. As before, the TDDFT was

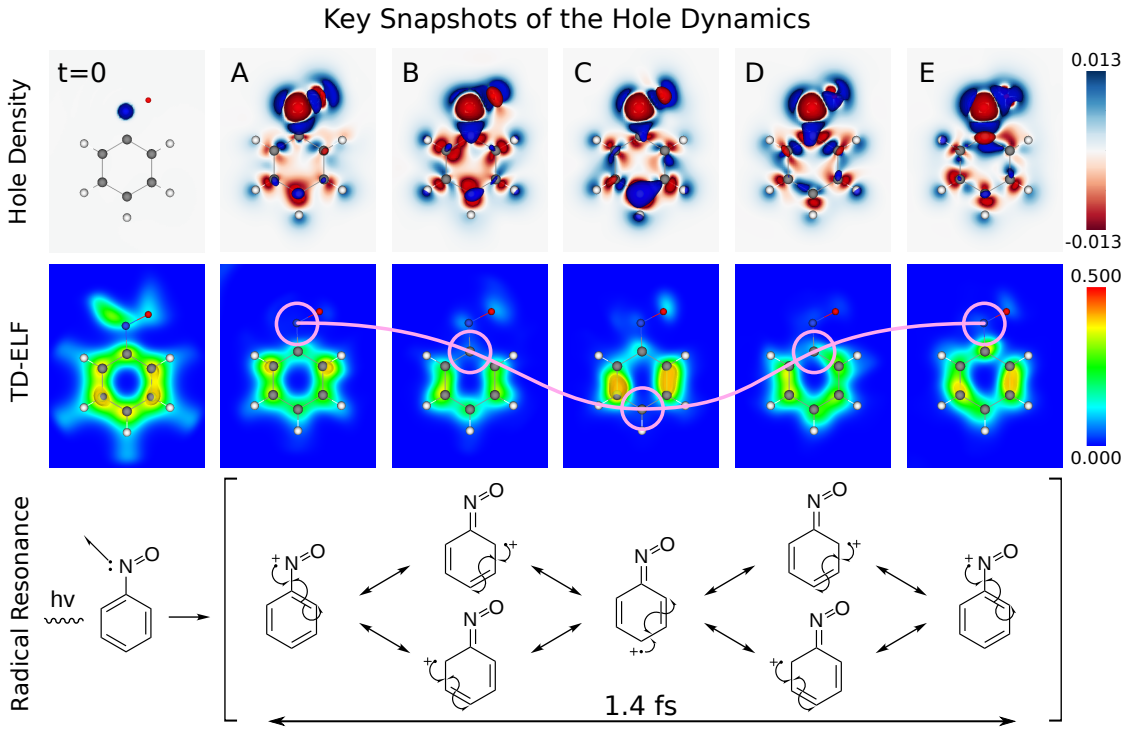

Figure 4.2: Snapshots of the hole migration at points points A-E from Fig. 4.1 represented in three different ways. The hole density (top) shows electron contraction around the N atom as well as one oscillation of the hole from N to C4 and back. In the time-dependent electron localization function (TDELF; middle), the hole manifests as a region of decreased electron localization (magenta circles) and can be qualitatively mapped onto the an evolving superposition of Lewis dot resonance structures (bottom). For example, a hole (magenta circles) localized on C4 (snapshot C) corresponds to a C4 radical with two parallel double bonds in the aromatic ring, demonstrating that attosecond hole migration can be viewed as an evolving superposition of resonance structures.

initialized by creating a hole in the neutral N 1s MO using the respective functional. The resulting TDDFT hole occupations, as well as a digitization of the reported ADC(4) results, are shown in Fig. 4.3. Note that the orbital ordering is different between TDHF and PBE0, so we determined these by inspecting the shape and symmetry of the dominant orbitals (see appendix for orbital plots). Also, since the ADC(4) results only showed population in one of the degenerate HOMO-1/HOMO-2, we likewise only present populations for one of a degenerate pair of orbitals. Summing over all of the orbitals yields the number of electrons, which is conserved.

In Fig. 4.3(a), the ADC(4) result shows clear, coupled hole occupations between the dominant orbitals, as the hole moves from one to another. Fig. 4.3(b) shows the TDHF hole-occupations using the same orbitals, rather than those with the largest hole dynamics. TDHF exhibits grossly incorrect dynamics, which is likely due to a lack of electron correlation. Not only does Hartree-Fock suffer from an incorrect orbital ordering, but it also fails to capture the hole dynamics in the respective orbitals. To test this, we computed the dynamics using the PBE0 functional, as shown in Fig. 4.3(c).

Pure DFT functionals like PBE (shown in Appendix B) have two probable sources of error: self-interaction and an incorrect long-range Coulomb potential. The incorrect Coulomb potential is also expected to yield nonphysical hole motion, similar to the well-known result that TDDFT needs exact exchange to capture charge transfer excitations.[18] For the hybrid PBE0 functional, the addition of 25% exact exchange yields reduced self-interaction and an improved Coulomb potential, providing a good balance of the two. (See Appendix B for additional details.) The resulting dynamics agree well with the ADC(4) data, capturing the $\sim$1.4 fs period of oscillation, coherent population transfer, and relatively fewer high frequency dynamics than the HF case. As the TDDFT calculation involves all MOs, the rapid ionization can induce excitations (ripples) unrelated to hole migration. These are not present in the ADC(4) calculation, which only correlated four valence orbitals, and

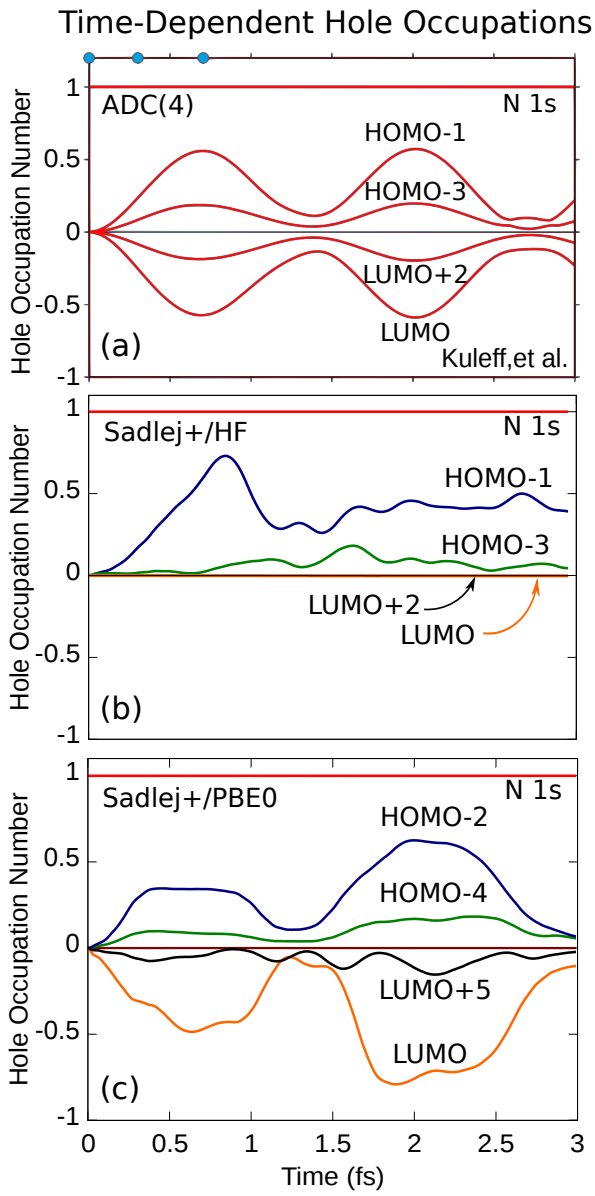

Figure 4.3: Hole occupations of the dominant molecular orbitals in nitrosobenzene following N K-edge ionization. (a) ADC(4) results (digitized with permission from Ref. 52; copyright 2016 by American Physical Society). (b) Hartree-Fock shows poor agreement due to the lack of electron correlation. (c) TD-PBE0 shows good agreement with ADC(4) results over two cycles of the hole migration. These results suggest that hybrid TDDFT adequately captures core-hole triggered valence dynamics. An evaluation of additional functionals is included in the appendix.

the excitations we observe can involve different occupied-virtual orbital pairs from the four shown.

4.4 Conclusions

In conclusion, these results for nitrosobenzene, when taken as a (w)hole, suggest that given a correct choice of initial state, TDDFT with a hybrid functional can capture hole migration consistent with correlated methods. Here, propagating from a well-defined initial state gives accurate dynamics, despite the approximate description of electron correlation. These results are quite unexpected, especially considering that all calculations used adiabatic DFT functionals. This is not simply a matter of "cherry-picking" a functional to get the desired answer. Indeed, non-adiabatic general purpose functionals do not exist. Surprisingly, making the adiabatic approximation is perhaps not as critical as predicted for model systems. One interpretation is that deficiencies in the ground state functional (e.g. self-interaction errors, long-range Coulomb potential errors, etc.) may dominate over errors due to the adiabatic approximation, yet this remains a topic of ongoing study.

A practical recipe is to break the simulation into two steps to "bypass" the issues with adiabatic TDDFT: (i) determine the initial state after interaction with pump, (ii) propagate starting from this state, either field-free or with a probe pulse. This approach hinges on an accurate description of the initial state in step (i). Other than simple unambiguous cases like core-holes, this requires going beyond crude occupation-based approximations and ideally should include coherence information in the complex wavefunction, e.g., phases between orbitals. Future work will explore the validity for tunnel ionization triggered hole migration, where dynamics arise from a superposition of holes in multiple valence molecular orbitals.

4.5 Computational Details

For the time propagation we use a development version of the real-time TDDFT module[68] in NWChem.[69] This code uses a Gaussian basis set to propagate the one-electron density

matrix in the time domain. Gaussian basis functions allow for a simple description of core states, creation of core-holes, and efficient use of hybrid DFT functionals. The equation of motion is:

$$i\frac{\partial \mathbf{P}'(t)}{\partial t} = [\mathbf{F}'(t), \mathbf{P}'(t)]\,, \tag{4.1}$$

where $\mathbf{F}'(t)$ and $\mathbf{P}'(t)$ are the Fock and density matrices, respectively, in the canonical basis. This expression is then integrated by a second-order Magnus (exponential midpoint) propagator:

$$\mathbf{P}'(t+\Delta t) = e^{-i\mathbf{F}'(t+\frac{\Delta t}{2})\Delta t}\mathbf{P}'(t)e^{i\mathbf{F}'(t+\frac{\Delta t}{2})\Delta t} \tag{4.2}$$

Each propagation step is then corrected using a self-consistent scheme. For additional details of the implementation see Ref. 68, and for a review of other propagators see Ref. 70.

The resulting dynamics were interpreted multiple ways. The hole density, which is a measure of the absence of charge with respect to the neutral molecule, is given by

$$Q(r,t) = \rho_+(r,t) - \rho_0(r) \tag{4.3}$$

where ρ_+ is the time-dependent density of the cation and ρ_0 is the neutral ground state density. The hole density is negative for regions with an increase in electron density and positive for regions with an decrease of electron density. The time-dependent molecular orbital hole occupations, which express the population transfer into the valence excited states, are computed via projection of the density matrix ($\mathbf{P}$) onto the ground state eigenvectors ($\mathbf{C}$) of the Fock matrix, all in the canonical basis (denoted by the prime):

$$n_k(t) = [\mathbf{C}'^{\dagger}\mathbf{P}'(t)\mathbf{C}']_{kk} \tag{4.4}$$

Finally, the time-dependent electron localization function (TDELF)[66,67] was computed to visualize the charge migration in terms of electron localization changes, rather than densi-

ties. A TDELF highlights the presence of holes due to increased localization of the electrons surrounding that hole. The time-dependent electron localization function (TDELF) is defined as:

$$\eta(r,t) = \frac{1}{1 + (D_\sigma(r,t)/D^0_\sigma(r,t))^2}, \tag{4.5}$$

where

$$D_\sigma(r,t) = \tau_\sigma(r,t) - \frac{1}{4}\frac{|\nabla n_\sigma(r,t)|^2}{n_\sigma(r,t)} - \frac{|j_\sigma(r,t)|^2}{n_\sigma(r,t)}, \tag{4.6}$$

and $D^0_\sigma(r,t) = (3/5)(6\pi)^{2/3} n_\sigma(r,t)^{5/3}$ is the kinetic energy density function for a homogeneous electron gas, where $n_\sigma(r,t)$ is the time-dependent density function for electrons with spin σ. In $D_\sigma(r,t)$, $\tau_\sigma(r,t) = \sum_i^{N_\sigma} |\nabla\psi_i(r,t)|^2$ and $j_\sigma(r,t)$ represents the kinetic energy density function and current density, respectively. All quantities were computed in the atomic orbital basis and then evaluated on a Cartesian grid.

4.6 References

[1] A. Bruner, S. Hernandez, F. Mauger, P. M. Abanador, D. J. LaMaster, M. B. Gaarde, K. J. Schafer, and K. Lopata, "Attosecond charge migration with tddft: Accurate dynamics from a well-defined initial state," *J Phys. Chem. Lett.*, vol. 8, no. 17, pp. 3991–3996, 2017.

[2] K. C. Kulander, "Time-dependent hartree-fock theory of multiphoton ionization: Helium," *Phys. Rev. A*, vol. 36, no. 6, p. 2726, 1987.

[3] X. Li, S. M. Smith, A. N. Markevitch, D. A. Romanov, R. J. Levis, and H. B. Schlegel, "A time-dependent hartree–fock approach for studying the electronic optical response of molecules in intense fields," *Phys. Chem. Chem. Phys.*, vol. 7, no. 2, pp. 233–239, 2005.

[4] C. M. Isborn and X. Li, "Singlet-triplet transitions in real-time time-dependent hartree-fock/density functional theory," *J. Chem. Theory Comput.*, vol. 5, no. 9, pp. 2415–2419, 2009.

[5] D. R. Nascimento and A. E. DePrince, "Simulation of near-edge x-ray absorption fine structure with time-dependent equation-of-motion coupled-cluster theory," *J. Phys. Chem. Lett.*, vol. 8, no. 13, pp. 2951–2957, 2017.

[6] C. Huber and T. Klamroth, "Explicitly time-dependent coupled cluster singles doubles calculations of laser-driven many-electron dynamics," *J. Chem. Phys.*, vol. 134, no. 5, p. 054113, 2011.

[7] S. Kvaal, "Ab initio quantum dynamics using coupled-cluster," *J. Chem. Phys.*, vol. 136, no. 19, p. 194109, 2012.

[8] P. Krause, T. Klamroth, and P. Saalfrank, "Time-dependent configuration-interaction calculations of laser-pulse-driven many-electron dynamics: Controlled dipole switching in lithium cyanide," *J. Chem. Phys.*, vol. 123, no. 7, p. 074105, 2005.

[9] A. E. DePrince III, M. Pelton, J. R. Guest, and S. K. Gray, "Emergence of excited-state plasmon modes in linear hydrogen chains from time-dependent quantum mechanical methods," *Phys. Rev. Lett.*, vol. 107, no. 19, p. 196806, 2011.

[10] P. Krause, J. A. Sonk, and H. B. Schlegel, "Strong field ionization rates simulated with time-dependent configuration interaction and an absorbing potential," *J. Chem. Phys.*, vol. 140, no. 17, p. 174113, 2014.

[11] D. Haxton and C. McCurdy, "Ultrafast population transfer to excited valence levels of a molecule driven by x-ray pulses," *Phys. Rev. A*, vol. 90, no. 5, p. 053426, 2014.

[12] H.-D. Meyer, U. Manthe, and L. S. Cederbaum, "The multi-configurational time-dependent hartree approach," *Chem. Phys. Lett.*, vol. 165, no. 1, pp. 73–78, 1990.

[13] M. Nest, T. Klamroth, and P. Saalfrank, "The multiconfiguration time-dependent hartree–fock method for quantum chemical calculations," *J. Chem. Phys.*, vol. 122, no. 12, p. 124102, 2005.

[14] T. Sato and K. L. Ishikawa, "Time-dependent complete-active-space self-consistent-field method for multielectron dynamics in intense laser fields," *Phys. Rev. A*, vol. 88, no. 2, p. 023402, 2013.

[15] X.-M. Tong and S.-I. Chu, "Time-dependent density-functional theory for strong-field multiphoton processes: Application to the study of the role of dynamical electron correlation in multiple high-order harmonic generation," *Phys. Rev. A*, vol. 57, no. 1, p. 452, 1998.

[16] M. Lein and S. Kümmel, "Exact time-dependent exchange-correlation potentials for strong-field electron dynamics," *Phys. Rev. Lett.*, vol. 94, no. 14, p. 143003, 2005.

[17] A. Sissay, P. Abanador, F. Mauger, M. Gaarde, K. J. Schafer, and K. Lopata, "Angle-dependent strong-field molecular ionization rates with tuned range-separated time-dependent density functional theory," *J. Chem. Phys.*, vol. 145, no. 9, p. 094105, 2016.

[18] A. Dreuw, J. L. Weisman, and M. Head-Gordon, "Long-range charge-transfer excited states in time-dependent density functional theory require non-local exchange," *J. Chem. Phys.*, vol. 119, no. 6, pp. 2943–2946, 2003.

[19] T. Stein, L. Kronik, and R. Baer, "Reliable prediction of charge transfer excitations in molecular complexes using time-dependent density functional theory," *J. Am. Chem. Soc.*, vol. 131, no. 8, pp. 2818–2820, 2009.

[20] C. M. Isborn and X. Li, "Modeling the doubly excited state with time-dependent hartree–fock and density functional theories," *J. Chem. Phys.*, vol. 129, no. 20, p. 204107, 2008.

[21] S. Hirata and M. Head-Gordon, "Time-dependent density functional theory for radicals: An improved description of excited states with substantial double excitation character," *Chem. Phys. Lett.*, vol. 302, no. 5, pp. 375–382, 1999.

[22] T. Nakatsukasa and K. Yabana, "Photoabsorption spectra in the continuum of molecules and atomic clusters," *J. of Chem. Phys.*, vol. 114, no. 6, pp. 2550–2561, 2001.

[23] K. Lopata and N. Govind, "Near and above ionization electronic excitations with non-hermitian real-time time-dependent density functional theory," *J. Chem. Theory Comput.*, vol. 9, no. 11, pp. 4939–4946, 2013.

[24] R. G. Fernando, M. C. Balhoff, and K. Lopata, "X-ray absorption in insulators with non-hermitian real-time time-dependent density functional theory," *J. Chem. Theory Comput.*, vol. 11, no. 2, pp. 646–654, 2015.

[25] A. Bruner, D. LaMaster, and K. Lopata, "Accelerated broadband spectra using transition dipole decomposition and padé approximants," *J. Chem. Theory Comput.*, vol. 12, no. 8, pp. 3741–3750, 2016.

[26] W. Liang, S. A. Fischer, M. J. Frisch, and X. Li, "Energy-specific linear response tdhf/t-ddft for calculating high-energy excited states," *J. of Chem. Theory Comput.*, vol. 7, no. 11, pp. 3540–3547, 2011.

[27] A. D. Baczewski, L. Shulenburger, M. P. Desjarlais, S. B. Hansen, and R. J. Magyar, "X-ray thomson scattering in warm dense matter without the chihara decomposition," *Phys. Rev. Lett.*, vol. 116, no. 11, p. 115004, 2016.

[28] S. Hu, L. Collins, V. Goncharov, T. Boehly, R. Epstein, R. McCrory, and S. Skupsky, "First-principles opacity table of warm dense deuterium for inertial-confinement-fusion applications," *Phys. Rev. E*, vol. 90, no. 3, p. 033111, 2014.

[29] J. Heslar, D. A. Telnov, and S.-I. Chu, "Subcycle dynamics of high-harmonic generation in valence-shell and virtual states of ar atoms: A self-interaction-free time-dependent density-functional-theory approach," *Phys. Rev. A*, vol. 91, no. 2, p. 023420, 2015.

[30] A. Wardlow and D. Dundas, "High-order-harmonic generation in benzene with linearly and circularly polarized laser pulses," *Phys. Rev. A*, vol. 93, no. 2, p. 023428, 2016.

[31] J. P. Perdew and A. Zunger, "Self-interaction correction to density-functional approximations for many-electron systems," *Phys. Rev. B*, vol. 23, no. 10, p. 5048, 1981.

[32] E. Ruiz, S. Alvarez, J. Cano, and V. Polo, "About the calculation of exchange coupling constants using density-functional theory: The role of the self-interaction error," *J. Chem. Phys.*, vol. 123, no. 16, p. 164110, 2005.

[33] A. Dreuw and M. Head-Gordon, "Failure of time-dependent density functional theory for long-range charge-transfer excited states: The zincbacteriochlorin- bacteriochlorin and bacteriochlorophyll- spheroidene complexes," *J. Am. Chem. Soc.*, vol. 126, no. 12, pp. 4007–4016, 2004.

[34] R. Magyar and S. Tretiak, "Dependence of spurious charge-transfer excited states on orbital exchange in tddft: Large molecules and clusters," *J. Chem. Theory Comput.*, vol. 3, no. 3, pp. 976–987, 2007.

[35] R. Baer, E. Livshits, and U. Salzner, "Tuned range-separated hybrids in density functional theory," *Ann. Rev. of Phys. Chem.*, vol. 61, pp. 85–109, 2010.

[36] Y. Zhao and D. G. Truhlar, "Density functional for spectroscopy: No long-range self-interaction error, good performance for rydberg and charge-transfer states, and better performance on average than b3lyp for ground states," *J. Phys. Chem. A*, vol. 110, no. 49, pp. 13126–13130, 2006.

[37] M. A. Marques and E. K. Gross, "Time-dependent density functional theory," *Annu. Rev. Phys. Chem.*, vol. 55, pp. 427–455, 2004.

[38] M. E. Casida and M. Huix-Rotllant, "Progress in time-dependent density-functional theory," *Ann. Rev. of Phys. Chem.*, vol. 63, pp. 287–323, 2012.

[39] J. Fuks and N. Maitra, "Charge transfer in time-dependent density-functional theory: Insights from the asymmetric hubbard dimer," *Phys. Rev. A*, vol. 89, no. 6, p. 062502, 2014.

[40] E. Runge and E. K. U. Gross, "Density-functional theory for time-dependent systems," *Phys. Rev. Lett.*, vol. 52, pp. 997–1000, Mar 1984.

[41] J. I. Fuks, P. Elliott, A. Rubio, and N. T. Maitra, "Dynamics of charge-transfer processes with time-dependent density functional theory," *J. Phys. Chem. Lett.*, vol. 4, no. 5, pp. 735–739, 2013.

[42] N. T. Maitra and D. G. Tempel, "Long-range excitations in time-dependent density functional theory," *J. Chem. Phys.*, vol. 125, no. 18, p. 184111, 2006.

[43] K. Giesbertz and E. Baerends, "Failure of time-dependent density functional theory for excited state surfaces in case of homolytic bond dissociation," *Chem. Phys. Lett.*, vol. 461, no. 4, pp. 338–342, 2008.

[44] R. Requist and O. Pankratov, "Adiabatic approximation in time-dependent reduced-density-matrix functional theory," *Phys. Rev. A*, vol. 81, no. 4, p. 042519, 2010.

[45] M. R. Provorse, B. F. Habenicht, and C. M. Isborn, "Peak-shifting in real-time time-dependent density functional theory," *J. Chem. Theory Comput.*, vol. 11, no. 10, pp. 4791–4802, 2015.

[46] J. I. Fuks, K. Luo, E. D. Sandoval, and N. T. Maitra, "Time-resolved spectroscopy in time-dependent density functional theory: An exact condition," *Phys. Rev. Lett.*, vol. 114, no. 18, p. 183002, 2015.

[47] S. Raghunathan and M. Nest, "The lack of resonance problem in coherent control with real-time time-dependent density functional theory," *J. Chem. Theory Comput.*, vol. 8, no. 3, pp. 806–809, 2012.

[48] S. A. Fischer, C. J. Cramer, and N. Govind, "Excited state absorption from real-time time-dependent density functional theory," *J. Chem. Theory Comput.*, vol. 11, no. 9, pp. 4294–4303, 2015.

[49] T. S. Nguyen, J. H. Koh, S. Lefelhocz, and J. Parkhill, "Black-box, real-time simulations of transient absorption spectroscopy," *J. Phys. Chem. Lett.*, vol. 7, no. 8, pp. 1590–1595, 2016.

[50] H. Eshuis and T. van Voorhis, "The influence of initial conditions on charge transfer dynamics," *Phys. Chem. Chem. Phys.*, vol. 11, no. 44, pp. 10293–10298, 2009.

[51] N. T. Maitra and K. Burke, "Demonstration of initial-state dependence in time-dependent density-functional theory," *Phys. Rev. A*, vol. 63, no. 4, p. 042501, 2001.

[52] A. I. Kuleff, N. V. Kryzhevoi, M. Pernpointner, and L. S. Cederbaum, "Core ionization initiates subfemtosecond charge migration in the valence shell of molecules," *Phys. Rev. Lett.*, vol. 117, no. 9, p. 093002, 2016.

[53] A. Slaughter, M. Banna, and C. McDowell, "Vapor-phase core photoelectron spectra of para-nitroaniline and nitrosobenzene," *Chem. Phys. Lett.*, vol. 98, no. 6, pp. 531–535, 1983.

[54] J. Schirmer, "Beyond the random-phase approximation: A new approximation scheme for the polarization propagator," *Phys. Rev. A*, vol. 26, no. 5, p. 2395, 1982.

[55] J. H. Starcke, M. Wormit, J. Schirmer, and A. Dreuw, "How much double excitation character do the lowest excited states of linear polyenes have?," *Chem. Phys.*, vol. 329, no. 1, pp. 39–49, 2006.

[56] M. Drescher, M. Hentschel, R. Kienberger, M. Uiberacker, V. Yakovlev, A. Scrinzi, T. Westerwalbesloh, U. Kleineberg, U. Heinzmann, and F. Krausz, "Time-resolved atomic inner-shell spectroscopy," *Nature*, vol. 419, no. 6909, pp. 803–807, 2002.

[57] C. Adamo and V. Barone, "Toward reliable density functional methods without adjustable parameters: The pbe0 model," *J. Chem. Phys.*, vol. 110, no. 13, pp. 6158–6170, 1999.

[58] T. H. Dunning Jr, "Gaussian basis sets for use in correlated molecular calculations. i. the atoms boron through neon and hydrogen," *J. Chem. Phys.*, vol. 90, no. 2, pp. 1007–1023, 1989.

[59] K. R. Brorsen, Y. Yang, M. V. Pak, and S. Hammes-Schiffer, "Is the accuracy of density functional theory for atomization energies and densities in bonding regions correlated?," *J. Phys. Chem. Lett.*, vol. 8, no. 9, pp. 2076–2081, 2017.

[60] M. Srebro, N. Govind, W. A. De Jong, and J. Autschbach, "Optical rotation calculated with time-dependent density functional theory: The or45 benchmark," *J. Phys. Chem. A*, vol. 115, no. 40, pp. 10930–10949, 2011.

[61] S. S. Leang, F. Zahariev, and M. S. Gordon, "Benchmarking the performance of time-dependent density functional methods," *J. Chem. Phys.*, vol. 136, no. 10, p. 104101, 2012.

[62] J. P. Perdew, K. Burke, and M. Ernzerhof, "Generalized gradient approximation made simple," *Phys. Rev. Lett.*, vol. 77, no. 18, p. 3865, 1996.

[63] H. Iikura, T. Tsuneda, T. Yanai, and K. Hirao, "A long-range correction scheme for generalized-gradient-approximation exchange functionals," *J. Chem. Phys.*, vol. 115, no. 8, pp. 3540–3544, 2001.

[64] A. J. Sadlej, "Medium-size polarized basis sets for high-level correlated calculations of molecular electric properties," *Collect. Czech. Chem. Commun.*, vol. 53, no. 9, pp. 1995–2016, 1988.

[65] M. E. Casida, C. Jamorski, K. C. Casida, and D. R. Salahub, "Molecular excitation energies to high-lying bound states from time-dependent density-functional response theory: Characterization and correction of the time-dependent local density approximation ionization threshold," *J. Chem. Phys.*, vol. 108, no. 11, pp. 4439–4449, 1998.

[66] T. Burnus, M. A. Marques, and E. K. Gross, "Time-dependent electron localization function," *Phys. Rev. A*, vol. 71, no. 1, p. 010501, 2005.

[67] A. D. Becke and K. E. Edgecombe, "A simple measure of electron localization in atomic and molecular systems," *J. Chem. Phys.*, vol. 92, no. 9, pp. 5397–5403, 1990.

[68] K. Lopata and N. Govind, "Modeling fast electron dynamics with real-time time-dependent density functional theory: Application to small molecules and chromophores," *J. Chem. Theory Comput.*, vol. 7, no. 5, pp. 1344–1355, 2011.

[69] M. Valiev, E. J. Bylaska, N. Govind, K. Kowalski, T. P. Straatsma, H. J. Van Dam, D. Wang, J. Nieplocha, E. Apra, and T. L. Windus, "Nwchem: A comprehensive and scalable open-source solution for large scale molecular simulations," *Comp. Phys. Comm.*, vol. 181, no. 9, pp. 1477–1489, 2010.

[70] A. Castro, M. A. Marques, and A. Rubio, "Propagators for the time-dependent kohn–sham equations," *J. Chem. Phys.*, vol. 121, no. 8, pp. 3425–3433, 2004.

Chapter 5. Modes and Metrics of Attosecond Charge Migration

5.1 Introduction

Attosecond electron dynamics underlie a range of applications spanning light harvesting to photochemistry. One important process is attosecond charge migration (CM), in which electrons coherently move from one location in a molecule to another following laser excitation or ionization. Modeling such experiments from first principles can be challenging, since intense fields of light drive the system beyond the perturbative linear-response regime. In the absence of a field, such correlation information, which is relevant to charge transport and photoelectric energy conversion, would otherwise remain hidden. The rewards, however, are significant as the potentially complex quantum evolution can reveal how electrons and holes are correlated. Furthermore, CM calculations may offer valuable insight for experimentally creating more localized holes, effects of laser polarization on CM dynamics, and "guiding" holes driven by a field selectively (e.g. in branched molecules).

As attosecond experiments have advanced, the ability to probe charge migration has grown from studying atoms[1,2] and diatomics[3,4] to small molecules and larger systems[5,6]. The experimental techniques using high harmonic generation and pump-probe spectroscopies continue to lead these efforts due to the high degree of temporal resolution necessary to capture the dynamics on their native time scales[3,4,7,8]. For such methods, the system is suddenly ionized, leaving a hole that can move over a few attoseconds. The resulting evolution of the hole can be challenging to interpret for molecular systems, and a theoretical description holds the potential to offer valuable insight.

Several methods exist for calculating electron dynamics such as time-dependent Hartree-Fock[9–12], multiconfiguration self-consistent field[13–17], configuration interaction[18–21], coupled cluster[22–24], and time-dependent density functional theory[25–37]. For hole dynamics following ionization, it is often useful to compute the hole density, which is positive for regions with a decrease in electron density and negative for regions with an increase in electron density.

Here, the time-dependent density of the cation ρ_+ is subtracted from that of the neutral ground state ρ_0 to yield the hole density ρ_H.

$$\rho_H(r,t) = \rho_0(r) - \rho_+(r,t) \tag{5.1}$$

This time-dependent quantity shows an absence (or excess) of charge relative to the neutral molecule and emphasizes holes.

In this Letter, we offer a way to both identify and chemically predict charge migration dynamics following ionization. We illustrate our method with five molecules, four of which are valence-hole and one core-hole triggered valence CM: For this work, we study four cases of valence-hole triggered charge migration and one carbonyl sulfide (OCS), iodoacetylene (ICCH), hexatriene ($CH_2(CH)_4CH_2$), 1,2-diethenyl diborane ($CH_2CH(BH)_2CHCH_2$), and nitrosobenze (ONC_6H_5), respectively. This spans a valence hole in the π system with adjacent double bonds (cumulenes), valence holes conjugated/alternating double and single bonds, and a localized core-hole, which triggers valence motion in the conjugated π system. The dynamics are calculated from the time-dependent hole density, obtained using real-time time-dependent density functional theory (RT-TDDFT). To avoid well-known excited-state challenges for TDDFT[38–44], prepared initial excited states are used to capture CM[37]. Such initial states act somewhat like a broadband excitation, and the total response is multimodal. Here, we extract the relevant CM modes to compute experimentally relevant metrics such as migration time, distance, and speed. The hole densities and CM frequencies are compared and validated with literature values from correlated calculations (e.g., time-dependent Schrödinger equation (TDSE)[6] or algebraic diagrammatic construction (ADC(n)))[45,46], and the mode dynamics are interpreted using the time-dependent electron localization function (TDELF)[47–49]. The TDELF has been shown previously to cast the dynamics into an "attochemistry" framework, offering an intuitive way to predict and interpret complicated charge

migration dynamics in terms of simple chemistry mechanisms[37]. Earlier work has revealed a universal attosecond response following ionization[50]. Here, we show that the CM metrics also exhibit a universal response in conjugated molecules.

5.2 Extraction Procedure

The overall technical approach has four steps. To obtain the hole dynamics, we (I) choose an initial state for the ionized molecule that mimics strong-field or core ionization. In this sudden approximation, the molecule is left in a non-stationary state. We then (II) propagate from this state to obtain the time-dependent hole density. Since the initial state is approximate, many modes are excited. This acts somewhat like a broadband excitation, including dynamics from charge migration and density-like excitations. In order to distinguish between CM dynamics and non-CM excitations, we then (III) extract CM modes via frequency analysis of the hole density. Here, we determine which regions in a molecule have correlated charge motion at various frequencies by Fourier transforming (FT) the time-dependent hole density. Phase maps are then created from the FT of the density at these frequencies to show regions where the hole starts and where it ends. Once the mode is extracted, (IV) metrics such as migration length and speed are easily computed. Using these modes and metrics, we contruct the attochemistry mechanism of the dynamics from the TDELF and relate to the corresponding Lewis dot structures.

For each simulation, the initial state was chosen to represent a particular type of hole. To prepare the initial state of the ICCH (iodoacetylene) case, the hole is created by removing one electron by partially depleting the population of the molecular orbitals involved during ionization[6]. The resulting initial state has a valence hole that begins localized on the iodine atom. Similarly, the OCS (carbonyl sulfide) initial state was constructed by removing population from multiple orbitals with a valence hole beginning on the sulfur atom. These populations were obtained from a TDDFT ionization simulation[51] for light polarized perpendicular to the molecular axis. The initial states of the alkenes (hexatriene $CH_2(CH)_4CH_2$ and

the diborane $CH_2CH(BH)_2CHCH_2$) were constructed with a non-physical localized π hole on the terminal double bond of each molecule to compare with previous ADC results[45]. For the core-hole triggered charge migration in nitrosobenzene, the initial state was prepared by removing a core electron from the nitrogen 1s orbital[37,46]. Additional details for each initial state's preparation are included in Appendix C.

From these initial conditions, we propagate the density matrix using a development version of the RT-TDDFT module[52] in NWChem.[53] (See Appendix C for details) We use the same basis sets and functional (PBE0) as the initial state calculations. Hybrid functionals such as PBE0 have been shown to give accurate charge migration dynamics, likely due to reduced self-interaction and improved long-range Coulomb interactions.[37] Additional details are included in Appendix C.

5.3 Extraction and Identification of Charge Migration Modes

Next, we extract the charge migration modes from the Fourier transform (FT) of the time-dependent hole density. Fig. 5.1 (top) shows the amplitude of the FT of the hole density $\rho_H(r,\omega)$ integrated over x and y (transverse to the CM axis z along the molecule) to give $\rho_H(z,\omega)$. The amplitude of the FT of the hole density in space is related to the probability of finding a particle or hole at a given position and frequency. In other words, the amplitude illustrates the extent of the hole migration along the migration path (z). For a real-space picture of the modes, the bottom two panels (A & B) show the weighted phase of the transformed hole density at a the corresponding frequency ($\phi_w(r,\omega_0)$).

$$\phi_w(r,\omega_0) = \phi(r,\omega_0)\,|\rho_H(r,\omega_0)| \tag{5.2}$$

Here, the phase of the FT shows how positions in the molecule are correlated or anticorrelated (in or out of phase); thus, multiplying the amplitude ($|\rho_H|$) and phase (ϕ) illustrates where the hole is likely to be at the start of a period, and where it will be half a period later.

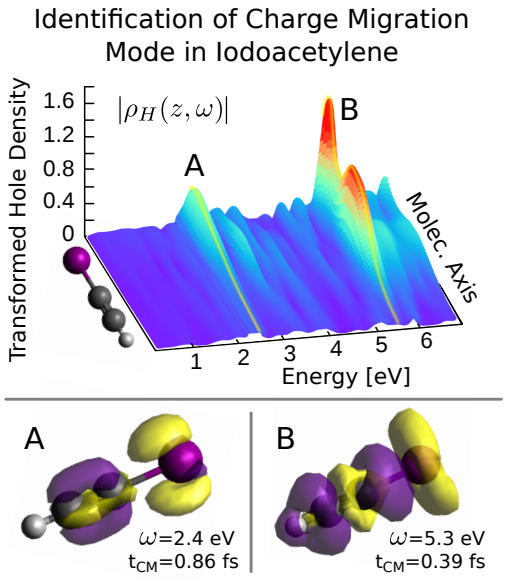

Figure 5.1: The amplitude of the Fourier transform of the hole density of iodoacetylene integrated along x and y (top). This shows the extent of the hole migration along the molecular axis (z). The 3D weighted phase (see text) for a given mode (bottom) shows that the charge oscillates back and forth between the positive (yellow) and negative (purple) regions at that frequency. These phase plots can be used to distinguish between charge migration (A) and excitation (B) modes.

(see appendix for details). For a given frequency, we define the hole migration time $t_{\mathrm{CM}} = T/2 = \pi/\omega$, where T is the period corresponding to that frequency. The phase map for that frequency thus shows where the hole starts (yellow; positive) and where it ends (purple; negative) in the time t_{CM}. Due to the lack of dephasing, our simulations are time-reversible. Since the CM time scales are much faster than dephasing processes, holes are expected to survive at least one half-period in real systems, if not longer[54–56]. Fig. 5.1 shows the spectrum and phase maps for iodoacetylene where there is a mode that takes 0.86 fs to travel across the molecule (A) and one that takes 0.39 fs (B). We identify mode A as charge migration, while B is non-migration; differentiation between these two is discussed in the next section.

Often, it can be challenging to visually distinguish between coherent charge-like migration and other non-migration excitations, which are more density-like. One way to quickly

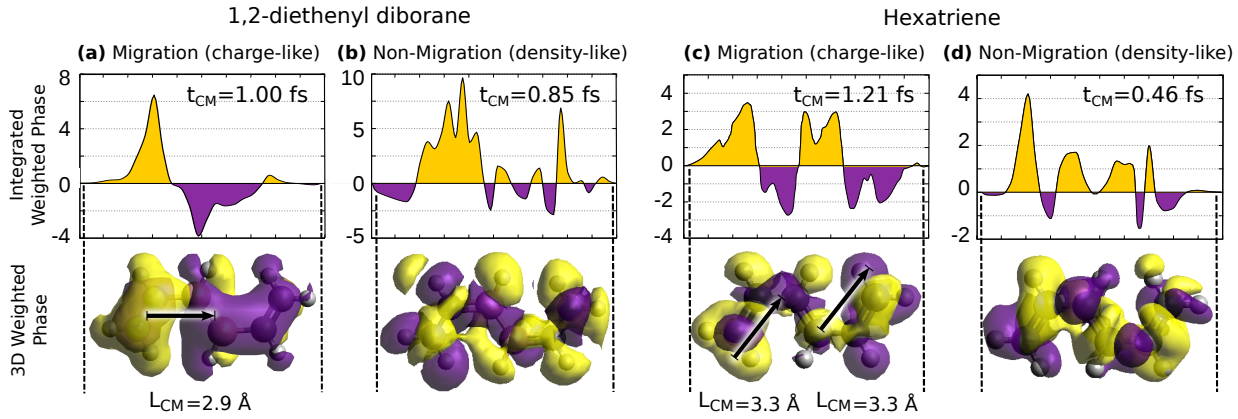

Figure 5.2: Weighted phase integrated over x and y (top row) and 3D weighted phase maps (bottom row) of migration and non-migration modes in two alkene molecules. In the integrated phase plots, two large, anticorrelated (+/-) regions indicate charge-like motion. The 1,2-diethenyl diborane (a) has large regions, with yellow→purple migration in 1.00 fs. In contrast, the 0.85 fs mode (b) shows a localized hole at the left end, but small discontinous regions on the right. In hexatriene, mode (d) is delocalized and density-like, whereas mode (c) is migration-like, best understood in an attochemistry interpretation to be an allylic radical and hole migration.

classify modes is by integrating the 3D weighted phase maps over transverse directions (x and y). This serves to emphasize regions where the hole is likely to be found along the migration axis (z) and qualitatively show the hole localization. In addition, these integrated phase maps show how different regions of the molecule are correlated in time. Fig. 5.2 (top) illustrates this can be used to characterize the CM and non-CM modes in hexatriene and 1,2-diethenyl diborane. Essentially, plots with localized anticorrelated regions (i.e., both a large positive/yellow and negative/purple region) correspond to charge-like dynamics (migration), whereas plots with alternating and diffuse phase plots correspond to delocalized (density-like) modes.

For example, Fig. 5.2 shows the integrated phase plot (top) and the 3D phase map (bottom) for charge migration and non-migration modes in the two alkenes. Column (a) shows the $t_{\mathrm{CM}} = 1.00$ fs ($\hbar\omega_0 = 1.71$ eV) mode in 1,2-diethenyl diborane. This shows two large, well-separated anticorrelated regions indicating charge-like motion. Similarly,

the 1.21 fs mode of hexatriene (c) roughly shows contiguous regions; however, these are on the left, middle, and right of the molecule (see arrows). An attochemistry interpretation (discussed below) shows this to be a hole migration from the left to the middle, in conjunction with a radical migrating from the left to the middle. In contrast to both of these charge migration modes, the 0.85 fs mode (b) and the 0.46 fs mode both exhibit a localized hole at the left end, but many small discontinuous regions on the right. This corresponds to a density-like excitation where a hole "blinks" in and out on one end, but gets delocalized or "washed out" as it travels to the other side.

5.4 Calculation of Experimentally Relevant Charge Migration Metrics

Once the modes have been extracted and classified as charge migration, they can be characterized to yield physical quantities like migration time, length, and speed. As discussed previously, the migration time can be obtained from the mode frequency $t_{\mathrm{CM}} = \pi/\omega_0$. Another metric is the hole migration length L_{CM}, which can be thought of as the distance a classical positive charge moves during a migration event. We define this as the distance between the midpoint of $\phi_w(z, \omega_0)$ in one dominant correlated region to the minimum in another anticorrelated region. These are shown by the arrows in Fig. 5.2. From this distance, we can compute the charge migration speed $v_{\mathrm{CM}} = L_{\mathrm{CM}}/t_{\mathrm{CM}}$. For example, the CM mode in 1,2-diethenyl diborane takes 1.00 fs to travel 2.92 Å, and thus has a migration speed of $v_{\mathrm{CM}} = 2.92$ Å/fs. To put this in context, this is ∼0.1% the speed of light, or roughly seven times slower than the mean orbital "speed" of an electron in hydrogen. Alternatively, we consider the speed in terms of number of bonds traveled per femtosecond. Using an average C=C bond length, this mode has a travel speed of 2.2 bonds/fs. These metrics for each molecule have been included in Table 5.1 along with the corresponding 3D phase maps. Comparisons with previous calculated and experimentally observed results migration times are shown in parentheses[6,45,46]; our TDDFT results agree well in all cases.

Table 5.1: Metrics for Various Charge Migration Modes.

System	CM Time (Ref.)	CM Length	CM Speed (bonds/fs)	Phase Map
Carbonyl Sulfide* OCS	1.10 fs –	2.14 Å	1.5	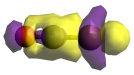
Iodoacetylene* ICCH	0.86 fs (0.93)[6]	2.58 Å	2.2	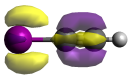
Hexatriene† $CH_2(CH)_4CH_2$	1.21 fs (1.19)[45]	3.29 Å	2.1	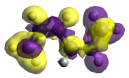
Diborane† $CH_2CH(BH)_2CHCH_2$	1.00 fs (1.02)[45]	2.92 Å	2.3	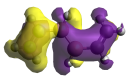
Nitrosobenzene‡ ONC_6H_5	0.70 fs (0.70)[46]	2.89 Å	3.1	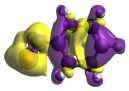

Initial States: **valence hole in multiple orbitals*, †*localized π hole*, and ‡*localized core-hole* .

It is interesting to note that for three of the valence hole cases (iodoacetylene, hexatriene, and the diborane), the holes have nearly identical speed. This suggests that holes in conjugated molecules have a universal speed of ∼2 bonds/fs. On the other hand, OCS, which has a staggered cumulene π system, has a slower CM speed. This is similar to what is observed in incoherent electron transport in organic molecules, where cumulenes have lower electron mobility than conjugated molecules[57].The nitrosobenzene example involves the creation of a stationary 1s hole on the nitrogen atom that drives valence motion[46]. This motion is faster than the valence hole cases, and is likely due to the change in effective electron/nuclear potential caused by the core-hole.

5.5 Electron Localization and the Attochemistry Picture

In addition to properties, a physical and chemical time-dependent representation can be constructed by combining these metrics with their associated dynamics. Since hole densities

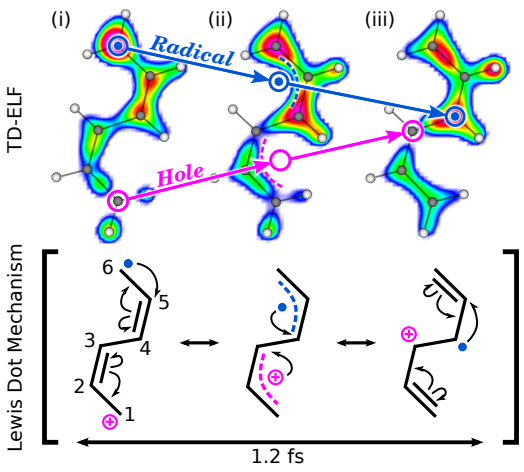

Figure 5.3: Snapshots of the hole migration in hexatriene following localized ionization from C1-C2. The time-dependent electron localization function (top row) shows the hole (magenta circles) as a region of decreased electron localization, moving from the C1 carbon to the C3 carbon at the bottom of molecule. At the same time, the allylic radical moves through the top three carbon atoms from C6→C4. As both the hole and radical move, they become delocalized across nearby carbons (B, dashed lines). These CM dynamics can be qualitatively mapped onto an evolving superposition of Lewis-dot resonance structures (bottom), offering a way to chemically predict the charge migration response.

can be congested, and orbitals are non-physical, we instead use a Lewis-dot picture. In this chemistry-inspired framework, the time-dependent electron localization function (TDELF) casts the hole migration in terms of evolving double bonds and lone pair electrons[47,48], and has been shown to map directly onto Lewis-dot resonance structures[37]. Fig. 5.3 (top row) shows the TDELF for CM mode in hexatriene ($t_{\mathrm{CM}} = 1.21$ fs from fig. 5.2 (c)). Here, we first computed the TDELF from the time-dependent density, which we then filtered to include only a narrow range of frequencies around ω_0 (see Appendix C for details).

The observed ELF exhibits a somewhat unexpected "half migration" mechanism, where the hole (magenta circle) is first localized on $[\mathrm{C1}]^+$ (i). As it moves, the hole then delocalizes across the first three allylic carbons $[\mathrm{C1{=}C2{=}C3}]^+$ (ii), appearing as a superposition (dashed lines) of a hole at C1 and C3. Finally, the hole migrates to a localized position on $[\mathrm{C3}]^+$ (iii). There is a simultaneous complimentary radical (blue circle) migration from the opposite

end of the molecule: C6$^{\bullet}\rightarrow$ [C6=C5=C4]$^{\bullet}\rightarrow$ C4$^{\bullet}$. An alternative way of interpreting this processes is a shuffling of the two double bonds away from the center of the molecule. The corresponding organic chemistry resonance structures (bottom) predict the same migration mechanism for the allylic cation and radical. In such systems, the radical or hole is known to become delocalized and travel between the three allylic carbons.

Besides their use in chemically interpreting the path of migration, resonance structure mechanisms also provide a way to anticipate hole dynamics in families of molecules. For instance, since the valence holes in conjugated π systems migrate at $\sim$2 bonds/fs, we can use the resonance mechanism to chemically predict CM and timescales in a range of molecules. In other words, by knowing where the hole starts, how it moves through the molecule, and at what speed, these tools offer a universal means of chemically predicting and describing charge migration.

In summary, we have shown that charge migration modes can be extracted and identified from the total response of the time-dependent density, and further analysis of these modes yields physical metrics such as migration length, time, and speed. Not only are metrics relevant to experimental observables,but we also show how these metrics can be combined with a mechanistic Lewis-dot picture to both interpret and predict experiments. This "attochemistry" interpretation forms a bridge between physics and chemistry that can be used to anticipate hole dynamics from chemical principles without computationally intensive simulations. Indeed, we can predict if a molecule may have an interesting charge migration response based upon its donor/acceptor groups, degree of conjugation, branching ratios, and structure. For instance, an amine group would likely attract a hole created on an aromatic halogen. By extension, we predict that non-symmetric molecules with such "source-sink" functionalization can be used to create uneven superposition hole states akin to photochemical processes, with holes instead of photoproducts.

This work was supported by U. S. Department of Energy, Office of Science, Office of Basic Energy Sciences, under Award No. DE-SC0012462. Portions of this research were conducted with high performance computational resources provided by Louisiana State University (http://www.hpc.lsu.edu) and Louisiana Optical Network Infrastructure (http://www.loni.org).

5.6 References

[1] M. Uiberacker, T. Uphues, M. Schultze, A. J. Verhoef, V. Yakovlev, M. F. Kling, J. Rauschenberger, N. M. Kabachnik, H. Schröder, M. Lezius, *et al.*, "Attosecond real-time observation of electron tunnelling in atoms," *Nat.*, vol. 446, no. 7136, p. 627, 2007.

[2] M. Schultze, M. Fieß, N. Karpowicz, J. Gagnon, M. Korbman, M. Hofstetter, S. Neppl, A. L. Cavalieri, Y. Komninos, T. Mercouris, *et al.*, "Delay in photoemission," *Sci.*, vol. 328, no. 5986, pp. 1658–1662, 2010.

[3] G. Sansone, F. Kelkensberg, J. Pérez-Torres, F. Morales, M. F. Kling, W. Siu, O. Ghafur, P. Johnsson, M. Swoboda, E. Benedetti, *et al.*, "Electron localization following attosecond molecular photoionization," *Nat.*, vol. 465, no. 7299, p. 763, 2010.

[4] P. Ranitovic, C. W. Hogle, P. Rivière, A. Palacios, X.-M. Tong, N. Toshima, A. González-Castrillo, L. Martin, F. Martín, M. M. Murnane, *et al.*, "Attosecond vacuum uv coherent control of molecular dynamics," *Proc. Nat. Acad. Sci.*, vol. 111, no. 3, pp. 912–917, 2014.

[5] F. Calegari, D. Ayuso, A. Trabattoni, L. Belshaw, S. De Camillis, S. Anumula, F. Frassetto, L. Poletto, A. Palacios, P. Decleva, *et al.*, "Ultrafast electron dynamics in phenylalanine initiated by attosecond pulses," *Sci.*, vol. 346, no. 6207, pp. 336–339, 2014.

[6] P. M. Kraus, B. Mignolet, D. Baykusheva, A. Rupenyan, L. Hornỳ, E. F. Penka, G. Grassi, O. I. Tolstikhin, J. Schneider, F. Jensen, *et al.*, "Measurement and laser control of attosecond charge migration in ionized iodoacetylene," *Science*, vol. 350, no. 6262, pp. 790–795, 2015.

[7] O. Smirnova, Y. Mairesse, S. Patchkovskii, N. Dudovich, D. Villeneuve, P. Corkum, and M. Y. Ivanov, "High harmonic interferometry of multi-electron dynamics in molecules," *Nat.*, vol. 460, no. 7258, p. 972, 2009.

[8] L. Belshaw, F. Calegari, M. J. Duffy, A. Trabattoni, L. Poletto, M. Nisoli, and J. B. Greenwood, "Observation of ultrafast charge migration in an amino acid," *J. Phys. Chem. Lett.*, vol. 3, no. 24, pp. 3751–3754, 2012.

[9] K. C. Kulander, "Time-dependent hartree-fock theory of multiphoton ionization: Helium," *Phys. Rev. A*, vol. 36, no. 6, p. 2726, 1987.

[10] X. Li, S. M. Smith, A. N. Markevitch, D. A. Romanov, R. J. Levis, and H. B. Schlegel, "A time-dependent hartree–fock approach for studying the electronic optical response of molecules in intense fields," *Phys. Chem. Chem. Phys.*, vol. 7, no. 2, pp. 233–239, 2005.

[11] C. M. Isborn and X. Li, "Singlet-triplet transitions in real-time time-dependent hartree-fock/density functional theory," *J. Chem. Theory Comput.*, vol. 5, no. 9, pp. 2415–2419, 2009.

[12] T. Ikemachi, Y. Shinohara, T. Sato, J. Yumoto, M. Kuwata-Gonokami, and K. L. Ishikawa, "Time-dependent hartree-fock study of electron-hole interaction effects on high-harmonic generation from periodic crystals," *arXiv preprint arXiv:1709.08153*, 2017.

[13] D. Haxton and C. McCurdy, "Ultrafast population transfer to excited valence levels of a molecule driven by x-ray pulses," *Phys. Rev. A*, vol. 90, no. 5, p. 053426, 2014.

[14] H.-D. Meyer, U. Manthe, and L. S. Cederbaum, "The multi-configurational time-dependent hartree approach," *Chem. Phys. Lett.*, vol. 165, no. 1, pp. 73–78, 1990.

[15] M. Nest, T. Klamroth, and P. Saalfrank, "The multiconfiguration time-dependent hartree–fock method for quantum chemical calculations," *J. Chem. Phys.*, vol. 122, no. 12, p. 124102, 2005.

[16] T. Sato and K. L. Ishikawa, "Time-dependent complete-active-space self-consistent-field method for multielectron dynamics in intense laser fields," *Phys. Rev. A*, vol. 88, no. 2, p. 023402, 2013.

[17] S. A. Ndengue, R. Dawes, F. Gatti, and H.-D. Meyer, "Resonances of hco computed using an approach based on the multiconfiguration time-dependent hartree method," *The Journal of Physical Chemistry A*, vol. 119, no. 50, pp. 12043–12051, 2015.

[18] P. Krause, T. Klamroth, and P. Saalfrank, "Time-dependent configuration-interaction calculations of laser-pulse-driven many-electron dynamics: Controlled dipole switching in lithium cyanide," *J. Chem. Phys.*, vol. 123, no. 7, p. 074105, 2005.

[19] A. E. DePrince III, M. Pelton, J. R. Guest, and S. K. Gray, "Emergence of excited-state plasmon modes in linear hydrogen chains from time-dependent quantum mechanical methods," *Phys. Rev. Lett.*, vol. 107, no. 19, p. 196806, 2011.

[20] P. Krause, J. A. Sonk, and H. B. Schlegel, "Strong field ionization rates simulated with time-dependent configuration interaction and an absorbing potential," *J. Chem. Phys.*, vol. 140, no. 17, p. 174113, 2014.

[21] P. Hoerner and H. B. Schlegel, "Angular dependence of ionization by circularly polarized light calculated with time-dependent configuration interaction with an absorbing potential," *The Journal of Physical Chemistry A*, vol. 121, no. 6, pp. 1336–1343, 2017.

[22] D. R. Nascimento and A. E. DePrince, "Simulation of near-edge x-ray absorption fine structure with time-dependent equation-of-motion coupled-cluster theory," *J. Phys. Chem. Lett.*, vol. 8, no. 13, pp. 2951–2957, 2017.

[23] C. Huber and T. Klamroth, "Explicitly time-dependent coupled cluster singles doubles calculations of laser-driven many-electron dynamics," *J. Chem. Phys.*, vol. 134, no. 5, p. 054113, 2011.

[24] S. Kvaal, "Ab initio quantum dynamics using coupled-cluster," *J. Chem. Phys.*, vol. 136, no. 19, p. 194109, 2012.

[25] E. Runge and E. K. U. Gross, "Density-functional theory for time-dependent systems," *Phys. Rev. Lett.*, vol. 52, pp. 997–1000, Mar 1984.

[26] M. Petersilka, U. Gossmann, and E. Gross, "Excitation energies from time-dependent density-functional theory," *Phys. Rev. Lett.*, vol. 76, no. 8, p. 1212, 1996.

[27] A. Dreuw, J. L. Weisman, and M. Head-Gordon, "Long-range charge-transfer excited states in time-dependent density functional theory require non-local exchange," *J. Chem. Phys.*, vol. 119, no. 6, pp. 2943–2946, 2003.

[28] T. Stein, L. Kronik, and R. Baer, "Reliable prediction of charge transfer excitations in molecular complexes using time-dependent density functional theory," *J. Am. Chem. Soc.*, vol. 131, no. 8, pp. 2818–2820, 2009.

[29] C. M. Isborn and X. Li, "Modeling the doubly excited state with time-dependent hartree–fock and density functional theories," *J. Chem. Phys.*, vol. 129, no. 20, p. 204107, 2008.

[30] X.-M. Tong and S.-I. Chu, "Time-dependent density-functional theory for strong-field multiphoton processes: Application to the study of the role of dynamical electron correlation in multiple high-order harmonic generation," *Phys. Rev. A*, vol. 57, no. 1, p. 452, 1998.

[31] M. Lein and S. Kümmel, "Exact time-dependent exchange-correlation potentials for strong-field electron dynamics," *Phys. Rev. Lett.*, vol. 94, no. 14, p. 143003, 2005.

[32] K. Lopata and N. Govind, "Near and above ionization electronic excitations with non-hermitian real-time time-dependent density functional theory," *J. Chem. Theory Comput.*, vol. 9, no. 11, pp. 4939–4946, 2013.

[33] K. Lopata, B. E. Van Kuiken, M. Khalil, and N. Govind, "Linear-response and real-time time-dependent density functional theory studies of core-level near-edge x-ray absorption," *J. Chem. Theory Comput.*, vol. 8, no. 9, pp. 3284–3292, 2012.

[34] P. J. Lestrange, P. D. Nguyen, and X. Li, "Calibration of energy-specific tddft for modeling k-edge xas spectra of light elements," *J. Chem. Theory Comput.*, vol. 11, no. 7, pp. 2994–2999, 2015.

[35] F. Ding, B. E. Van Kuiken, B. E. Eichinger, and X. Li, "An efficient method for calculating dynamical hyperpolarizabilities using real-time time-dependent density functional theory," *J. Chem. Phys.*, vol. 138, no. 6, p. 064104, 2013.

[36] S. A. Fischer, C. J. Cramer, and N. Govind, "Excited state absorption from real-time time-dependent density functional theory," *J. Chem. Theory Comput.*, vol. 11, no. 9, pp. 4294–4303, 2015.

[37] A. Bruner, S. Hernandez, F. Mauger, P. M. Abanador, D. J. LaMaster, M. B. Gaarde, K. J. Schafer, and K. Lopata, "Attosecond charge migration with tddft: Accurate dynamics from a well-defined initial state," *The Journal of Physical Chemistry Letters*, vol. 8, no. 17, pp. 3991–3996, 2017.

[38] J. I. Fuks, P. Elliott, A. Rubio, and N. T. Maitra, "Dynamics of charge-transfer processes with time-dependent density functional theory," *J. Phys. Chem. Lett.*, vol. 4, no. 5, pp. 735–739, 2013.

[39] N. T. Maitra and D. G. Tempel, "Long-range excitations in time-dependent density functional theory," *J. Chem. Phys.*, vol. 125, no. 18, p. 184111, 2006.

[40] K. Giesbertz and E. Baerends, "Failure of time-dependent density functional theory for excited state surfaces in case of homolytic bond dissociation," *Chem. Phys. Lett.*, vol. 461, no. 4, pp. 338–342, 2008.

[41] R. Requist and O. Pankratov, "Adiabatic approximation in time-dependent reduced-density-matrix functional theory," *Phys. Rev. A*, vol. 81, no. 4, p. 042519, 2010.

[42] M. R. Provorse, B. F. Habenicht, and C. M. Isborn, "Peak-shifting in real-time time-dependent density functional theory," *J. Chem. Theory Comput.*, vol. 11, no. 10, pp. 4791–4802, 2015.

[43] J. I. Fuks, K. Luo, E. D. Sandoval, and N. T. Maitra, "Time-resolved spectroscopy in time-dependent density functional theory: An exact condition," *Phys. Rev. Lett.*, vol. 114, no. 18, p. 183002, 2015.

[44] S. Raghunathan and M. Nest, "The lack of resonance problem in coherent control with real-time time-dependent density functional theory," *J. Chem. Theory Comput.*, vol. 8, no. 3, pp. 806–809, 2012.

[45] A. D. Dutoi, M. Wormit, and L. S. Cederbaum, "Ultrafast charge separation driven by differential particle and hole mobilities," *The Journal of chemical physics*, vol. 134, no. 2, p. 024303, 2011.

[46] A. I. Kuleff, N. V. Kryzhevoi, M. Pernpointner, and L. S. Cederbaum, "Core ionization initiates subfemtosecond charge migration in the valence shell of molecules," *Phys. Rev. Lett.*, vol. 117, no. 9, p. 093002, 2016.

[47] A. D. Becke and K. E. Edgecombe, "A simple measure of electron localization in atomic and molecular systems," *J. Chem. Phys.*, vol. 92, no. 9, pp. 5397–5403, 1990.

[48] T. Burnus, M. A. Marques, and E. K. Gross, "Time-dependent electron localization function," *Phys. Rev. A*, vol. 71, no. 1, p. 010501, 2005.

[49] A. Parise, A. Alvarez-Ibarra, X. Wu, X. Zhao, J. Pilmé, and A. de la Lande, "Quantum chemical topology of the electron localization function in the field of attosecond electron dynamics," *J. Phys. Chem. Lett.*, 2018.

[50] J. Breidbach and L. Cederbaum, "Universal attosecond response to the removal of an electron," *Phys. Rev. Lett.*, vol. 94, no. 3, p. 033901, 2005.

[51] A. Sissay, P. Abanador, F. Mauger, M. Gaarde, K. J. Schafer, and K. Lopata, "Angle-dependent strong-field molecular ionization rates with tuned range-separated time-dependent density functional theory," *J. Chem. Phys.*, vol. 145, no. 9, p. 094105, 2016.

[52] K. Lopata and N. Govind, "Modeling fast electron dynamics with real-time time-dependent density functional theory: Application to small molecules and chromophores," *J. Chem. Theory Comput.*, vol. 7, no. 5, pp. 1344–1355, 2011.

[53] M. Valiev, E. J. Bylaska, N. Govind, K. Kowalski, T. P. Straatsma, H. J. Van Dam, D. Wang, J. Nieplocha, E. Apra, and T. L. Windus, "Nwchem: A comprehensive and scalable open-source solution for large scale molecular simulations," *Comp. Phys. Comm.*, vol. 181, no. 9, pp. 1477–1489, 2010.

[54] M. Vacher, M. J. Bearpark, and M. A. Robb, "Communication: Oscillating charge migration between lone pairs persists without significant interaction with nuclear motion in the glycine and gly-gly-nh-ch3 radical cations," *J Chem. Phys.*, vol. 140, p. 201102, 2014.

[55] V. Despré, A. Marciniak, V. Loriot, M. Galbraith, A. Rouzée, M. Vrakking, F. Lépine, and A. Kuleff, "Attosecond hole migration in benzene molecules surviving nuclear motion," *J. Phys. Chem. Lett.*, vol. 6, no. 3, pp. 426–431, 2015.

[56] K. Spinlove, M. Vacher, M. Bearpark, M. Robb, and G. Worth, "Using quantum dynamics simulations to follow the competition between charge migration and charge transfer in polyatomic molecules," *J. Chem. Phys.*, vol. 482, pp. 52–63, 2017.

[57] C. H. Hendon, D. Tiana, A. T. Murray, D. R. Carbery, and A. Walsh, "Helical frontier orbitals of conjugated linear molecules," *Chem. Sci.*, vol. 4, no. 11, pp. 4278–4284, 2013.

Chapter 6. Conclusions and Outlook

The motivation of the work outlined in this dissertation was to study the response of electrons following various interactions with light. More specifically, the goals of these efforts were to: (1) accelerate the convergence of broadband spectra, (2) simulate charge migration dynamics while avoiding pathologies from the adiabatic approximation, and (3) develop a way predict charge migration and candidate molecules for associated experiments.

In Chapter 3, a technique was introduced to address the first goal. Here, the total dipole was deconstructed into molecular orbital pair dipole moments. Since these contain fewer frequencies than the total dipole, their Fourier transforms converge more quickly. To futher accelerate the transforms, Padé approximants, employing a ratio of power series, were used to fit the discrete Fourier transform and extrapolate to any spectral density. This technique not only allowed for acceleration, but also natively contained the contributions to the excitation peaks in valence and core absorption spectra. To validate, results were compared for valence and core spectra of water of established linear-response methods. Nitrogen K-edge XANES in a nickel porphyrin were also found to be consistent with experimental results, and the edge could be computed directly without spurious, non-physical phantom peaks. Studies in these areas offer valuable information about the structural environment useful in designing and characterizing materials. Futher work in this area would be to incorporate spin-orbit coupling to provide more accurate peak splitting near the core absorption edge.[1]

In Chapter 4, the use of well-defined initial states following an electron ionization event was shown to capture charge migration from an RT-TDDFT simulation. The use of these initial states circumvents the problems of resonantly driving the system to an excited state due to the adiabatic approximantion. Here, a hole was created in the nitrogen 1s orbital. This sudden removal of an electron created a non-stationary state, which induced movement of the valence electrons. The TD-ELF cast the charge density motion in terms of bonds and lone

pairs and thus map directly onto Lewis-dot resonance structures. This technique introduced a way to interpret the movement of electrons using the familiar tools of chemistry.[2]

Chapter 5 built upon the work of Chapter 4, introduced a way to extract and identify charge migration modes. In addition to providing dynamical information, we showed that these modes could be used to calculate experimentally relevant properties like migration distance, time, and speed. Various valence holes were studied, and charge migration in conjugated systems showed an average migration speed of ~ 2 bonds/fs. Combining these metrics with the Lewis-dot picture, we presented an attochemistry framework, which can predict and interpret charge motion on its native time scale. Future work would be to use attochemistry to predict charge migration dynamics in more complicated systems with different functional groups. Likely candidates would include source-sink systems where a hole would likely be attracted to a less electronegative group, or branched molecules to offer selective braching ratios based upon functionalization. Furthermore, the use of Ehrenfest and other nuclear motion techniques will offer a more complete picutre of lifetime of charge migration dynamics as well as long-range charge transfer processes.

The work of this dissertation has focused on light-matter interactions. Through the acceleration of broadband spectroscopy simulations and calculations of charge migration dynamics, we have been able to capture the complicated behavior of electrons both in absorption spectroscopy and in response to an ionization event. In addition, the introduction of attochemistry as a means to predict and describe ultrafast motion of electrons in molecules has provided a means to identify candidate molecules for charge migration studies and applications. As such, continued work in these areas will advance the fields of spectroscopy, photochemistry, photoresponsive materials, and many others.

The motivation of the work outlined in this dissertation was to study the response of electrons following various interactions with light. More specifically, the goals of these efforts were to: (1) accelerate the convergence of broadband spectra, (2) simulate charge migration

dynamics while avoiding pathologies from the adiabatic approximation, and (3) develop a way predict charge migration and candidate molecules for associated experiments.

6.1 References

[1] A. Bruner, D. LaMaster, and K. Lopata, "Accelerated broadband spectra using transition dipole decomposition and padé approximants," *J. Chem. Theory Comput.*, vol. 12, no. 8, pp. 3741–3750, 2016.

[2] A. Bruner, S. Hernandez, F. Mauger, P. M. Abanador, D. J. LaMaster, M. B. Gaarde, K. J. Schafer, and K. Lopata, "Attosecond charge migration with tddft: Accurate dynamics from a well-defined initial state," *J Phys. Chem. Lett.*, vol. 8, no. 17, pp. 3991–3996, 2017.

Appendix A. Time-Dependent Dipole Decomposition and Details of Simulations

A.1 Decomposition of Time-Dependent Dipole

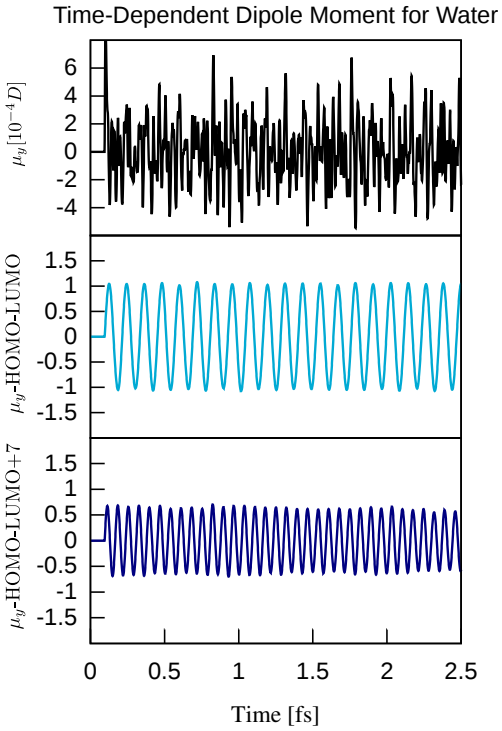

Figure A.1: Top: RT-TDDFT time signal for total y-polarized dipole for gas phase water. Middle: Time signal for the HOMO-LUMO dipole contribution. Bottom: Time signal for HOMO-LUMO+7 contribution. Overall, the dipole pair signals contain significantly fewer frequencies than the total dipole, which facilitates rapid convergence with Padé approximants.

This appendix has been reprinted from its original format as the Supporting Information in Bruner, A., LaMaster, D., Lopata, K., J. Chem. Theory Comput., 2016, 12 (8), pp 3741-3750. with permission by the authors and the journal. Copyright ©2016 J. Chem. Theory Comput. [1]

A.2 TDDFT Simulation and Signal Processing Parameters

Table A.1: Simulation and signal processing parameters. All parameters are in atomic units.

System	Propagation		Electric Field			Fourier		Padé
	Δt	$t_{\max}$	t_0	w	κ	τ	N_{pad}	τ
H_2O valence	0.2	varied	20	1	10^{-3}	150	0	150
H_2O core	0.05	250	20	1	10^{-3}	n/a	n/a	150
Ni Porphyrin core	0.05	250	20	1	10^{-3}	30	10^6	150

A.3 Molecular Geometries

Table A.2: Geometry of gas-phase water in Å optimized using aug-cc-pVTZ/B3LYP.

```
O      0.00000049     0.11212494     0.00000000
H      0.76340902    -0.47287058     0.00000000
H     -0.76340951    -0.47286895     0.00000000
```

Table A.3: Geometry of gas-phase nickel porphyrin in Å optimized using B3LYP and the 6-31++G** basis for C, N, and H, and the Stuttgart-RSC-1997 ECP for Ni.

Ni	-0.00043013	0.00032700	0.00434635
N	1.97707655	-0.00058867	0.00460842
N	-1.97760866	0.00015636	0.00462650
N	-0.00019993	1.97903110	0.00195261
N	0.00056105	-1.97864874	0.00248210
C	2.81810243	-1.09281861	0.00425402
C	2.81805742	1.09174737	0.00246233
C	-2.81807632	-1.09226571	0.00355179
C	-2.81843493	1.09260282	0.00288947
C	1.09215062	2.81949002	-0.00221604
C	-1.09216884	2.82012857	-0.00163721
C	1.09255492	-2.81970875	-0.00201109
C	-1.09165506	-2.81931239	-0.00133631
C	4.19874817	-0.68073994	0.00320831
C	4.19853486	0.67943060	0.00167417
C	-4.19873696	-0.68038158	0.00194500
C	-4.19900984	0.68000651	0.00147580
C	0.68072283	4.20044060	-0.00889303
C	-0.67975417	4.20087039	-0.00842317
C	0.68075787	-4.20004541	-0.01033642
C	-0.67954603	-4.20018638	-0.00954826
C	2.41534430	-2.41605857	0.00029641
C	2.41478696	2.41490024	-0.00172399
C	-2.41467608	-2.41543249	0.00042136
C	-2.41498745	2.41575599	-0.00052770
H	5.04124332	-1.35948739	0.00120746
H	5.04170247	1.35734435	-0.00212511
H	-5.04099257	-1.35938154	-0.00139153
H	-5.04266959	1.35732200	-0.00184549
H	1.36054881	5.04242476	-0.01490185
H	-1.35843780	5.04370582	-0.01427975
H	1.36033712	-5.04180754	-0.01783872
H	-1.35772762	-5.04335504	-0.01598127
H	3.18241599	3.18131200	-0.00676817
H	3.18298240	-3.18248654	-0.00304696
H	-3.18263447	3.18209229	-0.00380714
H	-3.18194221	-3.18215956	-0.00262561

A.4 References

[1] A. Bruner, D. LaMaster, and K. Lopata, "Accelerated broadband spectra using transition dipole decomposition and padé approximants," *J. Chem. Theory Comput.*, vol. 12, no. 8, pp. 3741–3750, 2016.

Appendix B. Attosecond Charge Migration from Well-Defined Initial State Supplementary Details

B.1 Contents

This supporting material which accompanies Chapter 4 on attosecond charge migration[1] contains molecular orbital plots for the different functionals, time-dependent Bader charges, an evaluation of basis set convergence, and a more detailed comparison of hole occupations for different functionals.

B.2 Molecular Orbital Plots

The dominant orbitals participating in charge migration are shown below in Fig. B.1. Although the labels of the orbitals are different, the relevant orbitals have the same symmetry. These have been included to demonstrate that the orbitals being shown in the hole occupations with different labels are physically consistent with each other. Different functionals order orbitals uniquely; thus, to compare consistently, orbital symmetries were used.

Molecular Orbital Labeling

Orbital	Hartree-Fock	PBE	PBE0	LC-PBE*
	LUMO+2	LUMO+2	LUMO+5	LUMO+45
	LUMO	LUMO	LUMO	LUMO
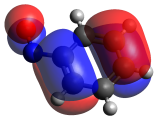	HOMO-1	HOMO-2	HOMO-2	HOMO-1
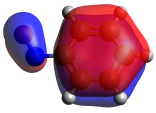	HOMO-3	HOMO-1	HOMO-4	HOMO-4

Figure B.1: The four dominant molecular orbitals involved in the O K-edge core-hole triggered dynamics in nitrosobenzene. Hartree-Fock Orbitals are from previous ADC(4) calculations (Ref. 2). Each row represents the same orbitals based upon symmetry and their respective labels for the calculation.

B.3 Time-Dependent Bader Charges

As another way of visualizing the hole migration, we have included Bader charge (atoms in molecules) analysis in Fig. B.2. Bader charges[3,4] represent the integrated charge in regions defined by boundaries where the gradient is zero. We compute the Bader charges at each timestep from the TDDFT density using the code by the Henkelman group.[5] Here, we have grouped atoms into various functional groups in the molecule to illustrate how the charge moves from the nitroso group to the ring. The charges shown have been normalized by the nuclear charges in each group. There is good agreement among the three DFT functionals; however, the HF result does not capture the correct period of the charge oscillation. This is consistent with the MO occupation analysis (See B.4)

B.4 Basis Set Convergence

Fig. B.3 shows the PBE0 dynamics for three different basis sets. Results are essentially converged for all three basis sets.

B.5 Effect of the DFT Functional

Finally, to investigate the performance of various DFT functionals, we have included a more extensive comparison among Hartree-Fock, the pure DFT (GGA) functional PBE, the hybrid PBE0, and the tuned range-separated LC-PBE*. The range-separated LC-PBE* functional was optimally tuned via the first ionization energy, with a resulting attenuation parameter of $\gamma = 0.2822$. In Fig. B.4, the ADC(4) result shows clear, coupled hole occupations between the dominant orbitals. Fig. B.4 (b) shows the TDHF hole-occupations using the same orbitals. As discussed in the main text, TDHF exhibits grossly incorrect dynamics, which is likely due to a lack of electron correlation. Fig. B.4 (c) shows the PBE results, which as a GGA-type functional, includes DFT exchange and correlation. PBE captures some of the general trends of the hole occupations from the ADC(4), but has qualitatively incorrect long-time dynamics. This has two probable sources of error: self-interaction and an incorrect

long-range Coulomb potential. Self-repulsion is expected to impact the dynamics by overly delocalizing charge and "smearing out" of the hole. This corresponds to a hole distributed among many orbitals, with no coherent oscillations observed. The incorrect Coulomb potential is also expected to yield nonphysical hole motion, similar to the well-known result that TDDFT needs exact exchange to capture charge transfer excitations.

As mentioned in the Letter, we tested this by computing the dynamics using the PBE0 functional, as shown in B.4 (d). Here, the addition of 25% exact exchange reduced the self-interaction and improved the Coulomb potential. These dynamics agree well with the ADC(4) result, capturing the period of the oscillation, population transfer, and fewer dynamics than the HF or PBE case. The dynamics were also calculated using the tuned LC-PBE* functional, and they were found to be qualitatively similar to PBE0, suggesting that even a global admixture of HF is sufficient to capture charge migration.

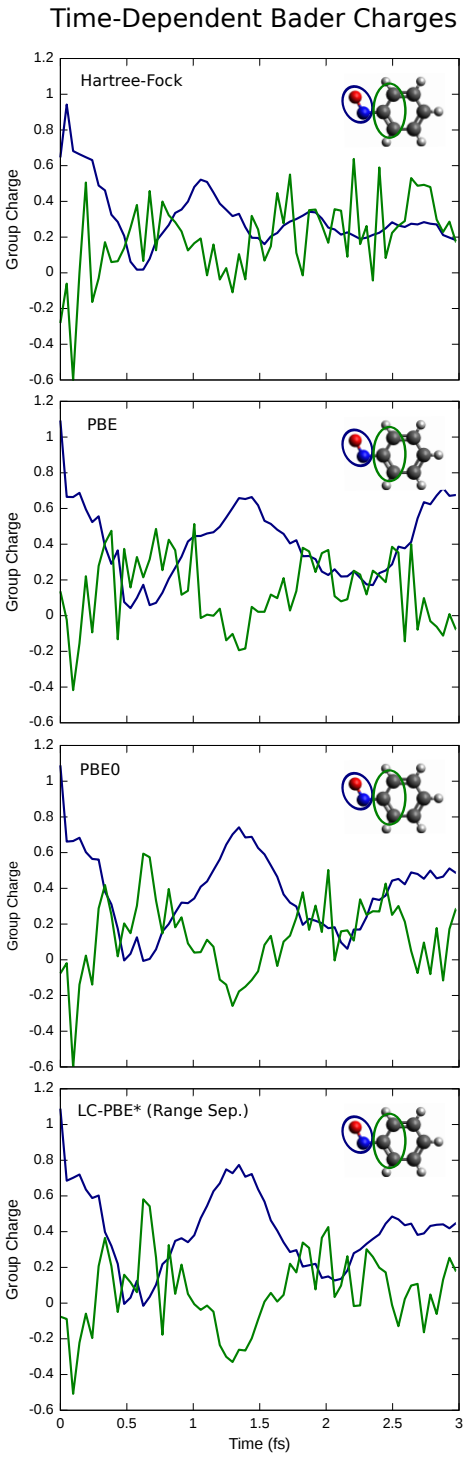

Figure B.2: The time-dependent Bader charges following ionization. The Hartree-Fock result does not capture the 1.4 fs period of the hole oscillations in Fig. 1; however, the three TDDFT functionals have similar oscillation frequencies. The results for PBE, PBE0, and LC-PBE* are consistent with each other.

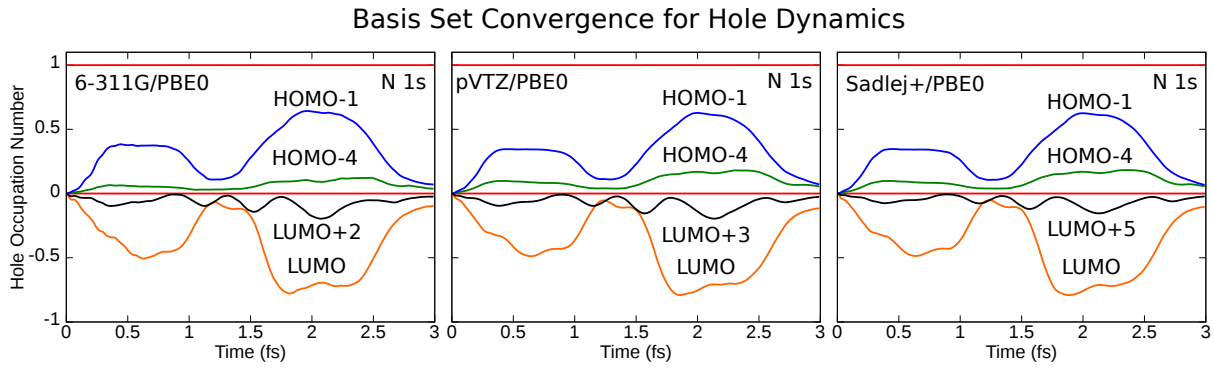

Figure B.3: Time-dependent hole occupations for three basis sets. The 6-311G, cc-pVTZ, and Sadlej+ basis sets give consistent results.

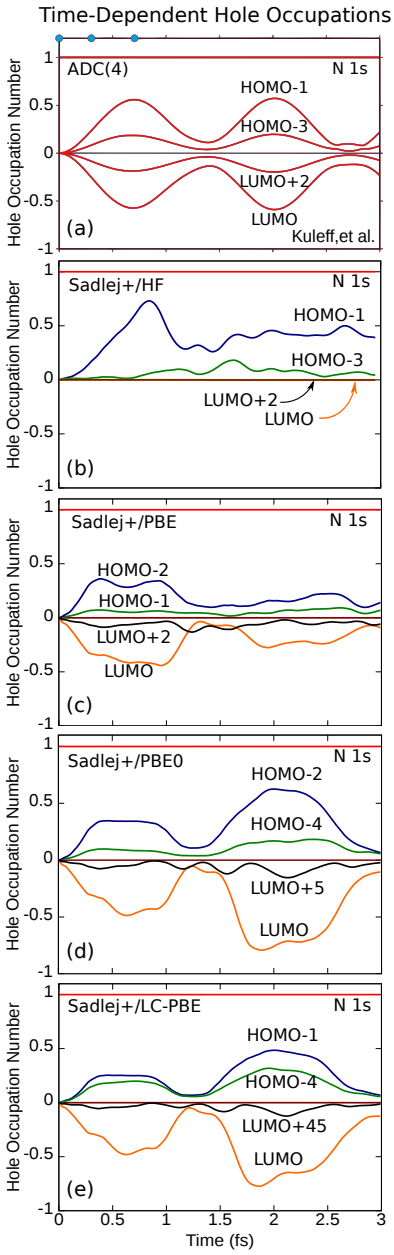

Figure B.4: Hole occupations of the dominant molecular orbitals in nitrosobenzene following N K-edge ionization. (a) ADC(4) results (digitized with permission from Ref. 2; copyright 2016 by American Physical Society). (b) Hartree-Fock shows poor agreement due lack of electron correlation. (c) TD-PBE somewhat captures the dynamics at short time, but deviates after the first oscillation. (d) TD-PBE0 and the tuned range-separated form (e) TD-LC-PBE* both show good agreement with ADC(4) results over two cycles of the hole migration. These results suggest that hybrid TDDFT adequately captures core-hole triggered valence dynamics.

B.6 References

[1] A. Bruner, S. Hernandez, F. Mauger, P. M. Abanador, D. J. LaMaster, M. B. Gaarde, K. J. Schafer, and K. Lopata, "Attosecond charge migration with tddft: Accurate dynamics from a well-defined initial state," *J Phys. Chem. Lett.*, vol. 8, no. 17, pp. 3991–3996, 2017.

[2] A. I. Kuleff, N. V. Kryzhevoi, M. Pernpointner, and L. S. Cederbaum, "Core ionization initiates subfemtosecond charge migration in the valence shell of molecules," *Phys. Rev. Lett.*, vol. 117, no. 9, p. 093002, 2016.

[3] F. W. Biegler-König, R. F. Bader, and T.-H. Tang, "Calculation of the average properties of atoms in molecules. ii," *J. Comp. Chem.*, vol. 3, no. 3, pp. 317–328, 1982.

[4] R. F. Bader, "Atoms in molecules," *Acc. Chem. Res.*, vol. 18, no. 1, pp. 9–15, 1985.

[5] G. Henkelman, A. Arnaldsson, and H. Jónsson, "A fast and robust algorithm for bader decomposition of charge density," *Comp. Mat. Sci.*, vol. 36, no. 3, pp. 354–360, 2006.

Appendix C. Identifying Modes and Properties of Charge Migration Supplementary Details

C.1 Contents

This supporting material contains details of the time propagation for the simulations, a description of the weighted phase analysis for a particle-in-a-box example, and our implementation of the frequency filtering used for the mode analysis.

C.2 Time Propagation

For the real-time time-dependent density functional theory calculations, the equation of motion in the von Neumann description is

$$i\frac{\partial \mathbf{P}'(t)}{\partial t} = [\mathbf{F}'(t), \mathbf{P}'(t)] \tag{C.1}$$

Here, $\mathbf{P}'(t)$ and $\mathbf{F}'(t)$ represent the density and Fock matrices in the canonical basis, respectively. To propagate this expression in time, a second-order Magnus (exponential midpoint) scheme is used:

$$\mathbf{P}'(t+\Delta t) = e^{-i\mathbf{F}'(t+\frac{\Delta t}{2})\Delta t}\mathbf{P}'(t)e^{i\mathbf{F}'(t+\frac{\Delta t}{2})\Delta t} \tag{C.2}$$

Each time step is propagated forward and iterated until self-consistent. Additional details of a Magnus scheme are included in ref. 1, and a review of other propagators can be found in ref. 2.

C.3 Amplitude and Weighted Phase of the Fourier Transform for Particle-in-a-Box Modes

To illustrate the mode analysis, consider the simpler example of the particle in a box. Now, double the length of the box, and the original particle will slosh back and forth in the new box. This time-dependent motion is now cast in terms of the Eigen functions and coefficients of the original box, since they are the solutions that describe the initial wave packet. Consider that if only two coefficients and corresponding Eigen functions are

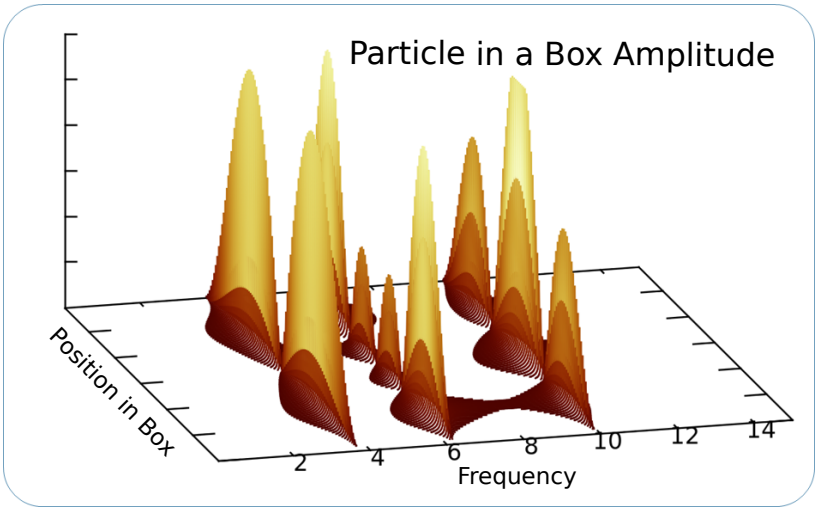

Figure C.1: Amplitude of the Fourier Transform of the first three modes of the particle in a box. The Fourier Transform separates the modes of the box by their associated frequencies.

used to describe the initial state, then then response has only one mode proportional to the difference between states 1 and 2 (N_2^2-N_1^2). By extension, the three-coefficient case has two additional modes (3 total: N_2^2-N_1^2, N_3^2-N_2^2, and N_3^2-N_1^2), and so on. As such, it is possible to gain information about all of the frequencies of the box, simply by calculating the eigenvalue differences. Similarly in molecules, the excitation and dynamical frequencies can be obtained by the energy differences between the eigenstates. The frequencies alone, however, do not provide dynamical information or offer insight into how localized or "charge-like" the excitation dynamics may be.

In order to study the dynamics, again consider the particle in a box and look at the amplitude and phase of the modes. For a given frequency, the amplitude shows the expected locations of the particle in a box, and the phase illustrates how the locations are temporally related. In other words, the phase shows which regions are correlated or anticorrelated. Multiplying amplitude by the phase, weights the phase such that it shows the particle moving from regions with a positive phase to those with a negative phase over a given half-period (i.e., for a given frequency). For dynamics in molecules, the analysis is the same: the amplitude

shows where the electron or hole is likely to be, and the weighted phase shows where it is likely to travel over a given half-period.

For the TDDFT calculations described in the Letter, the special construction of the initial states yields many modes of the molecular target, similar to a broadband excitation. For systems with many states, some modes are likely to be charge-like and have large, localized regions of charge density in the molecule. This would be indicated by how far peaks in the amplitude plots extend in the moleucule before a node. Again, the phase illustrates that if two regions are anticorrelated (opposite phase / positive and negative), then the density will move between them over a given half-period, showing a charge-like migration. In contrast, several small regions in the amplitude would illustrate non-charge-like movement of charge, but rather a density-like excitation. Such non-migration excitations are usually higher in energy and are not interesting for charge migration studies.

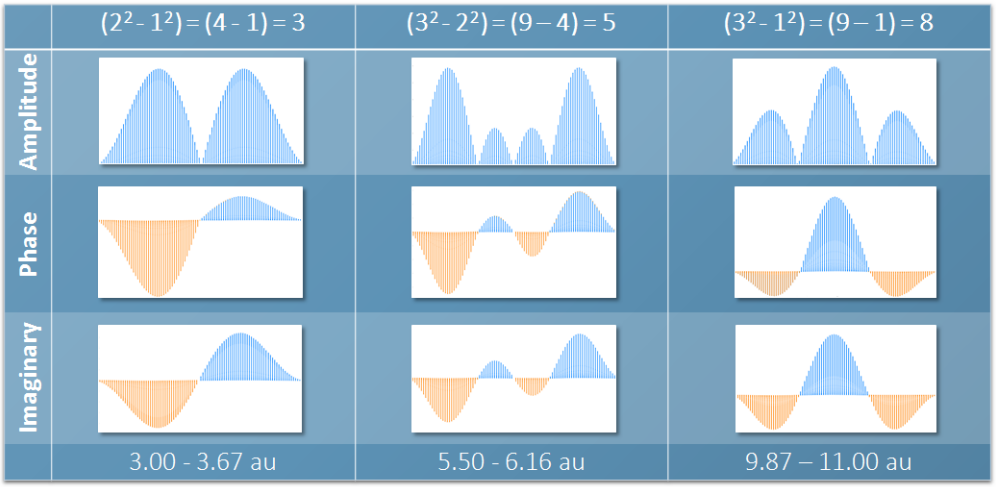

Figure C.2: Amplitude, weighted phase ($\phi_w(z, \omega_0)$) regions, and imaginary part of the Fourier transform of particle in a box modes. Amplitude shows likely positions of the particle in the box, and the weighted phase shows which regions are correlated or anticorrelated. This is useful when considering migration and non-migration modes in molecules.

C.4 Frequency Filtering

To obtain the filtered time signal, we first transform into the frequency domain. Although several different filtering methods exist, we have chosen a Gaussian filter for simplicity.

$$\widetilde{\eta}(\omega) = \frac{1}{\sigma} e^{\frac{\omega-\omega_0}{2\sigma^2}} \eta(\omega) \tag{C.3}$$

Here, the TDELF η is first transformed into the frequency domain and subsequently filtered at the frequency of interest ω_0 within a standard deviation from this value of 0.1 au to provide the corresponding localized hole dynamics $\widetilde{\eta}(\omega)$.

C.5 References

[1] K. Lopata and N. Govind, "Modeling fast electron dynamics with real-time time-dependent density functional theory: Application to small molecules and chromophores," *J. Chem. Theory Comput.*, vol. 7, no. 5, pp. 1344–1355, 2011.

[2] A. Castro, M. A. Marques, and A. Rubio, "Propagators for the time-dependent kohn–sham equations," *J. Chem. Phys.*, vol. 121, no. 8, pp. 3425–3433, 2004.

Appendix D. Publication Agreements and Permissions

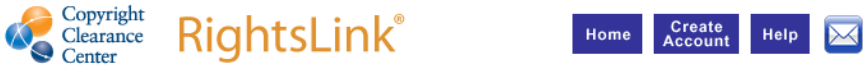

ACS Publications
Most Trusted. Most Cited. Most Read.

Title:	Accelerated Broadband Spectra Using Transition Dipole Decomposition and Padé Approximants
Author:	Adam Bruner, Daniel LaMaster, Kenneth Lopata
Publication:	Journal of Chemical Theory and Computation
Publisher:	American Chemical Society
Date:	Aug 1, 2016

LOGIN

If you're a copyright.com user, you can login to RightsLink using your copyright.com credentials.

Already **a RightsLink user** or want to learn more?

PERMISSION/LICENSE IS GRANTED FOR YOUR ORDER AT NO CHARGE

This type of permission/license, instead of the standard Terms & Conditions, is sent to you because no fee is being charged for your order. Please note the following:

- Permission is granted for your request in both print and electronic formats, and translations.
- If figures and/or tables were requested, they may be adapted or used in part.
- Please print this page for your records and send a copy of it to your publisher/graduate school.
- Appropriate credit for the requested material should be given as follows: "Reprinted (adapted) with permission from (COMPLETE REFERENCE CITATION). Copyright (YEAR) American Chemical Society." Insert appropriate information in place of the capitalized words.
- One-time permission is granted only for the use specified in your request. No additional uses are granted (such as derivative works or other editions). For any other uses, please submit a new request.

BACK CLOSE WINDOW

Title:	Attosecond Charge Migration with TDDFT: Accurate Dynamics from a Well-Defined Initial State
Author:	Adam Bruner, Samuel Hernandez, François Mauger, et al
Publication:	Journal of Physical Chemistry Letters
Publisher:	American Chemical Society
Date:	Sep 1, 2017

PERMISSION/LICENSE IS GRANTED FOR YOUR ORDER AT NO CHARGE

This type of permission/license, instead of the standard Terms & Conditions, is sent to you because no fee is being charged for your order. Please note the following:

- Permission is granted for your request in both print and electronic formats, and translations.
- If figures and/or tables were requested, they may be adapted or used in part.
- Please print this page for your records and send a copy of it to your publisher/graduate school.
- Appropriate credit for the requested material should be given as follows: "Reprinted (adapted) with permission from (COMPLETE REFERENCE CITATION). Copyright (YEAR) American Chemical Society." Insert appropriate information in place of the capitalized words.
- One-time permission is granted only for the use specified in your request. No additional uses are granted (such as derivative works or other editions). For any other uses, please submit a new request.

BACK CLOSE WINDOW

Vita

Adam S. Bruner majored in chemical engineering at Rose-Hulman Institute of Technology, receiving his B.S. in chemical engineering with a minor in chemistry in 2013. Following his undergraduate career, he worked as a chemical engineer, later being promoted to research scientist of chemistry. While in industry he developed solutions for a wide range of applications in batteries, capacitors, pigments, flame retardants, fuel stabilizers, coatings, among others. He is pursuing a concurrent M.S./Ph.D. in physical chemistry with a graduate minor in physics as a doctoral candidate in the Lopata research group at Louisiana State University in Baton Rouge, LA. His research interests include charge migration, charge transfer, and excited state electron dynamics, specifically as they relate to spectroscopy, photochemistry, photovoltaics, quantum computing, quantum optics, and specialty materials.